On-chip Single-photon Sources for Quantum Information Technology

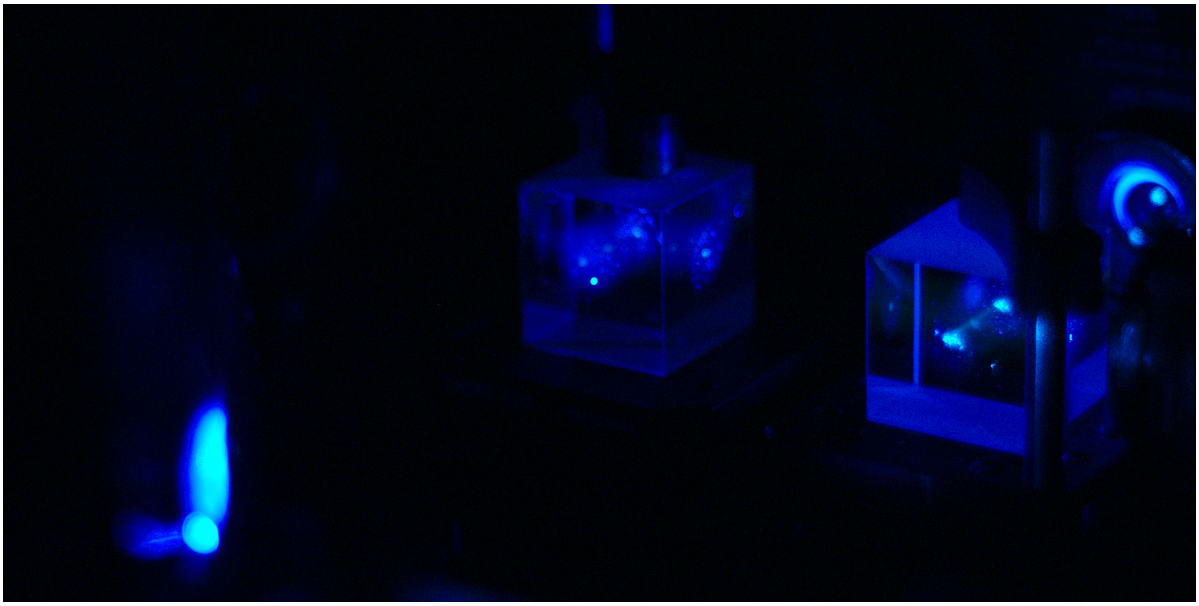

Photograph of beamsplitters illuminated by a blue light emitting diode and laser.

University of Southampton

Faculty of Physical Sciences and Engineering
Department of Physics and Astronomy
Quantum Light and Matter Research Group
Solid-State Quantum Optics Group

On-chip Single-photon Sources for Quantum Information Technology

Author:
Oliver Trojak
o.trojak@soton.ac.uk

Supervisor:
Dr. Luca Sapienza
l.sapienza@soton.ac.uk

Thesis submitted in partial fulfilment for the degree of Doctor of Philosophy

13th June, 2018

A catalogue copy is available from the University of Southampton Library Service, an electronic catalogue copy is available from ePrints Soton.

ORCID: 0000-0003-2296-6036

Cite as: O. J. Trojak, *On-chip Single-photon Sources for Quantum Information Technology*, PhD Thesis, University of Southampton (2018)

Typeset using LaTeX 2_ε

Abstract

University of Southampton
Faculty of Physical Sciences and Engineering
Department of Physics and Astronomy

On-chip Single-photon Sources for Quantum Information Technology

Oliver Trojak

The interaction of light with matter is of fundamental importance, and is the mechanism that governs how photons are generated and used. Control over this interaction can be achieved by using an optical cavity, engineering the properties of the material to create a photonic crystal, or by using plasmonic devices to confine the electromagnetic field locally. Emitters can be coupled to devices with high-quality light confinement to enhance the emission rates, creating brighter light sources for detection, for contaminant sensing or for quantum information technologies. Such technologies require bright and pure-single photon sources: a solid-state platform can meet these requirements whilst also being compatible with well-developed fabrication technologies and long-term stability.

We report metallic nanorings fabricated around selected solid-state quantum dots, to enhance vertical emission for collection by free-space optics, using a nanometre-accurate positioning technique. Enhancements of a single emission line as high as $\times 25$ are recorded thanks to a broadband lensing effect. Such metallic nanorings can be combined with deterministically-deposited super-solid immersion lenses, to provide further enhancement, $\times 10$, to that of the nanoring – creating photon sources with up to 1 MHz emission rates.

The light-matter interaction can be modified by using photonic crystals. The performance of photonic crystal devices in the visible light regime is hampered by unavoidable fabrication imperfections, which affect devices on the length-scales required for visible light operation. An alternative to such highly engineered devices is to use the fabrication disorder as a resource. Anderson localization is demonstrated using photonic crystal waveguides, and directly imaged for the first time in the visible on a nanophotonic chip. Spectral analysis shows Q-factors approaching 10,000, exceeding highly engineered devices for the first time. Optical sensing is demonstrated by making use of high-quality resonances from photonic crystals to perform sensing: a contaminant was introduced, and a resonance was shown to red-shift over $\times 100$ its line-width in response. The resonances are also sensitive to temperature, shifting about 2 nm under a 290 K change.

An alternative localization mechanism is to use aperiodic structures, where a quasi-random pattern is procedurally generated. We have fabricated and optically characterised aperiodic structures, showing efficient light confinement in a 2D system.

Index terms: Anderson Localization, Emission Enhancement, Light-Matter Interaction, Metallic Nanorings, Optical Sensing, Photonic Crystals, Photonic Crystal Cavities, Photonic Crystal Waveguides, Quantum Optics, Single Photon Sources, Solid Immersion Lenses, Solid State Quantum Dots

Unfortunately, this paper will
most probably not make part of
the scientific heritage of the topic.
This paper cannot be published
in any serious scientific journal.

Referee B

Dedicated to my loving
parents, and my grandmother
Paula, who sadly passed away
whilst I was writing.

Contents

List of Figures

List of Tables

Declaration of Authorship

I, Oliver Trojak, declare that this thesis (On-chip Single-photon Sources for Quantum Information Technology) and the work presented in it are my own and has been generated by me as the result of my own original research. I confirm that:

1. This work was done wholly or mainly while in candidature for a research degree at this University;
2. Where any part of this thesis has previously been submitted for a degree or any other qualification at this University or any other institution, this has been clearly stated;
3. Where I have consulted the published work of others, this is always clearly attributed;
4. Where I have quoted from the work of others, the source is always given. With the exception of such quotations, this thesis is entirely my own work;
5. I have acknowledged all main sources of help;
6. Where the thesis is based on work done by myself jointly with others, I have made clear exactly what was done by others and what I have contributed myself;
7. Parts of this work have been published in the works listed.

Signed: *Date:*

_____ 13th June, 2018

Publications

1. O. J. Trojak, S. I. Park, J. D. Song, L. Sapienza, "Metallic nanorings for broadband, enhanced extraction of light from solid-state emitters", *Applied Physics Letters* **111**, 021109 (2017)

2. T. Crane*, O. J. Trojak*, J. P. Vasco, S. Hughes, L. Sapienza, "Anderson localization of visible light on a nanophotonic chip", *ACS Photonics* **4**, 2274-2280 (2017) *Equal contribution

3. O. J. Trojak, T. Crane, L. Sapienza, "Optical sensing with Anderson-localised light", *Applied Physics Letters* **111**, 141103 (2017) – Editor's Pick

4. S. I. Park, O. J. Trojak, E. Lee, J. D. Song, J. Kyhm, I. Han, J. S. Kim, G. Yi, L. Sapienza, "GaAs droplet quantum dots with nanometer-thin capping layer for plasmonic applications", *Nanotechnology* **29**, 205602 (2018)

5. O. J. Trojak, C. Woodhead, J. D. Song, R. J. Young, L. Sapienza, "Combined metallic nano-rings and solid-immersion lenses for bright emission from single InAs/GaAs quantum dots", *Applied Physics Letters* **112**, 221102 (2018)

6. O. J. Trojak, C. Murray, R. Wang, H. Alizadeh, F. Pinheiro, L. Dal Negro, L. Sapienza, "Experimental investigation of light confinement in golden-angle, spiral photonic crystals", *in preparation*

Conferences

Peer-Reviewed Scientific Conferences

1. L. Sapienza, M. I. Davanço, T. Crane, O. J. Trojak, K. Srinivasan, "Bright and pure single-photon emission and efficient light confinement on a chip", *Latin America Optics and Photonics Conference*, Medellin, Colombia – **Invited Talk (2016)**

2. O. J. Trojak, J. D. Song, L. Sapienza, "Metallic microrings as scalable funnels for improved single-photon extraction", *UK Quantum Dot Day*, Edinburgh, UK – **Poster (2017)**

3. O. J. Trojak, J. D. Song, L. Sapienza, "Broadband emission enhancement of the extraction of light from solid-state emitters by metallic nanorings", *UK Semiconductors*, Sheffield, UK – **Talk (2017)**

4. O. J. Trojak, T. Crane, J. D. Song, L. Sapienza, "Nano-rings for improved extraction of single-photons and disorder-induced efficient visible-light confinement on a chip", *International Conference on Metamaterials, Photonic Crystals and Plasmonics (META17)*, Incheon (Seoul), South Korea – **Invited Talk (2017)**

5. O. J. Trojak, J. D. Song, L. Sapienza, "Metallic nano-rings for improved extraction of light from InAs/GaAs quantum dots", *International Conference on Optics of Excitons*, Bath, UK – **Poster (2017)**

6. O. J. Trojak, J. D. Song, L. Sapienza, "Metallic nano-rings for free-space extraction of light from single quantum dots", *OSA Frontiers in Optics*, Washington DC, USA – **Talk (2017)**

7. O. J. Trojak, T. Crane, L. Sapienza, "Disorder-induced light confinement in photonic crystals as a platform for efficient optical sensing", *OSA Frontiers in Optics*, Washington DC, USA – **Poster (2017)**

8. O. J. Trojak, T. Crane, L. Sapienza, "Efficient confinement of visible light in disordered photonic crystal waveguides", *OSA Frontiers in Optics*, Washington DC, USA – **Poster (2017)**

9. O. J. Trojak, J. D. Song, L. Sapienza, "Metallic nanorings for enhanced extraction of light from single InAs/GaAs quantum dots", *SPIE Photonics Europe*, Strasbourg, France – **Talk (2018)**

10. O. J. Trojak, T. Crane, L. Sapienza, "Anderson localization of visible light for high-quality on-chip optical cavities", *SPIE Photonics Europe*, Strasbourg, France – **Poster (2018)**

11. O. J. Trojak, T. Crane, L. Sapienza, "Optical sensing with Anderson localized light", *SPIE Photonics Europe*, Strasbourg, France – **Poster (2018)**

12. O. J. Trojak, C. Woodhead, J. D. Song, R. J. Young, L. Sapienza, "Metallic nano-rings for efficient, broadband light extraction from solid-state single-photon sources", *CLEO 2018*, San Jose, USA – **Talk (2018)**

13. O. J. Trojak, T. Crane, L. Sapienza, "Optical sensing with Anderson localized light", *CLEO 2018*, San Jose, USA – **Talk (2018)**

14. O. J. Trojak, T. Crane, L. Sapienza, "High-quality confinement of visible light in disordered photonic crystal waveguides in the Anderson-localized regime", *CLEO 2018*, San Jose, USA – **Talk (2018)**

15. O. J. Trojak, T. Crane, L. Sapienza, "Efficient confinement of visible light in disordered photonic crystals", *EOS Topical Meeting on Waves in Complex Photonics Media*, Anacapri, Italy, – **Invited Talk (2018)**

16. O. J. Trojak, C. Woodhead, J. D. Song, R. J. Young, L. Sapienza, "Metallic nano-rings to improve light extraction from single quantum dots", *Photon18*, Birmingham, UK, – **Invited Talk (2018)**

Symposia

1. O. J. Trojak, L. Sapienza, "On-chip quantum photonics structures for on-demand, bright and pure single-photon emission", *Zepler Institute Photonics Day: The Quantum Opportunity*, Southampton, UK – **Talk (2015)**

2. T. Crane, O. J. Trojak, L. Sapienza, "Quantum Optics in Coherent Artificial Systems", *Quantum Optics in Coherent Artificial Systems*, Romsey, UK – **Talk (2015)**

3. O. J. Trojak, T. Crane, L. Sapienza, "Nano-Scale Disorder: Turning an Obstacle into an Advantage", *International Day of Light Public Forum*, Southampton, UK, – **Poster (2018)**

4. O. J. Trojak, T. Crane, L. Sapienza, "Anderson-localization of Visible Light in Disordered Photonic Crystal Waveguides", *SPIE FOCUS Conference "Optics and Photonics Technologies"*, Southampton, UK, – **Talk (2018)**

Summer Schools

1. O. J. Trojak, L. Sapienza, "Nanometre-accurate positioning of single photon sources within nanophotonic devices", *QUICC Summer School*, Warwick, UK – **Poster (2015)**

2. O. J. Trojak, L. Sapienza, "Nanometre-accurate positioning of single photon sources within nanophotonic devices", *QLM Summer School 2015*, Totland, UK – **Poster (2015)**

3. O. J. Trojak, T. Crane, L. Sapienza, "Fabrication disorder: turning an obstacle into an asset", *QLM Summer School 2016*, Winchester, UK – **Talk (2016)**

4. O. J. Trojak, J. D. Song, L. Sapienza, "Nanometre-accurate positioning of single photon sources within nanophotonic devices", *QLM Summer School 2016*, Winchester, UK – **Poster (2016)**

5. O. J. Trojak, J. D. Song, L. Sapienza, "Metallic microrings as scalable funnels for improved single-photon extraction", *SEPNet Quantum Technologies School*, Liphook, UK – **Poster (2017)**

6. O. J. Trojak, J. D. Song, L. Sapienza, "Broadband enhancement of light by metallic nanorings", *QLM Summer School 2017*, Bournemouth, UK – **Talk (2017)**

7. O. J. Trojak, T. Crane, L. Sapienza, "Disorder-induced light confinement in photonic crystals as a platform for efficient optical sensing', *QLM Summer School 2017*, Bournemouth, UK – **Poster (2017)**

8. O. J. Trojak, "A Safari Guide to The Curiosities of Academic Publishing", *QLM Summer School 2018*, Southampton, UK, **Invited Talk (2018)**

Workshops

1. J. Kinsella, O. J. Trojak, "How can I get my community to talk to me? #sciroom", *Making an Impact (Research and Innovation Conference 2017)*, Southampton, UK – **Workshop (2017)**

2. J. Kinsella, O. J. Trojak, "How can I get my community to talk to me? #sciroom", *BIG STEM Communicators Network – BIG Event 2017*, Newcastle, UK – **Workshop (2017)**

Acknowledgements

Firstly I would like to thank my primary supervisor Dr. Luca Sapienza for his supervision over the last $3\frac{1}{2}$ years; without which, very little of any note would have been accomplished. I would also like to thank my secondary supervisor, Dr. Hendrik Ulbricht, for providing the use of one of his labs and his crazy ideas.

I have been fortunate to have had access to leading facilities at the Southampton Nanofabrication Centre, the Rapid Prototyping Facility and the Integrated Planar Cleanroom; and have guidance, advice and discussion with knowledgeable technicians: Zondy Webber, Kathleen LeBlanc, Peter Ayliffe and Neil Sessions. I have also had access to a very skilled workshop team: Philip Connell, Damon Grimesy, Paul Kinsey and Mark Skulley (mechanical workshop); and Gareth Savage and Gary Taylor (electronics workshop). The technical support team never seemed to tire of repeated demands for things to be done yesterday: Justin Harris, Cameron Murray and Tom Perkins; and the teaching lab staff allowed me to take unreasonable quantities of lab equipment whilst things were on order: Mark Ashley, Sanja Barkovic and Paul Martin.

A veritable Lazy Susan of undergraduate students have passed through the group, and have contributed to my work via discussion, help in the lab, simulation or by process optimization; 3 'Year of Experimental Research' Masters students: Henry Nelson, Tom Crane and Connor Murray; 8 Masters project students: Charles Pooley, Imogen White, Thomas Frank, Vincent Taylor, David Elcock, Liam Sharkey, Barnaby Sleat and Chris Meayers; and 9 summer students: Ben Burridge, Tom Crane (again), Barnaby Sleat (again), Hector Stanyer, Jason Tam, Jay Wroe-Brown, Josh Nevin and Chris White.

I have been fortunate to have worked with like-minded collaborators: Luca Dal Negro, Alizadeh Hossein and Ren Wang (Boston University, US); Felipe Pinheiro (Federal University of Rio de Janeiro, Brazil); Robert Young and Christopher Woodhead (University of Lancaster, UK); Stephen Hughes, and Juan Pablo Vasco (Queens University, Canada); Jin Dong Song (Korea Institute of Science and Technology, South Korea); Santiago Solares, Alfredo Diaz Gonzalez (George Washington University, US); and Kartik Srinivasan (National Institute of Standards and Technology, US).

I should begrudgingly acknowledge the support of my long-suffering housemates Amy, Andrea, Rex and Sen Ta (all of whom are fellow students) for the many late-night discussions about the intricacies of nano-fabrication, why things won't work and the other more irrelevant things. Colleagues in my office have provided valuable discussion and procrastination when things in the lab stopped making sense, in particular Jeff and Steve. I should also thank a colleague that I met whilst at a SEPNet workshop for the moniker of 'Pineapple Rings' to describe the nanoring devices.

I am greatly indebted to the authors and contributors to the countless number of open-source software packages that I have extensive use of in my research, to mention a few specifically: linux, matplotlib [1] and python.

Lastly, none of this work would be possible without financial support from research funding agencies: Engineering and Physical Sciences Research Council (EPSRC), The Royal Society, and the Zepler Institute.

Chapter 1

A Retrospection

> Let's start at the very beginning,
> a very good place to start.
>
> Rodgers and Hammerstein
> *The Sound of Music (1959)*

EARLY ideas on optics were developed in ancient Greece, with the atomist and mediumist schools of thought competing with each other, a competition that went substantially unresolved for $\sim 1,000$ years [2]. Empedocles and Democritus believed in the visual fire: a fire inside the eye that went forth and interacted with objects (and rays from other fires, such as the sun or candles) and returned to the eye, giving us vision. The competing viewpoint was the atomist idea: that we perceive things as an interaction of 'atoms' striking the object and then eye. Aristotle (a student of Plato, who believed in the visual fire), reasoned that the visual fire would be unable to reach the stars instantly, so rubbished the idea. He proposed that light rendered the medium between the object and observer transparent. Despite differing ideas of how light worked, there was an implicit understanding of geometric optics, this was formalized by Euclid [3], and later extended by Ptolemy.

The ideas from ancient Greece went substantially unchallenged well into the Medieval period, when Ibn al-Haytham (anglicised as Alhazen) published his 'Book of Optics' [4]; in which he argued that the emitted light from the eyes was an unnecessary complication. He also argued that light had a finite speed, developed early ideas about refractive indices, and used geometry to describe refraction. Later scholars then extended his work and arrived at descriptions of rainbow formation.

Optical theories progressed slowly until the 1600s, Kepler investigated the functioning of the eye, tried to find an explanation for refraction[2]. He championed the idea that light activated the colour of objects, instead of rendering them transparent. In the late 1600s, Newton began his work on optics, culminating in his 'Book of Opticks' [5]. His experiments on refraction showed that white light was made of indivisible colours [6], and his experiments on refraction led him to determine that refracting telescopes were inferior, and instead invented the reflecting telescope. Despite observing the phenomena known as 'Newton's Rings', he disregarded the wave explanation for the propagation of

light. He later openly supported the corpuscular concept of light propagation (analogous to modern photons), which became the dominant viewpoint for the rest of the 1700s.

Huygens proposed a wave model of light in the 1670s [7], and it was this that originally spurred Newton to publish his work. This described light propagation in a manner identical to that of waves on the surface of a body of water. A wavefront propagates by the radiation and interference of individual wavelets. This was able to explain refraction, and a number of other interference phenomena. In 1801 Young presented the Bakerian Lecture [8] in which he examined the weight of evidence against the particle theory of light, including: the colours of thin films and scattering from scratches, two things Newton was unable to explain and glossed over; the existence of diffraction from edges, which Newton incorrectly determined to be non-existent; and a wave-based explanation of the Newton's rings phenomena. This was met with consternation by the British scientific establishment as Newton's ideas were held in high regard over the imported wave hypothesis. Young presented his famous double-slit experiment in the Bakerian Lecture two years later in 1803 [9]; despite the most compelling evidence for the wave description of light, some members of the scientific establishment remained unconvinced, such was the reputation of Newton.

The wave description of light was further cemented by Fresnel in 1818, in a memoir he submitted to the 1819 physics Grand Prix; in which he was able to fully explain: diffraction; the new experimental results on polarization; and the birefringent behaviour of calcite (which despite being explicitly mentioned in the title of Huygens work, was not adequately explained) [2]. Poisson, in an attempt to discredit the wave hypothesis, found using Fresnel's work that a bright spot should appear in the centre of a shadow of a circular object – a clearly absurd outcome! Experiments by Arago, confirmed the presence of this spot, and in so proved that the wave hypothesis was able to predict unseen phenomena. The wave hypothesis was fully formalized by Maxwell in 1865 [10], where he joined together parallel work on electricity and magnetism; showing that they were manifestations of a single electromagnetic field, which propagated at the speed of light.

Throughout the history of the wave theory of light, it was universally agreed that as a wave, there must be a medium of propagation – the luminiferous æther. To allow light such a high speed this æther must be incredibly stiff, yet pervade all of space – a very unusual set of properties. In 1887 Michelson and Morley attempted to measure the speed of the Earth relative to this æther, however they returned the now-famous null result [11]. As far as they could tell, the æther was not moving regardless of how the Earth moved through it. Either the universe was geocentric (which it clearly was not), or æther (and subsequently a universal reference frame) did not exist. It was not until 1905 when Einstein proposed a description of a relativistic universe [12, 13], where the speed of light is a constant upper limit on velocity, that this was æther was completely dispensed with; relativity also proved to be compatible with Maxwell's equations anyway.

The wave theory was also being attacked from the other end of the size scale. In 1900 Rayleigh proposed the λ^{-4} dependence of what is now called the Rayleigh-Jeans law to describe the emission spectrum of light from hot objects, black body radiation. This was an asymptotic description, where the integral over the whole spectrum is infinite – a non-physical result. Planck

proposed a new description in 1901 [14], where energy is exchanged with the electromagnetic field in discrete packets of energy – quanta. This signalled the start of the quantum age, and in 1905 Einstein proposed the existence of the photon to explain the emission of cathode rays from charged surfaces under ultra violet (UV) light – the photoelectric effect [15]. It was later proved that this can be explained semi-classically with only quantized atomic energy levels [16], this would have been known at the time, and shows that the scientific community felt a need for the photon to exist. The final, no-strings-attached experimental proof of the photon came in 1977, with single photon emission from Na atoms [17].

Meanwhile the behaviour of previously deterministic particles was being challenged. In 1923 de Broglie unified relativistic photon momentum with quantum photon energy to produce the prediction of matter waves – wave-like behaviour of particle-like objects [18]. Also in 1923 Compton conducted X-ray scattering experiments which showed the interaction of momentum between photons and matter [19]. Then in 1927 G. P. Thomson showed that electrons could be diffracted by thin films of metal, producing wave-like interference patterns [20][1] [21]. This left our understanding of light and matter thoroughly jumbled together, with both showing particle- and wave-like properties.

[1]Such a ground-breaking result was, initially, published as a rather short letter to the editor, next to a letter complaining about misrepresentation of government committee reports; a manner which resembles todays correspondence sections.

Chapter 2

Light-Matter Interaction

> "Since there's no ending quote mark, everything after this point is part of my quote.
>
> Randall Munroe

The interaction of light with matter is is fundamental to photonics, as this is how photons are generated, detected and put to work. The modern picture evolved out of the photoelectric effect [15], where photons interacted with a quantized atom. This was later refined to utilize advances in quantum theory [22], where the interaction can be modified. Things have progressed, with artificial atoms providing more ways of controlling the interaction, whilst opening up advances in solid-state fabrication to photonics. Key to all of this is the photon.

2.1 Single Photons

2.1.1 Photon Statistics

Before we begin discussing the intricacies of different single photon sources and their applications it should first be established: what is a single photon and how this differs from classical light.

Let the experiment in Figure 2.1 be considered: a light beam incident on a single-photon sensitive detector, with suitable counting electronics. Within any given time window, t (as shown), a number of photons fall onto the detector and are registered as a detection; in the schematic this is shown as a distance. The average number of counts is determined by the beam intensity, with the count rate fluctuating around this value. A naïve interpretation is that as the detector can resolve single photons, we now have proof that the incident beam is made up of single photons; however, the devil is in the detail. In this case, the detector is not photon number resolving; it does not tell you how many photons it has detected, just that there was something to detect. So in the time-window t, 8 photons would fall upon the detector, and a single count would be registered.

We can now examine what happens if we try to create what intuitively appears to be an obvious single photon source, a very dim light source. To

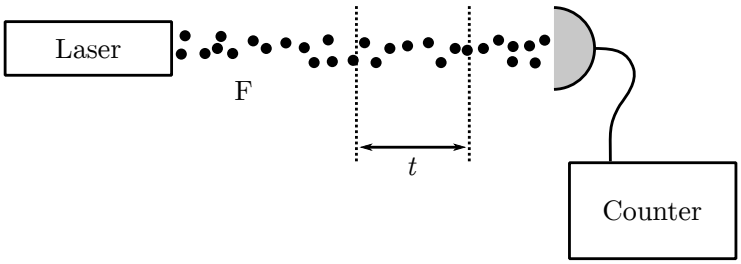

Figure 2.1: Schematic of a coherent light source emitting photons, which are directed upon a single-photon-sensitive detector. The distance indicated corresponds to the time window t.

create our very dim source, all we need to do is place a neutral density filter in the path of the photons (at position F in Figure 2.1); this has the effect of reducing the mean value of photons in the time interval t. The behaviour of photons in such a discrete random system is described by Poissonian statistics [23]: which describe the probability of a number of events occurring in a given time if each event is independent of the last and they occur at a nominally constant rate over large values of t. The probability of k events occurring, for a given expected event rate of λ is:

$$P(k) = \frac{\lambda^k e^{-\lambda}}{k!} \tag{2.1}$$

If this distribution is plotted for $\lambda = 10$ (yellow in Figure 2.2), the most likely number of events to occur in time t is 10, we get a spread of possible numbers of photons on the detector. If we now return to the attenuated laser, the attenuation reduces the intensity, which is manifested as a decrease in the expected occurrence, λ, on the Poisson distribution. Figure 2.2 shows the distribution $P(k)$ as λ is decreased. The numbers of photons on the detector falls, with $\lambda = 1$ providing single photons $\sim 37\%$ of the time. However, as λ is decreased, not only do the single photon events increase in frequency, the no-photon events do as well. Worst still, there is a non-zero probability of 2, 3 and 4 photon events. Such multi-photon events are detrimental to many potential applications, such as quantum cryptography where it introduces a potential attack vector. Increasing the attenuation further still makes the problem worse, as the single photon events are reduced. So an attenuated multi-photon light source is a bad choice for a single photon source: it will be very dim (with may zero photon events), it is not deterministic (we have no certainty that we will receive a photon), and it will not be pure (as multi-photon events are still possible). We need some light source which does not obey these Poisson statistics, a sub-Poissonian source.

2.1.2 Characterizing Single Photon Sources

Single Photon Purity

To quantify how pure a given single photon source is (i.e. if it emits single photons or if it occasionally emits two or more photons simultaneously), a quantity

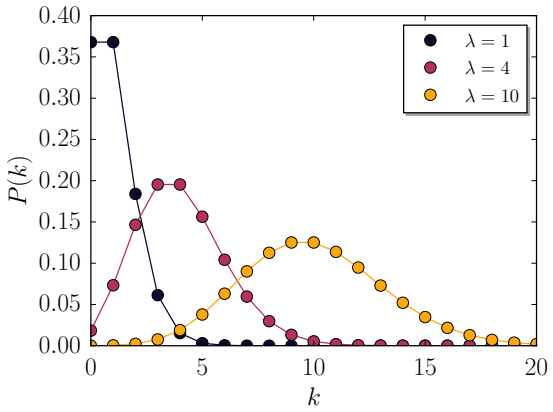

Figure 2.2: Poisson probability mass function, $P(k)$, showing the relative probability of occurrence of k for varying vales of expected occurrence, λ.

called the second order coherence function, $g^{(2)}(\tau)$, is measured [23]:

$$g^{(2)}(\tau) = \frac{\langle I(t)I(t+\tau)\rangle}{\langle I(t)\rangle\langle I(t+\tau)\rangle} \tag{2.2}$$

where $I(t)$ is the intensity of the light beam at time t; τ is a variable time delay used to examine the variability of $g^{(2)}(\tau)$; and $\langle ...\rangle$ indicates that the measurement is averaged over a long integration time, this is done to reduce shot noise.

To experimentally measure $g^{(2)}(\tau)$, a Hanbury-Brown and Twiss (HBT) experiment is performed [24, 25, 26]. The key feature of this experiment, Figure 2.3, is a 50:50 beamsplitter. A beam of light for analysis is directed into the beamsplitter. Light can leave the beamsplitter by one of two paths, and any given photon can only exit the beamsplitter from one path. The two exiting beam-paths are each directed onto a single photon avalanche photo-diode (SPAD). Therefore any incident photon will enter the beamsplitter, leave by one of the exit ports and produce a 'click' on the corresponding detector. If two photons enter the beamsplitter, they can leave by different ports, causing simultaneous 'clicks' in both detectors. For light made purely of single photons, such coincidences of detection cannot occur.

By adding an electronic delay, $\Delta\tau$, in the signal line from one of the detectors, the relationship of coincidences can be observed. Figure 2.4 shows a plot of coincidences from an excitation source driven with a pulsed laser. At $\Delta\tau = 0$ there are almost no coincidences between the detectors. As $|\Delta\tau|$ is increased, coincidences between two temporally separated photons become visible. Due to the pulsed excitation used, coincidences can only be seen with a periodicity matching that of the excitation repetition rate. Graphically, a series of periodic peaks is seen, with the central peak at $\Delta\tau = 0$ missing.

The value of $g^{(2)}(0)$ is used to determine the single photon purity, Table 2.1 shows a comparison of $g^{(2)}(0)$ values for various sources. A value of $g^{(2)}(0)$ less than one indicates a degree of single photon emission and the source is called anti-bunched, whereas multi-photon light is called bunched.

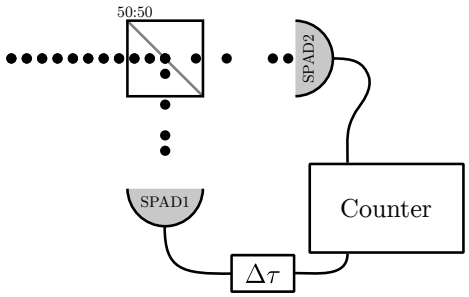

Figure 2.3: HBT experiment schematic. A pair of SPADs detect photons output from the two paths of a beamsplitter. An electronic delay, $\Delta\tau$, is applied to one of the signal lines. A counter records coincidence events.

Emission Type	$g^{(2)}(0)$
Chaotic	$1 <$
Coherent	1
Non-classical	< 1
Majority Single Photon	$< \frac{1}{2}$

Table 2.1: Comparison of $g^{(2)}(0)$ for different light emission sources.

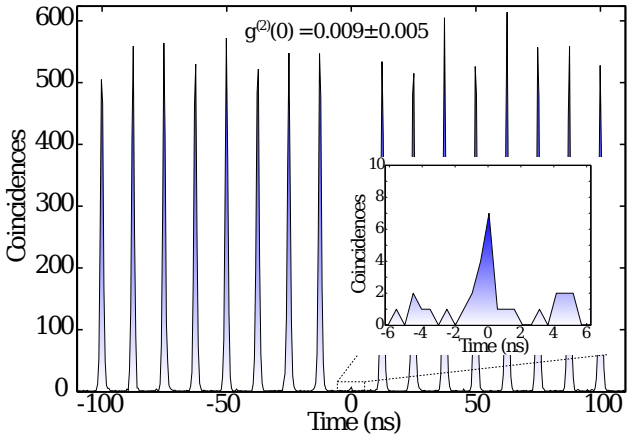

Figure 2.4: Coincidence plot of the emission produced from an InAs/GaAs quantum dot within a micro-cavity, measured using a HBT experiment. The missing peak at $\Delta\tau = 0$ is the signature of single photon emission, in this case $g^{(2)}(0) = 0.009 \pm 0.005$. Reproduced from [27], under a CC-BY 4.0 licence.

Indistinguishability

Fundamentally, indistinguishability is the inability to tell two photons apart; i.e. two photons have identical wavepackets [28]. The indistinguishability of two photons is characterized by the overlap of their wave-functions. If the wave-functions overlap perfectly, two photon interference can be observed. Most proposed applications of single photons in quantum technologies make use of two-photon interference: quantum computation [29], quantum teleportation [30], and entangled photon production [31].

A Hong-Ou-Mandel (HOM) experiment [32] can be carried out to determine the indistinguishability of photons from a source. In a HOM experiment, Figure 2.5, the single photon beam is split into two paths; one of which has a variable delay line. These paths converge on two input ports of a 50:50 beamsplitter, with a pair of SPAD detectors placed at the output ports. If two photon interference occurs then both photons leave from the same output port, resulting in a lack of coincidence counts between the detectors. The delay path length can be changed to alter the temporal overlap, this reduces interference and increases coincidence events observed. An example plot from a HOM experiment is shown in Figure 2.6. Recently, a demonstration of the HOM effect where images were taken of the output ports of the beamsplitter has been made – showing the photons leaving the ports as pairs [33].

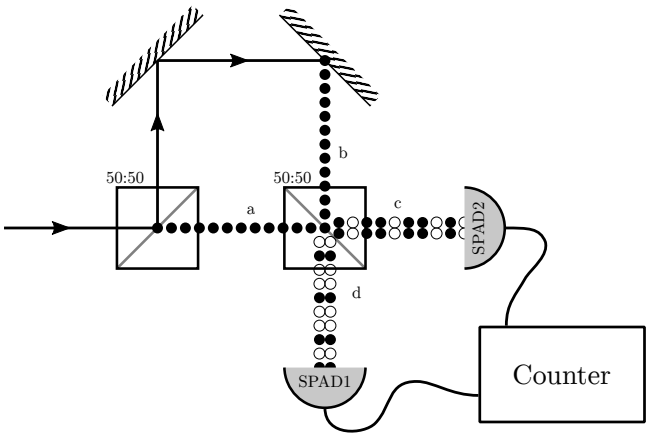

Figure 2.5: Schematic of a HOM experiment. Input light is split into two paths, one of which is of adjustable length. The filled dots represent the position of photons, whereas unfilled dots are the absence of a photon. These paths re-combine in a beamsplitter. If two indistinguishable photons are incident on the beamsplitter, they will bunch together upon output. If the photons are indistinguishable, coincidences detected between the output ports should not be observed.

The two photon interference at the beamsplitter can be understood intuitively by examining the paths of the photons (the labels of the beamsplitter ports are shown in Figure 2.5). There are four possibilities (shown as terms left to right in Equation 2.3): (1) photon a is transmitted and photon b reflects; (2) both photons are reflected; (3) both photons are transmitted; (4) photon a is reflected and photon b is transmitted. Due to a phase change upon reflection from the beamsplitter surface for photons from side a, the two terms where photons exit via both ports cancel, as shown in Equation 2.4 [35]. In the equations

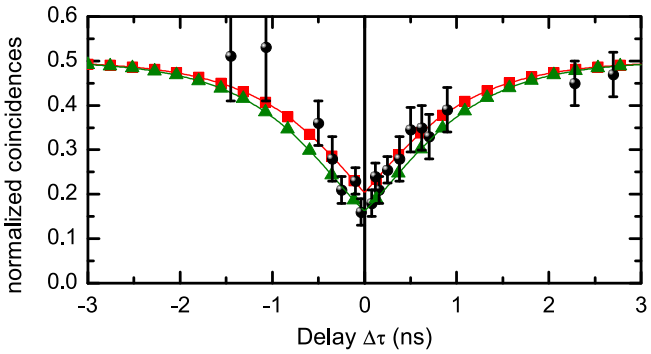

Figure 2.6: Coincidence plot from a HOM experiment. The presence of a dip in coincidences indicates indistinguishability. Reprinted with permission from [34], © 2014 American Physical Society.

below, the notation $|2,0\rangle_{\mathrm{cd}}$ indicates that a photon pair exits from port c.

$$|1,1\rangle_{\mathrm{ab}} = \tfrac{1}{\sqrt{2}}|2,0\rangle_{\mathrm{cd}} + |1,1\rangle_{\mathrm{cd}} - |1,1\rangle_{\mathrm{cd}} - \tfrac{1}{\sqrt{2}}|0,2\rangle_{\mathrm{cd}} \tag{2.3}$$

$$|1,1\rangle_{\mathrm{ab}} = \frac{|2,0\rangle_{\mathrm{cd}} - |0,2\rangle_{\mathrm{cd}}}{\sqrt{2}} \tag{2.4}$$

2.1.3 Applications of Single Photons

Single photons have a number of applications within '2^{nd} generation quantum technologies'; so-called because the devices exploit quantum phenomena. This is in contrast to technologies enabled by an understanding of quantum mechanics, the '1^{st} generation', i.e. semiconductor material in a transistor. Quantum technologies offer ways of exceeding the limits of classical technology, to realize: computers orders of magnitude more powerful, encryption with guaranteed unreadability, and techniques to side-step classical detector noise for more sensitive measurements. Several prominent quantum technologies shall now be considered: computing, cryptography, teleportation, metrology, and imaging; and by combining several of these technologies together, a so-called quantum internet is possible [36].

Quantum Computing

Classical computing uses binary digits, 1 and 0, to represent information. In quantum computing the infinite variability of the wave-function of a two level system, the qubit $|\Psi\rangle$, is exploited:

$$|\Psi\rangle = \alpha|0\rangle + \beta|1\rangle \tag{2.5}$$

where α and β are the amplitudes of the states $|0\rangle$ and $|1\rangle$, which can take an infinite number of value combinations such that:

$$1 = \alpha^2 + \beta^2 \tag{2.6}$$

This is particularly attractive as the limits of classical computers are now becoming clear, as the cost and difficulty of fabricating ever-smaller circuits is quenching the growth in performance [37]; with flaws and errors being discovered in ever-more complex processor architectures, requiring performance cuts to remedy [38]. A number of algorithms have been developed for quantum computers which provide reductions in the compute-time required for some specialized tasks: Shor's algorithm [39] is able to factorize numbers in polynomial time ($t \sim \log N$) compared to classical algorithms which scale $\sim e^{\log N}$; Grover's quantum search algorithm [40] scales $\sim \sqrt{N}$ whereas classical ones scale $\sim N$.

There are several design requirements for a quantum computer [41, 42]:

1. A system of 'well-characterized' qubits is needed, where their Hamiltonians are well understood and which can be initialized into a well defined state.
2. A means of initializing the qubits, to an initial state such as $|000...\rangle$.
3. Some unitary operator must exist that allows a transformation from the initial state to an arbitrary entangled state.
4. The de-coherence times of the qubits must be much longer than the time to perform operations upon them.
5. Lastly, the coupling of the qubits to the environment should be able to be switched on and off at will.

This last requirement means the system is decoupled from the environment during the computation and is strongly re-coupled for readout.

Current quantum computers make use of superconducting circuits to trap qubits [43], with 10 qubit systems now reported [44]. The main draw-back with superconducting systems is in isolating them from the environment during the computation, as residual nuclear spins radically shorten conference times, with 60 µs being the current upper limit [45]. Now systems where individual trapped ions are shuttled between quantum interaction sites are being considered [46]. Commercial annealing machine systems, such as those by D-Wave have become available, but are marred by reports that they do not offer performance improvement over classical systems [47]. IBM has made a 5-qubit system available for paying customers [48].

Photon-based quantum computers do not suffer from the de-coherence effects that plague other systems such as nuclear magnetic resonance (NMR) [49], and are not susceptible to thermal noise. They also offer direct integration to optical telecommunication systems, and are able to route information through at the speed of light, as well as bringing all of the benefits of being a solid-state monolithic system. A significant problem with optical qubits is the difficulty of realizing a controlled NOT gate (CNOT) [50], where a qubit is flipped if a control signal is applied. Logic gates acting upon polarization exploit birefringent materials, a CNOT requires a switch-able birefringent material which should ideally switch instantly. Another large barrier to overcome is that photons interact weakly with each-other; and, as demonstrated with the HOM experiment, need to be indistinguishable to do so.

Quantum Encryption

A more direct use of single-photons lies in cryptography. Quantum encryption relies upon the no-cloning theorem [51], which prohibits an exact copy of a quantum state to be transferred to a second body whilst retaining the first. This means that if single photons are used to encode a message, then any intercept will manifest itself as bit errors in a message. A pure single photon source is crucial, as double-photon emission would provide a means for the message to be intercepted unnoticed.

The most popular application of quantum cryptography is in quantum key distribution (QKD) [52]. This is where an encryption key is sent securely through quantum channels, to be used to encrypt messages sent through classical communication channels. The key acts as a one-time-pad, where an exclusive OR (XOR) is used to encode the message with a key string the same length; decryption is the reverse process. Messages sent this way are completely secure provided the key sequence remains secret.

The first proposed QKD protocol was BB84 [53][1]. In this protocol two parties, Alice and Bob, wish to communicate securely and have access to a classical, unencrypted communication channel. BB84 uses an additional quantum channel to distribute the key from Alice to Bob. Down this quantum channel Alice sends single photons, onto which she has encoded information using a set of orthogonal bases, e.g. crossed and anti-crossed polarization. Due to the no-cloning theorem, an eavesdropper, Eve, is unable to intercept a photon from the message and replace it without detection. If Eve intercepts a photon she has a 50:50 change of choosing the correct basis to measure in before re-sending a replacement photon, so at best she introduces a 50% error on every intercepted photon. Once a complete key message is sent, Alice sends the polarization basis to Bob, who checks his observed bases. He keeps only those results where he has measured in the same basis that Alice sent in. A small number of these 'correct' measurements are openly declared so that the error rate can be determined. If the error rate is low enough, then the key can be trusted. From here privacy amplification techniques can be used, and error corrections applied. The distributed key can now be used as a one-time-pad for secure communication over the classical channel. Since BB84, many other protocols have been proposed [55], which attempt to provide protection against imperfect single photon sources.

The first demonstration was made in 1989[2]; where, after distillation, a key of 443 bits were shared over 30 cm [56]. Subsequent demonstrations have followed [52]. Fibre-based QKD systems can leverage existing optical fibre infrastructure to send keys across metropolitan areas [57]. Free-space demonstrations concentrated on distances of ~ 150 km, [58], which may seem too short to be useful, but are representative of the atmospheric attenuation a ground-to-satellite system would experience. Indeed, the first demonstration of ground-to-satellite QKD was reported in 2017 [59]. This has opened the door to a global QKD satellite network, allowing keys to be exchanged between sites anywhere in the world.

[1] A more accessible, and tasty, description involving chocolates can be found in [54].

[2] Using a humble light emitting diode (LED) as a photon source (the only laser in the lab was used for alignment), they achieved 0.34 photons per pulse.

Quantum Teleportation

As mentioned earlier, the no-cloning theorem forbids the copying of a quantum state to another body whilst retaining the first. Quantum teleportation is a phenomenon that occurs when you do this copying, but destroy the first [60].

Alice has a photon ($|\psi\rangle_1$) which can be either horizontally ($\leftrightarrow$) or vertically ($\updownarrow$) polarized:

$$|\psi\rangle_1 = \alpha\,|\leftrightarrow\rangle + \beta\,|\updownarrow\rangle \tag{2.7}$$

She wishes to send this state to Bob, but no single measurement will be able to fully describe both orthogonal states at the same time. To fully communicate the state to Bob, it must be teleported. An Einstein-Podolsky-Rosen (EPR) photon pair is generated, and shared between Alice ($|\psi\rangle_2$) and Bob ($|\psi\rangle_3$), the important property here is that if one photon is measured, the other entangled photon immediately collapses into the complimentary state. Alice performs a Bell-state measurement between her initial photon and her entangled photon; this entangles them together, consequently entangling Alice's initial photon in state $|\psi\rangle_1$ with the photon Bob has, whilst destroying Alice's photon. As photon 2 is complimentary to 1 and 3, it follows that $|\psi\rangle_1 = |\psi\rangle_3$.

Key to this is a single photon source that can emit EPR entangled photons [61], multi-photon events will destroy the entanglement. The first experimental demonstration was made in 1997 [30], with the more spectacular demonstration of ground-to-satellite teleportation made in 2017 [62].

Quantum Metrology

Another application is quantum metrology, which uses quantum effects to realize precise measurements. Fundamentally, any measurement technique is ultimately limited by the Heisenberg uncertainty principle [63]; however, in practice, classical measurement schemes are limited by shot noise [64] which is of order $\frac{1}{\sqrt{N}}$. Entangled photons in 'N00N' states can be used with Mach-Zehnder interferometers, where the phase change between arms of the interferometer is measured, to lower the noise floor to the order of $\frac{1}{N}$ [65]. In these schemes, single photons are used in the generation of the input entangled states.

Ghost Imaging

Ghost imaging is a technique where a sample is imaged using light which has not actually interacted with the sample [66]. It relies on a photon pair to be generated, an imaging photon and an interaction photon. To conserve momentum, the photons have complimentary paths which are deterministic. By placing a camera to detect the spatial position of one photon, it is possible to know the path of other as well. The interaction photon is directed onto a sample to be 'imaged'. A single pixel, single-photon-sensitive detector is used to detect if this photon has made it past the sample, if it is transmitted. This detection signal is used to gate the camera, so only spatial positions of transmitted photons are recorded. Through this process, a transmission image of the sample can be built-up. This technique has two advantages over conventional imaging techniques: firstly low photon fluxes can be used, $\sim 100,000$ photons, which allows for minimal damage of sensitive samples such as cells; secondly, the photon pair production does not have to generate photons with identical wavelengths,

allowing imaging at a wavelength where silicon cameras have peak sensitivity, and probing at a different target wavelength.

2.1.4 Single Photon Sources

Single photons have been generated from a number of sources, including solid state systems. These are summarized in Table 2.2.

Source	λ [nm]	τ [ns]	$T_{\max}$ [K]
Trapped Atoms/Ions	$*$	30	†
Molecules	Visible	3	R.T.
Diamond NV Centre	637	11	R.T.
Carbon Nanotubes	860-880	200	R.T.
WSe_2	700-800	~ 2	4.2
SFWM	‡	N/A	R.T.
GaAs QDs	850-1300	$\sim$1	40
Colloidal QDs	Visible to NIR	20-30	R.T.

Table 2.2: Summary of sources of single photon emission. Showing typical emission wavelength (λ), photon lifetime (τ) and the maximum operating temperature ($T_{\max}$). R.T. $\equiv$ room temperature.
*Note that in trapped atom/ion systems the emission wavelength depends on the atomic species used. †Trapped atoms are laser cooled under ultra high vacuum. ‡Photon wavelengths can be tuned relative to pump wavelength.

Trapped Atoms

The most basic of all systems to realize single photons are single atoms; with single atoms used as the source in the first experimental demonstration of single photon generation [17]. These provide the most replicable system; as, for a given atomic species, one atom is the same as the next – whereas systems that are made from many atoms suffer variations between individual emitters. Single atoms have sharp bandwidths, in the order of MHz [67], which are lifetime limited[3]. Currently trapped-atom systems require bulky lasers and optics to cool and manipulate the atoms, and ultra high vacuum systems to contain them; this severely limits portability and potential applications, though efforts to miniaturize the technology are under-way [68]. The long photon lifetime of 30 ns limits the repetition rate of the source, restricting useful applications [69]. Devices which couple trapped atoms to cavities to decrease photon lifetimes have been demonstrated [70], but are technically challenging.

Molecules

Molecules were the first solid-state system where single photon emission was observed [71]. Molecules have vibrational states in addition to electronic states, due to their relatively complex geometries. The only non-broadened emission

[3]The relation $\Delta E \Delta t \gtrsim \hbar$ links the uncertainties in energy (E) and time (t); by rearrangement, the line-width ($\Delta\omega$) is given by $\Delta\omega \gtrsim \frac{1}{\tau}$, where τ is the photon lifetime.

from molecules occurs at the zero phonon line (ZPL), a transition between electronic excited and ground states at the vibrational ground state [72]. Due to their complex electronic structures, molecules suffer from blinking when emission is quenched by electrons becoming trapped in dark states. Dark states are energy states of a system which cannot emit photons. As molecules can be reactive, they are also susceptible to bleaching, where they oxidise and stop emitting [73].

Colour Centres

Colour centres are defects within a crystal lattice, so-called because they absorb specific wavelengths giving the crystal colour [74]. The most studied for quantum optics applications is the nitrogen-vacancy (NV) centre in diamond [75]. The NV centre is a vacant node in the diamond crystal lattice, next to a nitrogen atom; this causes a surrounding carbon atom to only have 3 bonds, forming a charge in the NV region. NV centres are typically made in bulk by bombarding a nitrogen-rich diamond with electrons to dislocate carbon atoms and form vacancies. A thermal annealing process, operating in excess of 600°C allows the vacancies to move and form a stable NV complex. NV centres in diamond are sensitive to etched features nearby – placing a limit on minimum device size. Diamond also has an indirect bandgap of 5.5 eV, which forms a large phonon side-band at longer wavelengths to the ZPL emission line from the NV centre [76]. Diamond is attractive as the NV centre exhibits room temperature single photon emission, diamond is biologically compatible, and can now be synthetically synthesized [77]. The main disadvantage of diamond-based devices is the difficulty of fabrication. Diamond is resistant to most chemical and mechanical processes, which severely constrains device design. To realize complex devices, such as those with suspended structures, various techniques have been used: focussed ion beam milling [78]; angled etching [79]; bottom-up fabrication [80]. Nanodiamond particles, with a diameter anywhere between 10-30 nm have been developed[4], allowing the colour centres themselves to be integrated into other material platforms [82].

Carbon Nanotubes

Carbon nanotubes (CNTs) were observed to emit single photons in 2008 [83]. With emission wavelengths in the near infrared (NIR) regime at ∼865 nm. Recently room temperature operation has been realized using a dopant group attached to the CNT [84]. CNTs are grown by chemical vapour deposition (CVD), in a relatively uncontrolled growth process [85]. This results in variability in length, diameter and electronic configuration (conducting or semiconducting) of the CNTs. CNT suffer from a low quantum yield, due to the existence of dark states the lie below the optical transitions of the defect sites [86]. These factors limit current applications.

2D Materials

Since graphite was shown to exist in stable single-atom-thick sheets, called graphene, in 2004 [87], a range of different 2-dimensional (2D) materials have

[4] You can even make them at home [81]!

been developed [88]: MoS_2, WS_2, $MoSe_2$, WSe_2, $MoTe_2$ and hexagonal boron nitride. Single photon emission has been reported from defects in a WSe_2 sheet [89]. 2D materials offer photon emission in the visible and NIR, with line-widths down to 120 µeV. There are two primary techniques for preparing monolayers for integration into devices: exfoliation and CVD growth. Exfoliation is a process where flakes of the bulk materials are stripped off by repeated use of adhesive materials such as sticky tape. This method is rather hit-and-miss [90], with large variation in flake sizes. CVD allows direct growth of monolayers, however removal of the monolayers from the growth substrate results is small flakes [91]. Both preparation methods result in small flakes with variable quality, limiting the scalability of devices based on such 2D materials.

Non-linear Photon Conversion Schemes

The current workhorse single photon source for quantum information experiments is some type of non-linear conversion: parametric down-conversion (where one photon is converted into two photons with total energy equal to that of the input) or spontaneous four-wave mixing (SFWM). The main drawback of these techniques is that they are stochastic, hence heralding is used: as multiple photons are generated at the same time, one of these is detected to announce or herald the arrival of a single photon in the experiment. This is perfectly acceptable to many experiments where a single train of single photons are required, but for large-scale quantum information devices, multiple photons are required simultaneously on-demand. SFWM is typically generated within fibres [92] or in resonators [93]. Some efforts to integrate multiple sources on-chip have been made, but the stochastic nature of the sources has not been addressed [94]. The need for such quantities of photons has lead to the investigation of quantum memories, where generated photons are stored until needed [95].

InAs/GaAs Solid State Quantum Dots

Solid state quantum dots (SSQDs) offer a number of advantages compared to other systems. GaAs is already used in the fabrication of micro-electronics, so any process can take advantage of the research already done to perfect fabrication technologies. Also, as electronic devices are already produced in GaAs, it is relatively simple to fully integrate emitters into electronic devices.

Such solid state quantum dot (SSQD) emitters are chemically stable compared to other technologies. The quantum dots are encapsulated into a wafer, sealing them from the environment. This prevents chemical processes such as bleaching from occurring. This also permits stable emission over time-spans of years, unlike molecule or colloidal quantum dot systems. SSQDs can suffer from blinking, but this occurs on short time-scales ($\sim$10 ns-10 ms) and to a lesser extent compared to other emitter systems [96]

A popular mechanism for the growth of SSQDs is the Stranski-Krastanov (SK) technique [97], Figure 2.7. Upon a GaAs substrate, a wetting layer of InAs is deposited using molecular beam epitaxy (MBE), Figure 2.7a. This growth is performed slowly, allowing the InAs lattice to conform to the lattice spacing of the GaAs substrate. The InAs lattice is 7% larger than that of the GaAs [98]. After a critical thickness of 1.75-3 monolayers [97, 99], it is thermodynamically more favourable for the InAs to nucleate into islands rather than remain in

strained layers, Figure 2.7b. These islands are small, ∼10 nm, as shown in Figure 2.8; structures on this scale are effectively zero-dimensional, they retain atom-like properties such as: discrete transitions, and they are subject to the Pauli exclusion principle. A capping layer of GaAs is grown on the top of the islands to encapsulate them, Figure 2.7c, this encapsulation creates a potential well for confinement of charge carriers.

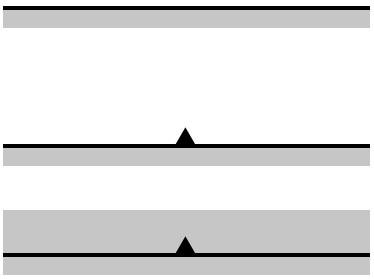

(a) An InAs wetting layer (black) is slowly grown on a GaAs substrate (grey).

(b) Strain builds in the InAs layer, due to a lattice mismatch, causing it to fail. This produces islands of InAs (the triangle).

(c) A capping layer of GaAs is grown on top of the InAs islands.

Figure 2.7: Schematic of Stranski-Krastanov method for the growth of SSQDs.

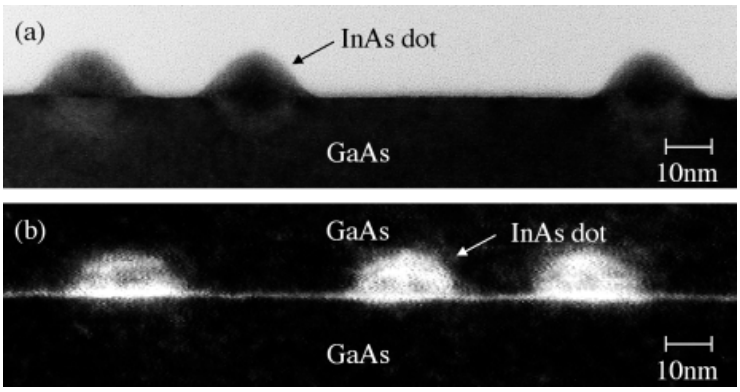

Figure 2.8: Transmission electron micrograph cross-section of InAs/GaAs quantum dots. (a) Shows uncapped InAs islands on GaAs substrate; (b) shows InAs islands with a GaAs capping, the wetting layer can also be seen as a thin layer. Reproduced with permission from [100].

The InAs quantum dot forms a region of low band-gap within the high-band-gap GaAs substrate, Figure 2.9. When the GaAs is excited with an above band-gap photon, an exciton (an electron and hole pair) can be created. The exciton can move to the low band-gap dot, where it can recombine, emitting a photon of lower energy compared to the excitation. The excess energy is lost to the crystal lattice as phonons. As the quantum dot is small, ∼10 nm as shown in Figure 2.8, multiple excitons are held sufficiently close that they can interact via the Coulomb force; this interaction causes bi-exciton states (states with two excitons) to emit at different wavelengths.

A drawback with SK growth is that the distribution of the islands is random, as it is driven by a spontaneous nucleation process. This is illustrated in the photoluminescence (PL) map in Figure 2.10. Also, to guarantee a region of the

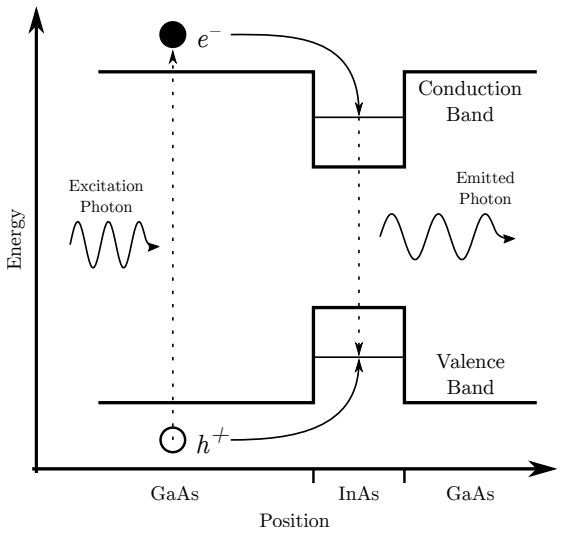

Figure 2.9: Schematic of the energy bands of an InAs/GaAs quantum dot, showing the excitation-emission process. The position axis shows a vertical line-cut across a quantum dot. h^+ is a positively charged hole or vacancy, and e^- is an electron.

desired QD density, the wafer rotation is stopped during the monolayer growth, allowing a density gradient to form.

To address the random growth, techniques have been developed to allow site-controlled growth. Initially basic lithographic patterning of substrates was used to control where islands would form [101, 102]. Holes or pits can be etched into the GaAs substrate prior to monolayer growth, with dimensions of the hole affecting QD shape, thus emission properties [103]. This method of growth produces a large variability in dot size, and relatively broad emission ($\sim 0.57\,\text{nm}$) [104]. Such variability and broad emission prohibits highly resonant cavity design, as highly resonant cavities have narrow band-widths; for example for a micropillar at $1.5\,\mu\text{m}$ with $Q = 165,000$, has a bandwidth of $\sim 9\,\text{pm}$ [105]. Multiple monolayer growths, separated by a buffer layer, allows QD formation on an un-etched GaAs substrate. The QDs form at locations where stresses have propagated through the buffer layers. QDs grown using this method have recently demonstrated narrow line-widths and indistinguishable single photons [106], however optical performance is still not as good as uncontrolled growth. Several growth techniques have been developed to force the formation of islands at specific locations [101, 102]; these mainly focus around etching pits into the GaAs substrate, the InAs then nucleates at these points. Such QDs are reported to have good optical properties ($g^{(2)} = 0.02$; and Indistinguishibility visibility, $V = 0.73$) [106], but are still trailing un-controlled growth and are more time-consuming and costly. Other techniques such as using atom migration in mesa-top growth have shown rather broad line-widths of $\sim 1.3\,\text{nm}$ [107].

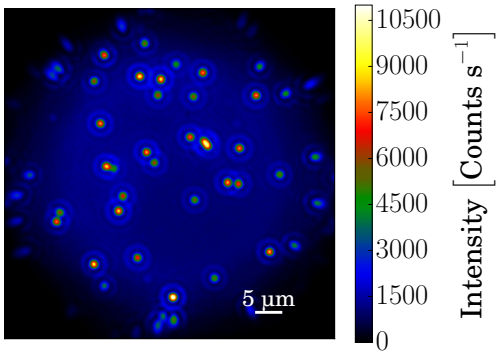

Figure 2.10: PL image of a SSQD wafer, showing the random spatial distribution of QDs.

Colloidal Quantum Dots

Colloidal quantum dots are similar to SSQDs in that they are essentially zero-dimensional objects; they occur as individual particles, instead of being embedded in a crystal lattice. These dots are fabricated in solution, with a wide array of chemistries available: CdS, CdSe, CdTe, PbS; and recently, non-heavy-metal varieties, such as InP and ZnSe [108]. Single-photon emission from colloidal dots was first observed in 2000 [109].

A well-studied variety are CdSe/ZnS colloidal dots. These quantum dots are made by a self-assembly process, where precursor reagents are mixed in a heated reaction vessel. The reaction time and temperature governs the size of the quantum dots produced [110]. A ZnS shell surrounds the CdSe core. The shell protects the core, preventing bleaching from oxygen, and leaching of the core into the suspension medium [111].

2.2 Weak Coupling Regime

The weak-coupling limit of the light-matter interaction occurs when the light losses from the system (leakage of photons from the system, γ; and decaying to non-resonant modes, κ) are greater than the emitter-system coupling, g_0 [23]. The light emission process from the photon source is irreversible, more light leaves the system than remains trapped inside. In this regime, the density of states is locally modified, allowing the emission rate of a photon source to be modified via the Purcell effect. Many different avenues to achieve this are available [112], for example: nano-photonic cavities, photonic crystals, and plasmonics.

2.2.1 Photonic Cavities

The light-matter interaction can be modified and controlled by placing the matter into a photonic cavity. An optical cavity is a structure in which light can reflect back-and-forth forming a resonance, passing through the matter many

times. A simple optical cavity is shown in Figure 2.11.

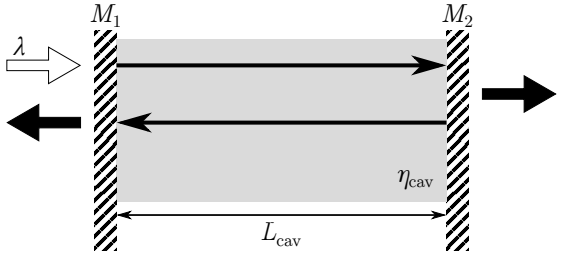

Figure 2.11: Schematic of an optical cavity, characterized by: cavity medium refractive index (η_{cav}); mirrors (M_1 and M_2) with a reflectivity R; and a cavity length of L_{cav}. The input light has a wavelength λ (white arrow). The large black arrows represent leakage of light from the cavity.

The lifetime of a photon within the cavity, τ_{cav} is defined by:

$$\tau_{\text{cav}} = \frac{\eta_{\text{cav}} L_{\text{cav}}}{c(1-R)} \tag{2.8}$$

where c is the speed of light in free space, other variables are shown schematically in Figure 2.11. The ability of a cavity to trap light is quantified by the quality-factor (Q-factor):

$$Q = \frac{\omega}{\Delta\omega} \tag{2.9}$$

where ω is the peak emission frequency (resonant frequency), and $\Delta\omega$ is its line-width.

The spontaneous emission rate from an emitter is given by Fermi's Golden Rule [22]:

$$W = \frac{2\pi}{\hbar^2}|M_{12}|^2 g(\omega) \tag{2.10}$$

where W is the spontaneous emission rate, $\hbar$ is the reduced Planck constant, M_{12} is the transition matrix element, and $g(\omega)$ is the density of states. As there is no field source within the cavity, the matrix element is given by the dipole interaction with the vacuum field:

$$M_{12} = \frac{\mu_{12}^2 \hbar \omega^3}{6\epsilon_0 V_0} \tag{2.11}$$

where μ_{12} is the electric dipole moment, ω is the emitter frequency, ϵ_0 is the permittivity of free space, and V_0 is the cavity volume.

The density of states can be altered by coupling the emitter to a resonant mode of a cavity. The density of states for an emitter in free space is given by:

$$g(\omega)_{\text{free}} = \frac{\omega^2 V_0}{\pi^2 c^3} \tag{2.12}$$

If the atom-cavity coupling is smaller than the losses from the cavity, the system is within the so-called weak coupling regime. Weak coupling allows the use of perturbation theory to calculate the density of states if the emitter is exactly

on-resonance:

$$g(\omega)_{\text{cav}} = \frac{2Q}{\pi\omega_0} \tag{2.13}$$

where ω_0 is the emission frequency.

By placing an emitter inside a cavity, the emitter can couple to the cavity modes, and the photon lifetime of the emitter can be modified. This changing of the lifetime is called the Purcell effect [113]. The Purcell factor (F_{p}) can be calculated by comparing the spontaneous emission rates of an emitter outside a cavity (W^{free}) with one coupled to a cavity (W^{cav}):

$$F_p = \frac{W^{\text{cav}}}{W^{\text{free}}} = \frac{3Q(\frac{\lambda}{\eta_{\text{cav}}})^3}{4\pi^2 V_0} = \frac{\tau_{\text{free}}}{\tau_{\text{cav}}} \tag{2.14}$$

where τ_{free} and τ_{cav} are the photon lifetimes for free and cavity-coupled emitters respectively. For $F_{\text{p}} > 1$ spontaneous emission is enhanced, and for $F_{\text{p}} < 1$ spontaneous emission is suppressed. It should be noted that $F_{\text{p}} \propto Q$, so the design and fabrication of high Q-factor cavities is key to increasing spontaneous emission rate. Increased emission rate is desirable as it makes it possible to generate more single photons from a given source per second. Furthermore, enhancement of the spontaneous emission rate reduces photon dephasing, increasing the indistinguishibility of the photos [69]. For any information based technologies which encode information with photons, increased photon input translates to increased information throughput. Many optical cavity types have been developed [114], for example: Bragg grating micropillars [115], microdisc cavities exploiting whispering gallery modes [116], and photonic crystals [117].

2.2.2 Photonic Crystals

Photonic crystals (PhCs) are a material structure that allows control over the propagation of light, they are the optical equivalent of electronic semiconductors. Whereas the atoms in the crystal lattice of a semiconductor provide a periodic electric potential, PhCs rely on the periodic modulation of refractive index. The simplest case is that of a dielectric stack: a stack of alternative layers of materials with different refractive indices. Incident light is partially reflected at each interface, with multiple reflections (assuming the alternation is periodic) destructively interfering to completely suppress the forward propagation of the light within specific wavelength regions [118]. The light that is forbidden from propagating through the material is reflected; this is the basis of dielectric mirrors. This phenomenon was first explained by Lord Rayleigh in 1887 [119].

This suppression arises due to the creation of a photonic bandgap, a region of wavelength (or frequency) space where no light propagation is supported. The critical feature of PhCs is that the bandgap can be modified by changing the properties of the dielectrics and their periodicity. This allows complete control over the optical properties of a system.

So far, only 1-dimensional (1D) structures, dielectric stacks have been mentioned. By increasing the dimensions of periodicity (as in Figure 2.12), richer band-structure features become available. An example band-structure for a 2D crystal is shown in Figure 2.13, where a bandgap exists between 646-754 nm. The wavevector refers to the k-space in which the wave propagates, with the

direction relative to the Brillouin zone (the irreducible unit cell, the repeating unit, of the periodic structure) indicated in the inset. The first demonstration of a multi-dimensional PhC was in 1991 [120], where holes were drilled into a dielectric to create a 3-dimensional (3D) PhC in the microwave regime – where the crystal dimensions are accessible to traditional machining. The first demonstration of a 2D device was in 1996 [121].

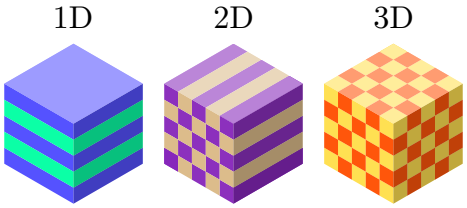

Figure 2.12: Examples of one, two and three dimensional periodic materials, with different colours representing different materials. A photonic crystal uses this periodicity to control optical properties.

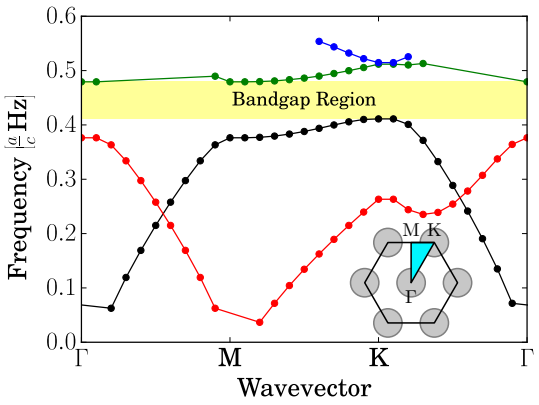

Figure 2.13: Example band-structure of a photonic crystal (a simulation of the bulk photonic crystal used in chapter 7, where a hexagonal array of holes is etched from a silicon nitride (Si_3N_4) membrane), showing allowed combinations of wavevector and frequency, the photonic bandgap region is highlighted. Only the transverse electric (TE) modes are calculated, as a dipole is unable to excite transverse magnetic (TM) modes in a 2D geometry. Frequency expressed in units of lattice constant, $a = 310\,\text{nm}$; divided by the speed of light, c. Inset: schematic showing the wavevector orientations relative to the Brillouin-zone (light blue), periodic structure shown in grey.

Whilst the most ideal structure would be a 3D PhC, allowing light propagation to be controlled exactly in all three cardinal directions, these have suffered from the fiendish difficulty in fabricating structures in 3D at the scale required for light (the sub micron regime for infra-red and shorter). Early structures leveraged existing planar fabrication technology [122]. Later approaches include bottom-up self-assembly of particles [123] and ion-drilling [124].

Let the example of a 2D PhC be considered: in this case the modulation of refractive index is achieved by drilling holes through a slab of material. This creates a periodic pattern of air (refractive index, $n = 1$) in a chosen dielectric

($n > 1$). An example of such a slab PhC is shown in Figure 2.14. Such PhCs are parametrized by three critical parameters: the centre-to-centre spacing of the holes, the lattice constant, a; the hole radius, r; and the slab thickness, T_{slab}. These three parameters are already enough to provide control to move the band-gap location and size to virtually any wavelength regime. It is fabricated as a free-standing membrane over a carrier substrate. Control of the propagation of light through the slab is controlled by the PhC; the control of out-of-plane propagation is, rather crudely, achieved by total internal reflection from the slab-air interfaces. This poorer quality (compared to that of the PhC) of out-of-plane confinement contributes to the subsequent lower performance of ideal[5] 2D devices compared to 3D equivalents.

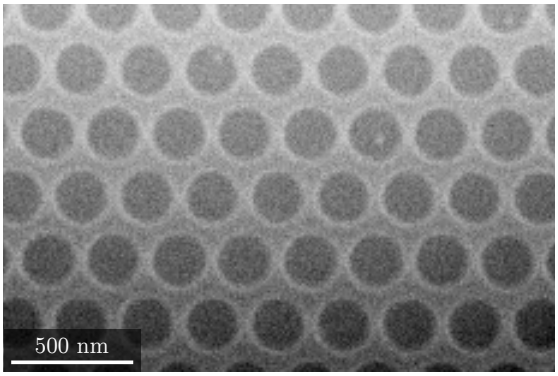

Figure 2.14: Scanning electron micrograph of a hexagonal photonic crystal slab, where air holes are etched through a Si_3N_4 membrane.

Once we have a material with a band-gap, what can we use it for? At the moment, we have defined a material which can merely block the propagation of a specific range of wavelengths. By introducing defects, a wide array of devices can be created (Figure 2.15). A defect[6] can either be the removal of a hole[7] (or several holes), or the alteration of the size or position of a hole.

By removing an entire line of holes (a line defect), a waveguide can be made (Figure 2.15a, called W1 as it is a waveguide of 1 hole width) [125]. Such a device works because the defect region, where there is no PhC, is able to support all wavelengths, but is bounded by the PhC which has a photonic band-gap. This means that any wavelengths that are within the band-gap are only able to propagate along the defect, all others are able to leak out through the PhC. In k-space this would manifest itself as a supported mode in the middle of the band-gap, meaning the waveguide itself only has a small number of supported wavelengths of propagation (which are able to propagate without leaking out). A straight waveguide is shown, but any path through the bulk PhC can be made, allowing for complete control of the light path.

A point defect is when a single hole is modified. In the example shown in Figure 2.15b, this is done by modifying the hole size [118]. In this case, the band-

[5]Considering the difficulty of fabricating perfect 3D PhCs and the relative ease of 2D fabrication, practical 2D devices remain competitive.

[6]This is a rather confusing name, as in this case it refers to intentional removal of holes in an otherwise perfect PhC, and not to defects introduced by fabrication errors.

[7]You don't technically remove the hole, you just never make the hole in the first place.

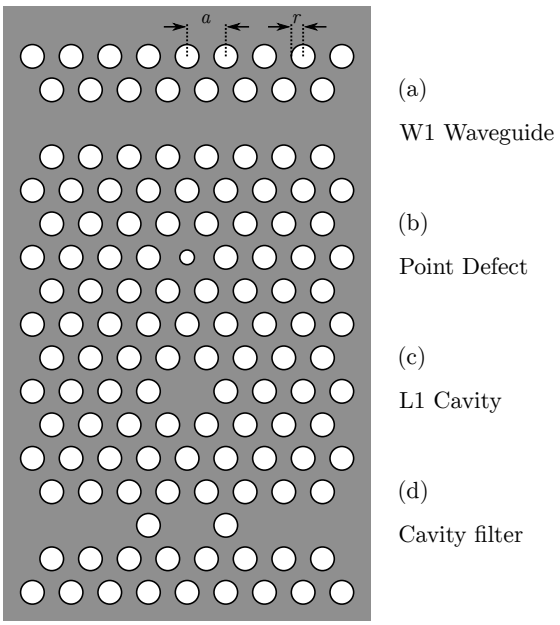

Figure 2.15: Examples of device types that can be designed by introducing defects into a 2D PhC lattice, the bulk lattice is parametrized by: the lattice constant, a; and hole radius, r.

gap becomes locally modified, creating an island within the larger crystal where some wavelengths are allowed to propagate. As their propagation is prevented through the rest of the crystal, they are trapped, reflecting from the bulk PhC on all sides: a photonic cavity. An alternative is to simply remove the hole, as in Figure 2.15c, creating an L1 cavity (so called as it is of 1 hole in length) [126]. The performance of such devices can be tuned by the modification of an almost overwhelming number of parameters: defect hole radius, displacement of hole, displacement of holes around the defect, and so on. This naturally makes the design process somewhat cumbersome, but this affords an unrivalled level of tune-ability.

Lastly, Figure 2.15d shows a cavity coupled to two waveguides. By inputting light through one waveguide and extracting it through the other, via the cavity, a filter can be made. The cavity can be designed to have a specific resonance which is then filtered out from the input light. This example shows the possibilities offered by combining the building blocks of the PhC platform, virtually anything is possible.

2.2.3 Plasmonic Devices

A plasmon is the fundamental quantum of a plasma oscillation, a rapid oscillation of electron density in a plasma or conductor; and a surface plasmon is a plasmon that is confined to a surface where it can interact with light, this results in a virtual particle: the polariton. As a photon strikes a surface, electrons gain energy and are free to migrate away, creating a small dipole. This dipole then polarizes the surrounding area, creating further dipoles. This allows

a surface plasmon wave to propagate. By introducing metal structures to the material surface, this wave can be controlled [127]. By creating sub-wavelength structures, the local electromagnetic field can be confined, providing Purcell enhancement.

Many device types have been demonstrated, exploiting the plasmonic effect to either enhance light emission, or to control emission properties: bowtie antennas [128], rod antennas [129], colloids [130], and metamaterials [131]. Plasmonics have several drawbacks: the field is tightly localized, so any emitter needs to be close, this has excluded SK QDs due to their thick capping layer ($> 50\,\mathrm{nm}$) needed for good optical quality of emission [132]; they require high-resolution nano-fabrication, typically electron beam lithography (EBL) or focussed ion beam (FIB), which can be time-consuming and expensive – bottom up techniques often provide limited configurability [133]; the metal of the devices introduces electromagnetic losses. These have limited the scope of plasmonic application, as the dream of creating plasmonic replacement for optical lenses as had to come to terms with the optical losses of such a device. However, the wide bandwidth (can be several 10s of nm) [127] means devices do not need to be exactly tuned to emitters in the way high-quality optical cavities need to be. The local field enhancement is of particular interest to sensing [134], as the relative simplicity of the devices means they can be integrated into other systems, by nanofluidics for example [135].

Chapter 3

Micro-Photoluminescence Spectroscopy

> A common mistake that people make when trying to design something completely foolproof is to underestimate the ingenuity of complete fools.
>
> Douglas Adams
> *Mostly Harmless (1992)*

MICRO-PHOTOLUMINESCENCE (PL) is a technique where the fluorescence emission from samples under excitation is examined using a microscope, allowing small features to be individually characterized. A confocal microscope allows simultaneous illumination and collection of emission from a sample under study. A camera is used to image samples, and a positioning technique can locate emitters to nm accuracy. Spot excitation using lasers allows single emitters to be spectrally characterized using a spectrometer. Emission lines can be selected and used for single photon experiments. The set-up described in this chapter was used to perform optical characterization and positioning for all work detailed in later chapters. I built the set-up and characterized the positioning technique.

3.1 Laboratory Set-up

A confocal microscopy set-up is used to examine the PL of samples, it consists of three stages (shown left-to-right in Figure 3.1). The first stage allows a sample to be imaged under light emitting diode (LED) illumination for imaging. Selected emitters can be selectively excited using lasers. A spectrometer allows the sample PL to be characterized; and, acting as a monochromator, it can select single emission lines to be selected. Photons from these emission lines can be passed to photon counting experiments where either time-resolved measurements or single-photon purity can be measured. The following discussion of

operation refers to the characterization of InAs/GaAs solid state quantum dots (SSQDs) (as described in section 2.1.4).

A quantum dot (QD) sample (a QD substrate with a metallic grid, shown schematically in section 4.2) is mounted into a liquid helium (LHe) flow cryostat, allowing samples to be cooled down to 3.2 K for optical characterization. The cryostat is mounted on translation stage, to allow the image-able area to be changed, and to move a feature of interest under the focus of a laser. An objective is used in the confocal geometry to provide sample illumination and emission collection, with separation of these light paths performed by a beam-splitter. The sample PL signal is sent for characterization from the 90% port, to minimize the number of PL photons lost.

Several different light sources are used to examine the samples. LEDs are used to provide wide area illumination ($\sim$ 80 µm diameter). A 455 nm LED is used to provide above-band excitation to the QDs, which emit photons in the region 900-100 µm. The beam-path for this source has the lowest attenuation and the least number of optical elements, so that the maximum excitation power can be provided over the full imaging area of the objective. A 940 nm LED is used to image the sample topology only, as it is unable to provide excitation to the QDs as it is below the bandgap energy. Simultaneous illumination with both light sources allows simultaneous imaging of the QD PL and the reflection from alignment markers on the chip surface (described in section 3.2).

Lasers are used to address specific QDs. Low densities of QDs are required so that only one falls within the laser spot (full-width half-maximum (FWHM) $\sim$ 2.5 µm). By using the wide-area LED illumination, a QD can be selected and moved under the focus of the laser. Laser power can be controlled using neutral density filters (NDFs) and measured using a photodetector. A 785 nm continuous wave (CW) is used for power resolved measurements, with a 785 nm picosecond-pulsed (ps-pulsed) laser being used for time-resolved photon counting. Both of these lasers provide above-band excitation to the QDs.

An electron-multiplying CCD (EMCCD) camera with an adjustable zoom lens is used to image PL signals from the sample. A longpass filter (LPF) is used to remove excitation light but pass the QD emission and sample reflection: allowing images of alignment markers with the QD PL. A 900 nm filter is used here to remove emission from the InAs wetting layer which is uniformly present across the sample, and peaks at $\sim$ 860 nm. The EMCCD has an adjustable electronic gain, to allow weak signals from single photon sources to be amplified.

PL from a selected feature can be spectrally characterized by directing the PL signal into a reflecting grating spectrometer. Spectrograms are taken using a charge coupled device (CCD) camera attached to the spectrometer, which images the diffraction pattern from the grating and provides a computer read-out. The spectrometer also acts as a monochromator, allowing a single emission line to be selected using a slit and coupled to photon counting experiments to assess purity and lifetime (discussed in section 3.3 and section 3.4).

For emitters that emit in the visible, different light sources need to be used to provide excitation. 473 nm and 405 nm CW lasers are able to provide excitation to a range of emitters: CdSe colloidal QDs, diamond nitrogen-vacancy (NV) centres, and silicon nitride (Si_3N_4). These sources emit PL in the 550-850 nm range. For imaging and spectroscopy LPFs at 550 nm are used to remove excitation light.

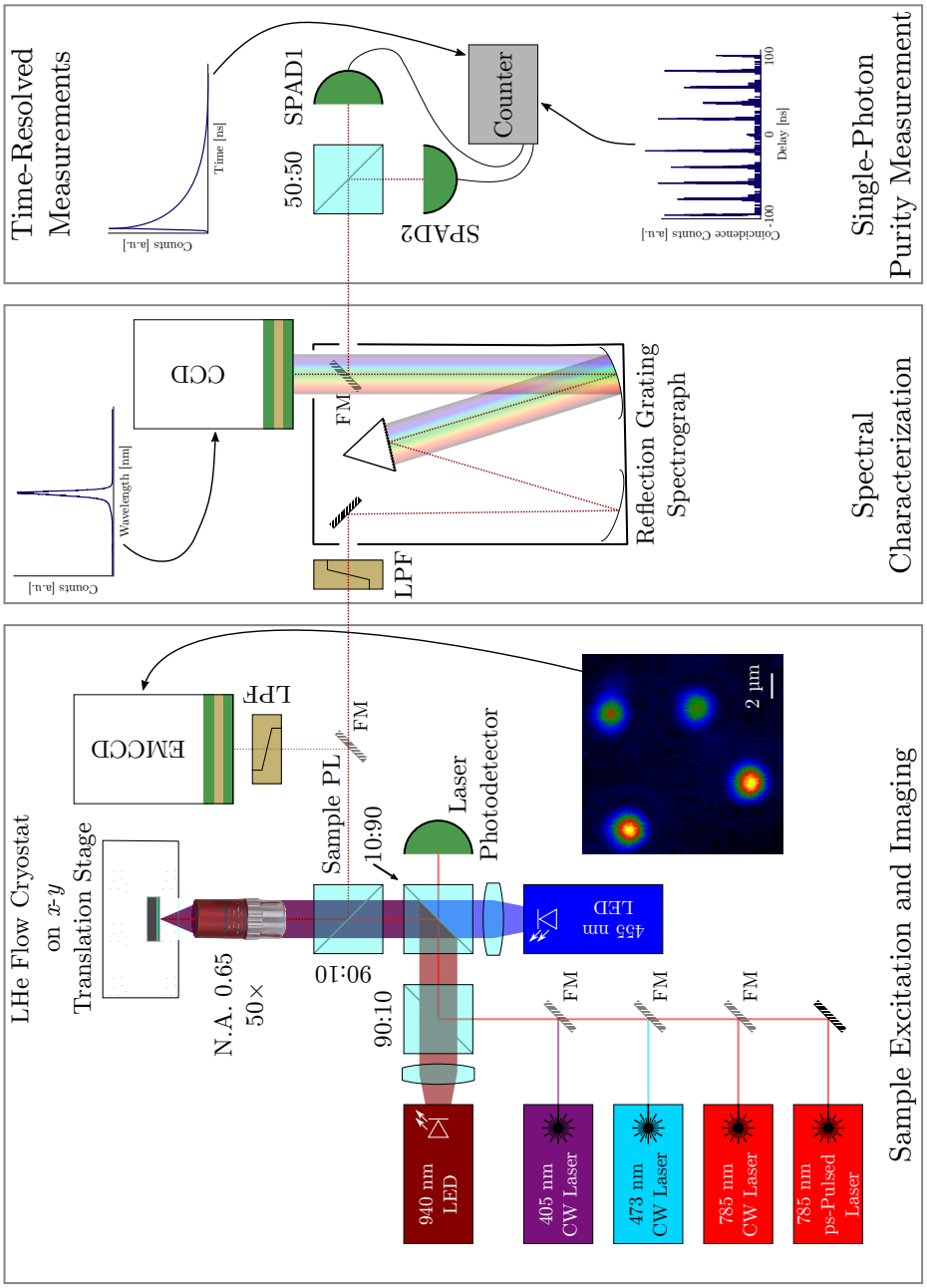

Figure 3.1: Schematic of the micro-photoluminescence set-up. This is composed of: a confocal microscope and light sources (left) to illuminate and image the sample; a spectrometer (centre) to spectrally analyse the sample emission and to perform spectral filtering; and a pair of single photon avalanche photo-diodes (SPADs) (right) in a Hanbury-Brown and Twiss (HBT) configuration to characterize single photon purity and to perform lifetime measurements. Flip-mirrors (FMs) are used to direct light between parts of the set-up.

3.2 Positioning Technique

Determining the location of emitters (SSQDs, carbon nanotubes, NV centres) and the location of modes within a device is of fundamental importance; as once the location is known, photonic devices can be fabricated around these emitters. In the case of QDs grown using Stranski-Krastanov (SK) self-assembly, the emission properties of the QDs are not precisely controlled. This leads to variation in emission wavelength, polarization and location between emitters. This positioning technique allows characterization of all of these parameters and design photonic devices tailored to the; additionally, the Purcell factor can be measured from the same emitter before and after device fabrication. Initial approaches were to use relatively high densities of QDs, and arrays of cavity devices, hoping to find an emitter/device pair that were resonant by chance [136]. In order to use devices which tightly confine the electric field, a technique is needed to locate and characterize such emitters before device fabrication. Previous examples have included: atomic force microscope (AFM) [137], confocal microscopy using scanning lasers [138] (including *in situ* lithography at cryogenic temperatures [139]), PL imaging [140] and cathodoluminescence [141]. Of these techniques, PL imaging is particularly attractive as it allows high positional accuracy (sub-50 nm) with high throughput, and the PL signal can be used to spectrally characterize emitters and photon counting and lifetime measurements can be made. It is also compatible with high resolution electron beam lithography (EBL), which can be used to pattern a range of devices: photonic crystals, bullseye gratings and nanowires.

Firstly the sample must be prepared: metallic alignment markers are deposited onto the sample surface. The markers chosen were crosses, with arm lengths of 15 µm, and widths of 1 µm, an example is shown in Figure 3.2. These were fabricated using EBL (chosen to ensure smooth edges of the markers, therefore high accuracy in position measurement, and to provide the best accuracy in position of the markers), thermal metal evaporation and chemical lift-off (procedure described in section 4.3).

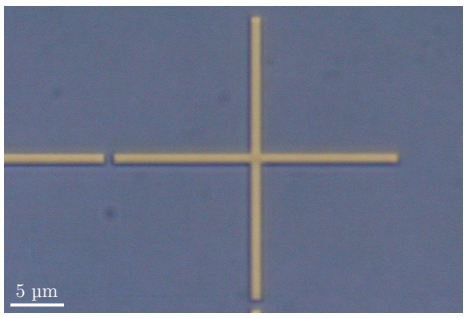

Figure 3.2: Optical micrograph of a cross metallized in Au, shown after lift-off.

When the SSQD samples are illuminated under 455 nm LED excitation, the QDs emit light, this can be imaged to show the distribution and density of the QDs, as shown in Figure 3.3a. By also illuminating the sample with 940 nm LED light, the grid also becomes visible: the grid reflection image is simultaneously imaged with the PL from the QDs, Figure 3.3b. From these images, the position of the emitters relative to the metallic crosses can be determined.

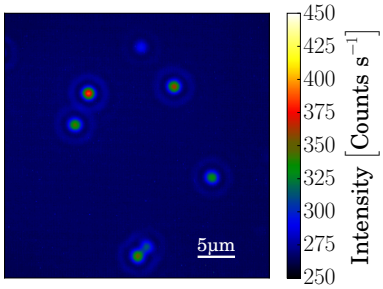

(a)

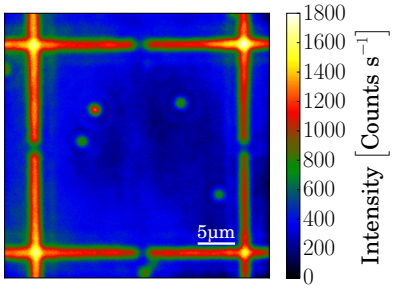

(b)

Figure 3.3: (a) PL image showing the emission from the SSQDs, sample under 455 nm LED excitation only. 2 s integration, 180 acquisitions, no gain, 9.2 K. (b) PL image of InAs/GaAs SSQDs under 455 nm LED excitation, with grid imaged using 940 nm LED illumination. Imaging parameters: 1 s integration, 360 acquisitions, ×50 gain, $T = 8.5$ K.

The first step of the image analysis procedure is to correct for any rotational offset, this offset is unavoidable as the sample cannot be mounted in the cryostat with sufficient accuracy by hand. Using the corrected image, the cross centres are marked in the software so that the extent of the grid square in known, then the individual QD are marked. This produces a map as shown in Figure 3.4a[1]. Line-cuts are then made vertically and horizontally for every QDs to establish the position of the QDs relative to the crosses. The line-cuts are fitted using a Gaussian function, as shown in Figure 3.4b. The accuracy of the fit is determined by the standard error of the positions from fits of the QD peak centre and the two cross arms either side of the QD. The example shown in Figure 3.4b has a centre at pixel 646.562(±0.125), this corresponds to an error of 10.5 nm. By fitting the cross marker either side of the QD, on the same line-cut, the distances between the QD and the grid can be measured – providing the location.

To determine the imaging parameters which corresponded to the lowest error in measured position, several images were taken with a range of acquisition settings. The settings adjusted were: the integration time; and number of images taken (accumulations), which were summed together to provide a image with higher dynamic range than a single image. Table 3.1 shows the typical errors: small numbers of accumulations severely impact the accuracy, due to a poor signal-to-noise ratio in the images. As total imaging time is increased (integration time multiplied by accumulations) the error decreases. The increased error when using 0.5 s with 240 accumulations (120 total) instead of 2.0 s with 60 accumulations can be attributed to the increased rate at which the sensor has to move image data from the sensing area. Due to the lack of a mechanical shutter, light can still interact with the sensor, so the image data can be altered during this read-out phase. By decreasing the number of times this can happen, the number of artefacts in the images are reduced, leading to lower errors. The

[1]Whilst this may give the appearance of a fully automated process, the feature selection and setting of the fitting range is manual. This minimizes incorrect fits and poor feature selection, but with tuning could be automated for a production system [142].

result of these tests are that the minimum error in the location of QD in a grid of crosses is ~ 21 nm.

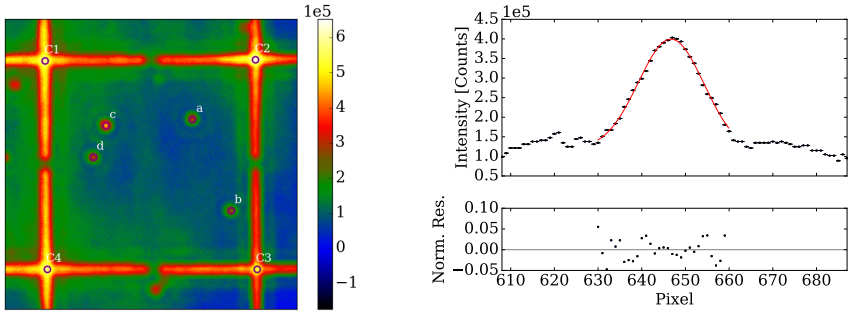

(a) (b)

Figure 3.4: (a) Map of features generated during position analysis process: cross centres and emitters marked. Colour bar indicates intensity in counts. (b) Line-cut of cross arm to the right of feature a. Upper panel: line-cut data (symbols) and Gaussian fit (red line). Lower panel: normalized error residual plot, used for verification of fit quality.

Int. Time [s]	Accumulations	Error [nm]
0.5	120	28
0.5	240	26
1.0	1	86
1.0	60	22
1.0	120	22
1.0	180	20
2.0	1	71
2.0	60	21

Table 3.1: Comparison of image acquisition conditions, with the combined error in the position of the alignment grid and quantum dot in nm.

3.3 Lifetimes

Time resolved measurements, such as exciton lifetime, can be made using a synchronized pulsed light source, the 785 nm ps-pulsed laser. This laser produces a stream of short light pulses, as shown in Figure 3.5, which are used to excite emitters. The laser is focussed onto a QD and the emission is collected. This is filtered by the spectrometer and passed to a single SPAD (the 50:50 beamsplitter of the HBT is removed, increasing photon flux on the single detector), shown in Figure 3.6. The SPAD sends an electronic pulse upon detection to the counter for each photon.

The counter records the time the laser fired the excitation pulse and also the arrival time of the emission photon. From this information, the time difference

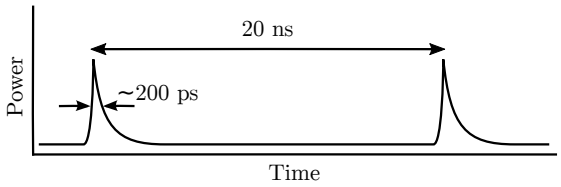

Figure 3.5: Approximate pulse shape and timings for the 785 nm ps-pulsed laser.

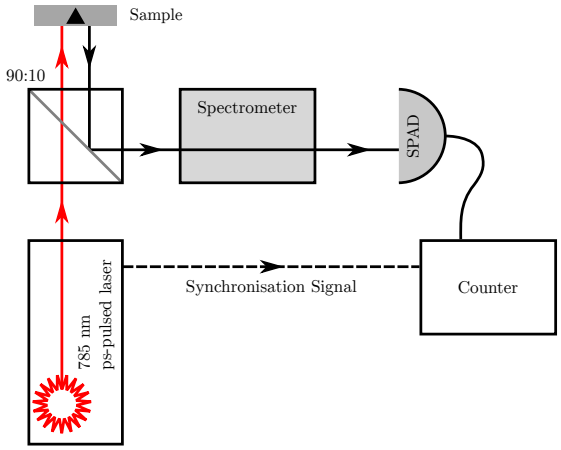

Figure 3.6: Reduced schematic showing how lifetime measurements are made. The laser produces a pulsed beam of light (red line) at 785nm, which excites the sample producing emission (solid black). The counter then records the laser shot times and detection times.

between the laser shot and photon detection can be determined for each detected photon. This calculation step can be performed in post processing, which is slow and generates large quantities of uncompressed data (10s of GB); or through the use of a dedicated field-programmable gate array (FPGA) circuit in the counter which returns a histogram of times. The FPGA based approach was not used for initial calibration measurements but used for all subsequent measurements. To verify the functioning of the detector and counter, the lifetime of a QD in a bullseye grating [27] was taken; shown in Figure 3.7. The e^{-1} lifetime is $1.07(\pm 0.04)$ ns.

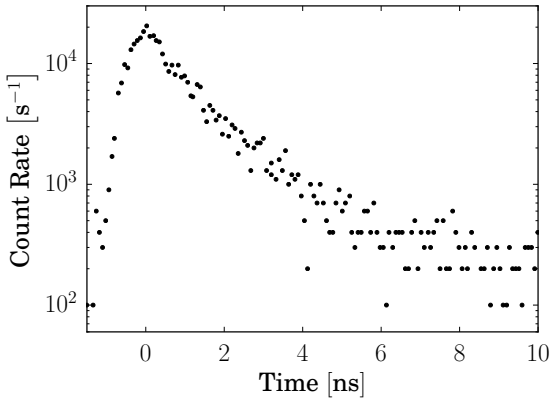

Figure 3.7: Lifetime measurement from a bullseye grating device.

3.4 $g^{(2)}$ Measurement

Single photon purity is characterized using a HBT experiment, where $g^{(2)}(\tau)$ is measured, as described in section 2.1.2. The time-tagged list of detection events is split into two lists: one for each detector. These lists are then examined to identify any coincidences between them – simultaneous detection events. To create a sweepable time-delay, the times in one of the lists are advanced by a time increment, creating a temporal offset. This process is repeated for a range of offsets, fully recovering the autocorrelation behaviour desired. Figure 3.8 shows the auto-correlation plot for the ps-pulsed laser. There is no missing peak at $\Delta\tau = 0\,\mathrm{s}$, indicating $g^{(2)}(0) > 0$, as expected for a bunched light source, such as the laser examined.

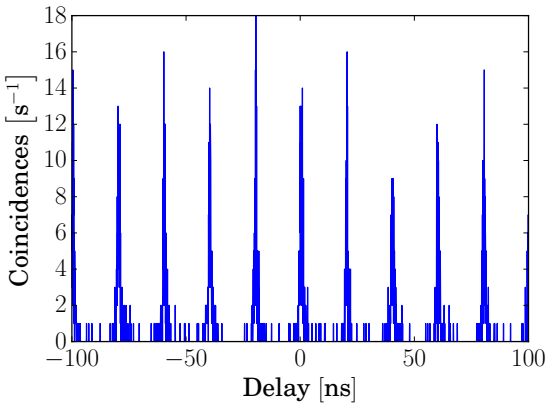

Figure 3.8: Photon auto-correlation plot using the 785 nm ps-pulsed laser as a light source. The lack of a missing peak at $\Delta\tau = 0$ proves that the light is bunched.

Chapter 4

Metallic Nanorings

> ...can one desire too much of a good thing?
>
> William Shakespeare
> *As You Like It (circa 1600)*

OLID-state quantum dots (SSQDs) have desirable optical properties: pure single-photon emission [143] and highly indistinguishable [144] single photons. They also have the advantages of a solid-state platform: stability, simple integration with electronic devices, and can leverage existing fabrication technologies. However high refractive index contrast, between the substrate and air, hampers free-space collection of emitted photons. A number of devices to improve out-coupled light have been developed: micropillars [145]; nanowires [146]; bullseye ratings [147] and solid immersion lenses [27]. However, these devices suffer from issues such as narrow bandwidth, difficulty of fabrication or fragility. Here a metallic nanoring is used to enhance emission for collection by free-space optics, and a hybrid nanoring and super-solid immersion lens (SIL) device is demonstrated. The quantum dot wafers were grown by Jin Dong Song and Suk In Park, and the super-SIL deposition was performed by Christopher Woodhead. Initial investigations and simulations were performed by Tom Frank, Barnaby Sleat and Jason Tam. I performed simulations to design the devices, prepared the sample for characterization, fabricated the devices, characterized the device performance and performed all analysis. The work in this chapter was published as [148, 149].

4.1 Enhancing the Emission from Solid State Quantum Dots

The extraction of light to free space is a key challenge that needs to be tackled when using solid-state emitters in a high refractive index material. At the interface between the material and the air, total internal reflection can trap most of the light; preventing efficient extraction, with extraction efficiencies as low as a few percent. This issue needs to be overcome for the development of high brightness light emitting diodes (LEDs) [150], lasers [151] that are based on

quantum wells or quantum dots. Increasing extraction efficiency is of particular interest for intrinsically dim light sources, such as single photon emitters, necessary for fundamental science [152, 153] and quantum technology applications [154].

Solid state quantum dots (SSQDs) are of particular interest as they are grown onto semiconductor chips directly (allowing easy integration within integrated optical circuits), they can exhibit lifetime-limited emission line-widths [155], and emit indistinguishable and pure single photons [143]. However, the high refractive index contrast between the bulk GaAs substrate and air can lead to less than 1% of light escaping to free space. Several different approaches to increase extraction efficiency have been followed: micropillars, based on distributed Bragg reflector (DBR) stacks; light-guiding nanowires; circular gratings on suspended membranes; SILs, which are discussed in detail in section 4.7.

Micropillars are cylindrical structures typically a few microns in diameter, which are etched from a substrate [143, 156]. During the growth process, DBR stacks are grown above and below the quantum dot (QD) layer and form reflectors at either end of the pillar. The top DBR stack has fewer layers, lowering the reflectivity, allowing light to be out-coupled into free space. Small mode volumes of the order of a few λ^3 are achievable [157], tightly confining the light. They are highly directional, allow high QD brightness and provide Purcell enhancement via interaction with the cavity mode. Q factors as high as 268,000 have been reported [156]. Consequently, these devices have a low bandwidth, the narrow cavity mode must be perfectly on resonance otherwise it has greatly reduced effect: the device can be tailored to the QD by making use of pre-fabrication characterization and the QD can be temperature tuned to the cavity resonance [139]. Micropillar samples require DBR growth, which is complex and time consuming. They also bring etched surfaces in close proximity to the QD, which can degrade optical performance [132, 158].

Nanowires are light-guiding structures that act to direct light from the emitter vertically. There are several geometries for this: the simplest is a needle-like structure etched from the sample [159]; more complex funnel-shaped trumpet devices can also shape the out-coupled optical mode to match collection optics [160]. These devices are single material (except for the QD); they usually do not have reflectors, therefore half of the emitted light is typically lost into the substrate. Unlike with micropillars, there is no micro-cavity, dispensing with the need to perfectly match resonances: thus these devices have a wide bandwidth. The main disadvantage of these devices is their fragility: the high aspect ratio makes them vulnerable to mechanical stresses, seriously affecting their scalability. They also bring etched surfaces close to the QD, which degrades the optical quality of the emitted light [132].

Circular 'bulls-eye' gratings are structures etched around an emitter in a membrane [147, 161, 27]. These devices are a set of concentric rings asymmetrically etched into a GaAs membrane, centred around a single QD. These provide high theoretical collection efficiencies of 80%, and modest Purcell enhancements of up to $\times 11$; experimentally, collection efficiencies up to $48.5(\pm 5.0)\%$ with Purcell factors of $\approx \times 4$ are seen. These devices have a moderate bandwidth, $\sim 5\,\text{nm}$. The asymmetric etch is nanometre-sensitive, requiring a highly calibrated etching process, therein lies the problem: the devices are sensitive to single nanometre variations in etch depth, limiting scalability.

To overcome the limits of fragility, scalability and bandwidth a new device

was examined: the nanoring [148][1]. This is a ring of metal deposited on the surface of a sample, centred around the QD beneath the surface. As will be shown, these nanorings provide a lensing effect and have no cavity to tune to resonance.

4.2 Simulations of Nanoring Devices

The nanorings were designed with finite-difference time-domain (FDTD) simulations, using a commercial software package [162]. A computer model of the QD sample structure was made, as shown in the schematic (Figure 4.1). From the bottom: the substrate was GaAs; a 1 µm $Al_{0.7}Ga_{0.3}As$ layer (this was included to permit undercut of devices at a later time); 95 nm GaAs; InAs wetting layer (purple dotted line), with QDs; 95 mn GaAs capping layer, in the schematic this capping layer is shown to have a thickness T_{cap}. The ring was made up of a 7 nm Cr adhesion layer [163], and a variable thickness Au top. The ring was characterized by three key parameters: T_{Au}, the hight of the gold layer; r_{inner}, the inner radius of the hole in the ring; and r_{outer}, the outer radius of the ring. The QD was modelled using a dipole source with a Gaussian emission spectrum centred at 910 nm, placed 95 nm below the surface of the sample.

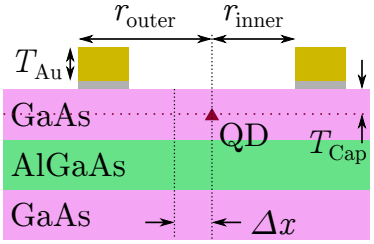

Figure 4.1: Schematic of a metallic nanoring and the QD substrate, with critical simulation parameters shown: capping thickness, T_{cap}; thickness of ring Au layer, T_{Au}; ring inner radius, r_{inner}; ring outer radius, r_{outer}; displacement of ring to QD, Δx.

Initial parameter sweeps were run to establish coarse upper limits for the device design, with the lower limits being dictated by fabrication resolution. A particle swarm optimization routine [164] was then used to tune the device dimensions, to maximize the electric field incident on a 1 µm^2 surface, 2.5 µm above the sample. The optimal dimensions were: $T_{\text{Au}} = 60$ nm, $r_{\text{inner}} = 220$ nm, and $r_{\text{outer}} = 540$ nm.

In the simulations, the electric field intensity ($|E^2|$) is calculated for an emitter in bulk (Figure 4.2a[2]); and measured on a plane parallel to the sample surface (Figure 4.2a). A line-cut across this surface (as indicated by the dotted line in Figure 4.2b) is shown in Figure 4.2c, fitted with a Gaussian function. The full-width half-maximum (FWHM) of the far-field profile in bulk is 3.9 µm. Identical simulations were performed using a ring with the optimal parameters,

[1] I prefer the catchier name of 'Pineapple Rings' as suggested by a colleague at a workshop, based off of false-colour scanning electron microscope (SEM) images, where the rings were coloured gold.

[2] When viewed digitally, due to rendering artefacts, the FDTD mesh can be discerned.

as shown in Figure 4.2. The electric field can be seen to be focussed by the ring: the far-field emission is brighter and the line-cut Gaussian FWHM is reduced to 2.5 µm. A comparison of the integrated $|E^2|$ over the far-field surfaces shows that the ring enhances the emission by ×7.2. It can also be seen that a significant amount of light is lost into the substrate with and without the nanoring; this could be addressed by including a back reflector to re-direct light upwards. Simulations were run to calculate the field loss caused by the metallic nanoring: the simulated volume was surrounded by monitor surfaces and the electric field integrated over all surfaces in the case with and without a metallic nanoring. The plasmonic losses were found to be negligible.

Additional simulations were undertaken to investigate the performance of

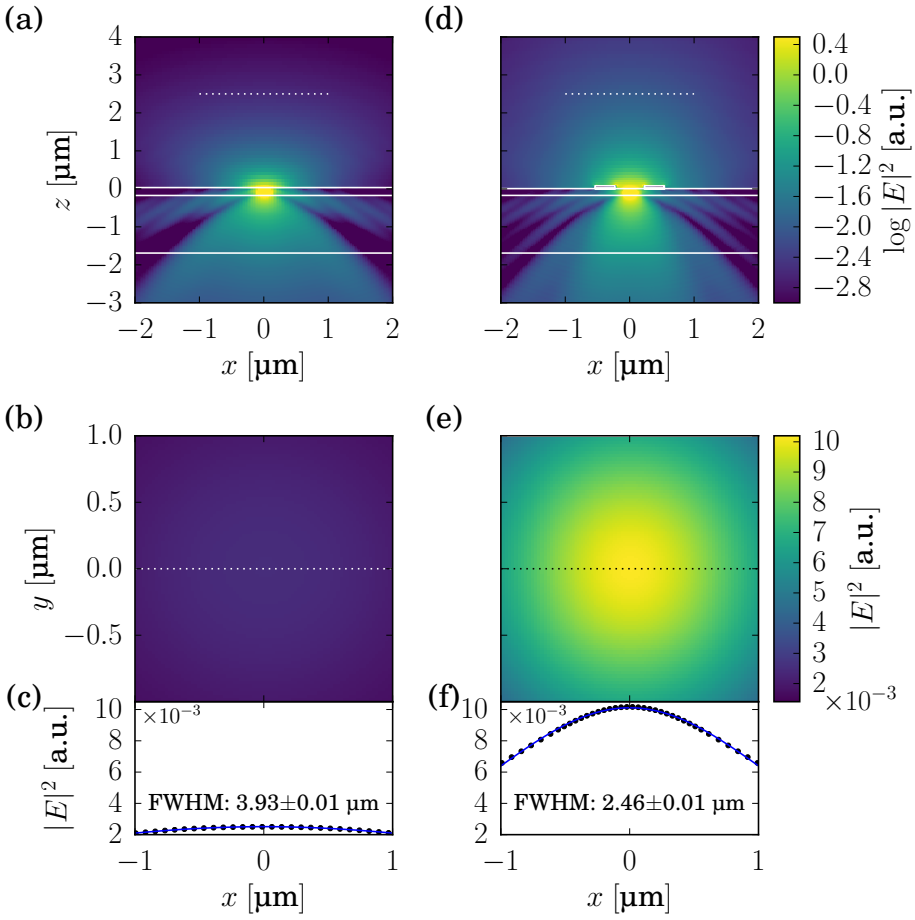

Figure 4.2: (a) FDTD simulation of the electric field from a dipole emitter, 95 nm below the surface – representing the emission from a QD in bulk. The solid white lines indicate the material structure as shown in Figure 4.1. (b) Plot of the electric field at a distance of 2.5 µm from the surface of the substrate, indicated by the dashed line in (a). (c) Line-cut across the far-field profile (symbols) indicated by the dotted line in (b), a Gaussian fit is shown in blue with the FWHM indicated. (d)-(f) As (a)-(c) but with a metallic nanoring placed on the substrate surface centred around the dipole source. The ring is indicated by additional white lines in (d).

the ring if it were off-centre and if the capping thickness were adjusted, Figure 4.3. To simulate displacement, the ring was moved relative to the emitter position (this kept the field monitors static), shown by the displacement Δx in Figure 4.1. The results indicate that a displacement of 50 nm would lead to a drop in performance to $\sim \times 6$; fabricating the device to within 50 nm is well within the accuracy provided by the positing technique in section 3.2. The emission drops off to zero at ∼300 nm, where the emitter becomes masked by the ring itself. The variation of capping layer thickness, T_{cap} (as in Figure 4.1), does not appear to have much effect on device performance (for fixed ring dimensions) as shown in Figure 4.3; this is of particular interest, as emitters simply placed on the surface instead of being sub-surface could also benefit from enhancement from the nanoring. However the devices were not optimized for this, so higher enhancements may be possible with refinement of the device dimensions.

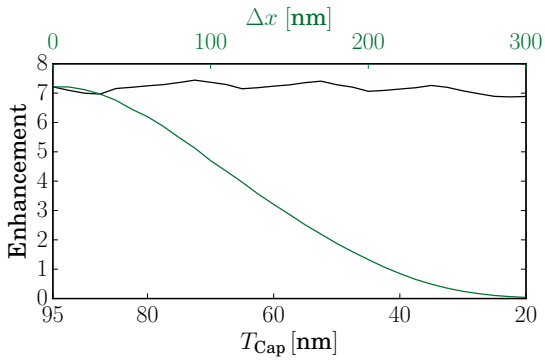

Figure 4.3: Simulation of the dependence of the emission enhancement factor as a function of: dipole position relative to the ring centre (Δx, green); and dipole distance to the sample surface (T_{cap}, black) with the QD centred to the ring.

4.3 Fabrication of Nanorings

Nanorings were fabricated around emitters identified and located using the positioning scheme, and using conventional complementary metal oxide semiconductor (CMOS) processes: patterning using electron beam lithography (EBL), thermal evaporation and chemical lift-off, recipes described in section A.1.

EBL is a type of mask-less lithography, where no physical mask exists to block exposing radiation, the exposure is guided by an computerized electronic mask. EBL uses a highly focussed beam of electrons which are directed onto the sample to be exposed, which has been coated in a thin layer (∼400 nm thick) of polymer which is electron sensitive (Figure 4.4a), in the case of the nanorings, the high-resolution resist poly(methyl methacrylate) (PMMA) was used [165]. A dual resist structure was used for the patterning of the alignment crosses, but not for the nanorings, due to the small size of the ring centre – a dual scheme would have undercut the central resist island. The exposed resist is then developed in a manner analogous to film photography. In order to write the nanorings with sufficient accuracy, alignment is required. Local 'chip-marks' were specified, the four crosses that formed a bounding box around the QD. Each

arm of each cross was scanned to determine the exact position of the mark, the scan marks are visible around the cross in Figure 4.4b, using these positions the pattern can be written to sub 4 nm accuracy.

To reproduce the nanoring in metal, a thin metal film is deposited over the entire sample using thermal evaporation, Figure 4.4c. In this process the coating metal is heated in a holder made from molybdenum (Mo), chosen due to the high melting point of 2622°C [166]. Metal coats all surfaces with line-of-sight to the metal source, metal makes contact with the sample in areas where the resist has been removed, adhering to the surface. Deposition thickness is monitored and the process halted when the desired thickness is reached.

The excess metal film is removed using lift-off (Figure 4.4e), where the resist layer is dissolved in a solvent; taking away any non-adhering metal. Slight agitation is used to aid the process for small features. This leaves the finished nanoring, rendered in Cr and Au, Figure 4.5. Figure 4.6 shows several nanorings on a sample and the alignment crosses.

4.4 Characterization of Nanorings

Self-assembled QDs grown with a distribution of wavelengths, and random spatial positions. Therefore, prior to fabrication of nanoring, several measurements need to be taken: photoluminescence (PL) images to determine the position of the QDs and spectral measurements to characterize the emission of the QDs in bulk. Figure 4.7 shows a typical PL image, with the grid and QD PL visible, from which positions are determined (section 3.2). Power-resolved spectral measurements are taken, these determine the initial brightness of the QD in bulk and its saturation behaviour. A typical bulk spectrum is shown as the green line in Figure 4.8. After the fabrication of the nanorings around selected QDs, the spectral measurements are repeated, so the change in brightness of the emitters can be measured.

The change in brightness of emission lines from QDs is done using the intensity of emission lines in spectrograms. This is highly sensitive to the in-coupling of light to the spectrometer: an enhancement could erroneously result from a better coupling when making measurements with the nanoring than when making those in bulk. To eliminate this, the quality of the spectrometer coupling was measured: several QDs were selected near fabrication sites which would act as calibration sources. No nanorings would be written around these QDs, so their bulk emission should remain constant, allowing the coupling to the spectrometer to be determined on a day-to-day basis. Any difference in count rate was attributed to variation in coupling and measurements were scaled accordingly. These adjustments were up to a maximum of $\sim 30\%$.

4.5 Results

Example of power resolved spectra (a power series) are shown in Figure 4.9. For these measurements, the excitation power of the laser was varied, and spectra taken at each laser power; this shows the emission properties as a function of pump power density. The left panel shows a zoom-in of an emission line shown in Figure 4.8, before and after ring deposition, with Lorentzian fits. The right

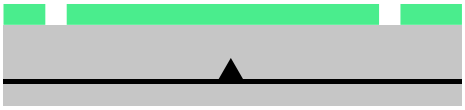

(a) Developed EBL of nanorings. The resist layer is shown in green, the missing areas are where the resist has been removed during developing.

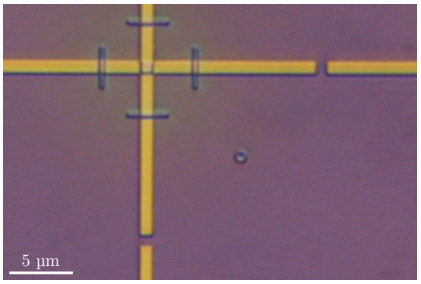

(b) Optical image showing developed resist after write. The mask pattern is visible as areas where the resist layer has been removed.

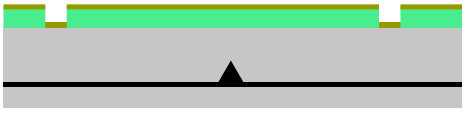

(c) Metal layer (gold) deposited over entire sample using evaporation.

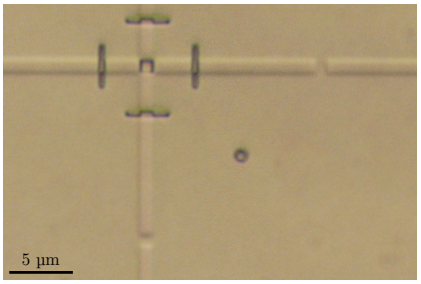

(d) Optical image of sample after gold evaporation.

(e) Removal of resist and metal layer, leaving finished device.

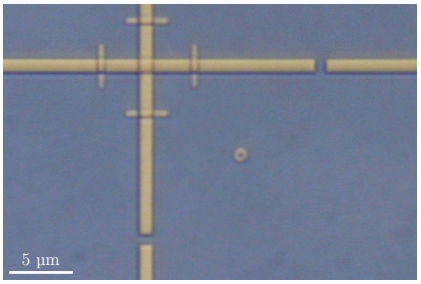

(f) Optical image of metallized ring and crosses.

Figure 4.4: Fabrication process for metallized nanorings onto a sample substrate: (a) patterning of rings into resist using EBL, shown once developed; (c) ring metallized in Au; (e) chemical lift-off removes excess metal, leaving a ring. (b), (d), (f) micrographs of a sample for each of the process in (a), (c), (e). Optical micrographs shown in real colour.

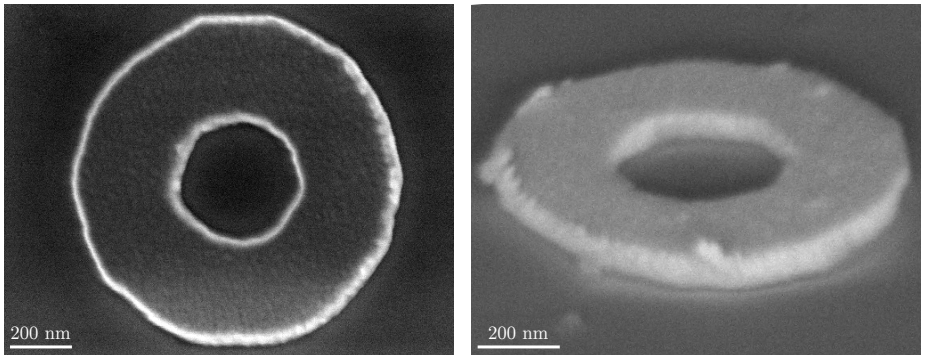

(a) (b)

Figure 4.5: (a) Scanning electron micrograph of a Au nanoring on a GaAs substrate. (b) Micrograph with 35°tilt.

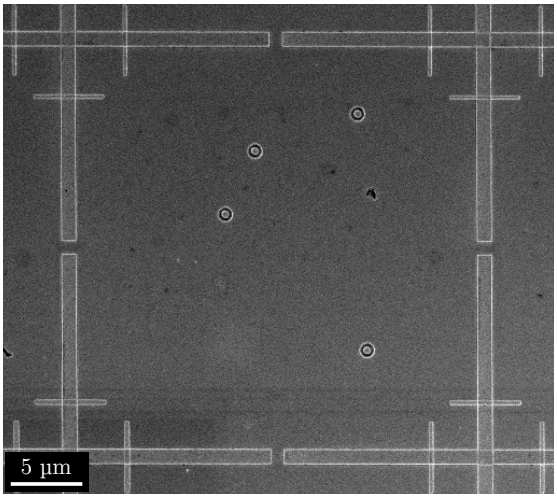

Figure 4.6: Scanning electron micrograph of metallized nanorings. Scanning marks from the EBL aligning process are visible around the cross centres.

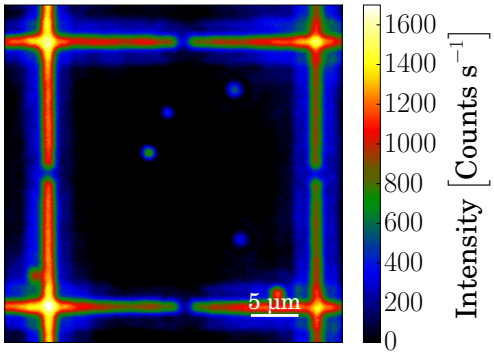

Figure 4.7: PL image of SSQDs in bulk under 455 nm LED excitation and 940 nm LED illumination to image the grid. Image parameters: 1 s integration, 360 acquisitions, $\times 50$ gain, $T = 8.3$ K.

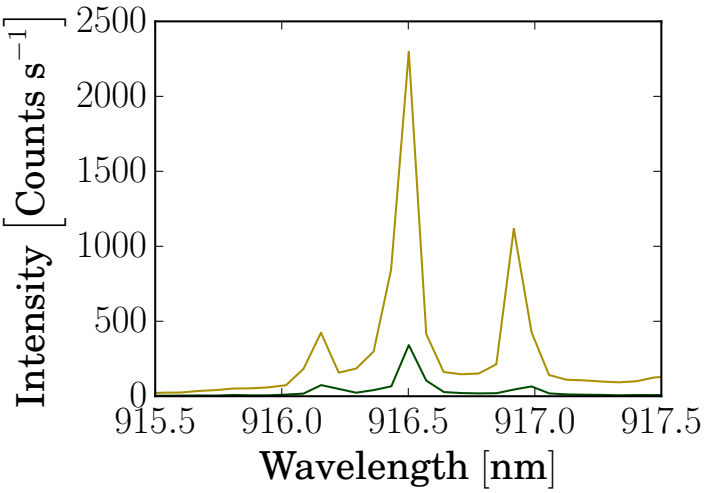

Figure 4.8: PL spectra from a SSQD at saturation under 785 nm continuous wave (CW) laser excitation, shown in bulk (green) and with ring (yellow).

panel shows the peak value of Lorentzian fits of spectra for each power density. The dashed lines are fits using the equation [167]:

$$I(P) = I_{\max}\left(1 - e^{-\frac{P}{P_{\text{sat}}}}\right) \tag{4.1}$$

where I is the intensity at pump power P, $I_{\max}$ is the maximum emission intensity and P_{sat} is the power at saturation. This shows that we can achieve an emission enhancement at saturation of $\sim \times 25$. It should be noted that this equation applies under pulsed excitation, whereas the measurements were made using CW excitation. When CW is used the intensity does not saturate, but reaches a peak and decreases as excitation is increased further. Under pulsed excitation the emission saturates as excitation power is increased. This is caused by the QD being unable to fully relax after excitation, so other recombination pathways begin to dominate at higher excitation energies.

These nanorings have no cavity mode, and do not provide Purcell enhancement to the QDs, instead act as a lens focussing the emission. Consequently, their bandwidth is greater than a micro-cavity based device: $\gtrsim 4\,\text{pm}$ for a micropillar [156] or $\sim 5\,\text{nm}$ for a bullseye device [27]. Experimentally, the same nanoring design was used for emitters from 900-960 nm without modification, and multiple emission lines were enhanced. As can be seen by the spectrum in Figure 4.8, multiple emission lines are enhanced by varying amounts. This is believed to be caused by modification of the focussing of the excitation laser spot by the nanoring (changing local power density), which in turn can excite different charged states differently [168, 169]. By using the nanoring as an electrical contact, an electric field can be applied over the QD to charge-tune the QD [155]. This could allow the behaviour of how charged states interact with the nanoring to be fully understood.

By examining the enhancement of multiple devices, statistics of performance can be obtained. Figure 4.10 shows that 78% (29) devices provided emission enhancement, with 19% (7) providing over $\times 10$. The variation in enhancement factor could be attributed to errors in device placement, non-central positioning of the ring around the QD location.

4.6 Conclusions

The nanorings have been demonstrated to provide enhancements up to $\sim \times 25$ of single emission lines, with a yield of 78% of successful devices. They utilise a lensing effect which is intrinsically broadband, and do not rely on any cavity. Therefore, metallic nanorings are compatible with a wide range of emitter/substrate combinations, such as: NV centres, molecules, carbon nanotubes and colloidal quantum dots.

The nanorings are relatively easy to fabricate, involving only a single lithographic step and have feature sizes within the reach of optical and nano-imprint lithography [170]. The metal ring can also be used as an enhancement-providing electrical contact for: charge-tunable devices [155] (which typically suffer be incompatibility with other light-enhancing devices, and have to resort to using SILs); Stark-effect wavelength tuning [171]; charge-noise reduction using electric fields [143]; and potentially electrical carrier injection [172]. The nanorings can also be hybridized with other devices to combine enhancements, such as:

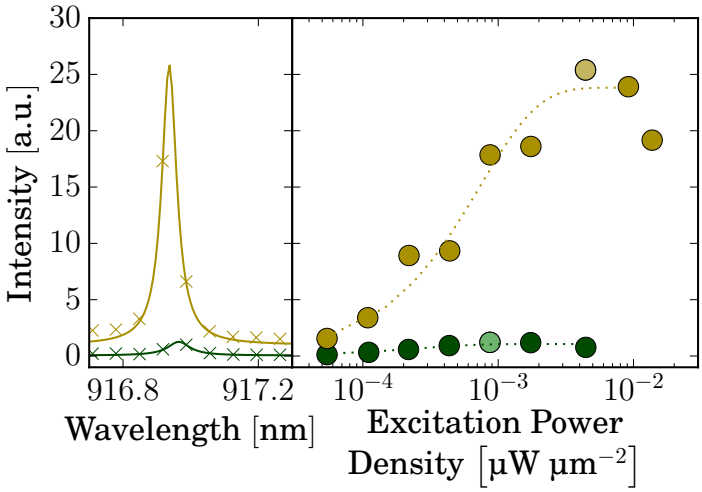

Figure 4.9: Left panel: Zoom-in of spectra from a single PL emission line from a single QD (symbols), collected at saturation level before (green) and after (yellow) ring deposition, taken at $T = 10\,\mathrm{K}$, shown with Lorentz fits (lines) Right panel: Emission intensities as a function of excitation power density (symbols) and their fits (dashed lines) for the emission lines shown in the left panel (same colour coding), lighter points indicate the spectra shown. Intensities are normalized to QD peak emission in bulk at saturation.

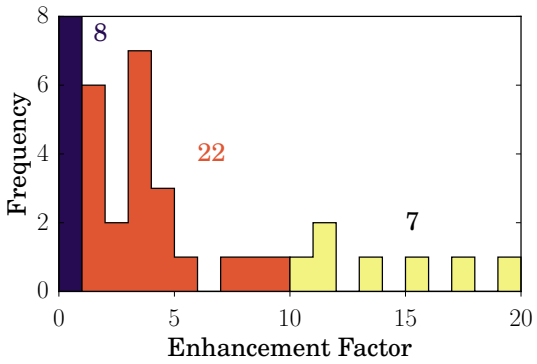

Figure 4.10: Histogram of measured enhancement factors for fabricated devices, with colour-coded totals.

bottom reflectors to capture light lost into the substrate (as shown in the simulation in Figure 4.2); SILs to further focus and extract emitted light; optical fibres deterministically positioned over the nanorings to collect emission and direct it to experiments in a monolithic device.

4.7 Solid Immersion Lenses

So far with the metallic nanorings, enhancement of emission brightness has been demonstrated, up to factors of $\times 25$ using a broadband lensing effect. This has proved the principle of the nanoring devices; however, enhancement occurs differently over the emission lines. Charge-tuning can be used to unravel the behaviour, increased source brightness would aid in these measurements. As to prevent any artefacts from this further enhancement, all of the emission lines should be enhanced equally. To this end, another broadband device is needed to further enhance the emission. A solid immersion lens (SIL) can fulfil this function: is is a broadband device, and is relatively simple to integrate into the ring system.

4.7.1 What are Solid Immersion Lenses?

A SIL is a lens which fills the object space (the gap between the lens and the object) with solid material [173], liquid-immersion lenses achieve this by using a range of oils and solvents with engineered optical properties. One method of filling the object space, is to simply place the lens directly onto the object itself[3]. They are typically used to reduce the diffraction limit of conventional far-field microscopy. The high-index material of the lens diffracts light to a lesser degree than air, resulting in a smaller diffraction limit under the lens compared to without the lens at all. They allow a larger collection angle of light from an emitter to be directed to collection optics, Figure 4.11. By using a SIL of intermediate refractive index, between that of the sample and air, total internal reflection can be reduced at the sample/SIL interface – allowing more light to be collected.

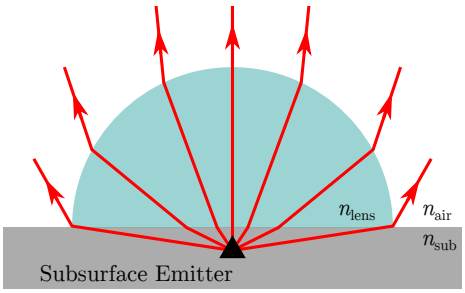

Figure 4.11: Schematic of a hemispherical SIL, showing: a SIL (pale blue), with refractive index $=n_{\text{lens}}$; a substrate (grey), n_{sub}; and air, n_{air}. The red lines are ray traces showing the lensing of light emitted from an emitter (black triangle) under the centre of the SIL.

[3] In some cases, a thin layer of grease or oil is used between the sample and lens surface to ensure a good optical contact [27].

An optical micro-lens is a simple optical component to introduce, a hemisphere or super-hemispherical dome of high-index material placed over a light emitter. There are several approaches to implement them. The first is to simply place 'by-hand' a millimetre-sized glass SIL over the sample [27]. Such SILs are readily available and no not require fabrication of the SIL by the end user. They are typically able to achieve enhancements of $\sim \times 5$ [173].

For quantum dot (QD) samples, an alternative approach is to fabricate the SIL on the sample deterministically. Using 3-dimensional (3D)-electron beam lithography (EBL), a dome of resist can be patterned over the site of a QD in bulk. Etching is then used to transfer the SIL pattern to the material of the capping layer, resulting in a SIL $\sim 1\,\mu m$ in diameter. Extraction efficiencies up to $23(\pm 3)\%$ have been achieved using such SILs [174]. Cathodoluminescence spectroscopy is used to locate QD during exposure. This requires specialized lithography equipment that can cryogenically cool a sample and perform optical characterization all in-chamber.

Aligned optical 3D-printed polymer SILs are fabricated by using a laser to expose a photoresist, forming a SIL. During optical characterization, *in situ* lithography is used to pattern markers around a selected QD, which are etched to transfer the markers to the substrate. A scanning laser system can use these marks for alignment, and expose a hemispherical dome over the QD, forming a SIL of diameter $\sim 20\,\mu m$. Enhancement factors of only ≈ 2 are reported [168], due to lens shape and index contrast available.

A simpler technique is to fabricate larger lenses and remove the need to define the lens shape by raster-scanning. By also moving towards a super-SIL shape, where the lens is super-hemispheric, larger magnifications are available. The lens is formed by dispensing a droplet of ultra violet (UV)-curable epoxy ($\eta = 1.54$) over the sample, electrowetting is used to control the SIL shape [175, 176]. The process is performed with the sample immersed in glycerol, which increases the contact angle between the droplet edge and the substrate, by modifying surface tensions at the interface [177]. Finally the epoxy is cured using UV light. An example of a finished super-SIL is shown in Figure 4.12. Optical magnifications of $\times 1.8$ have been reported, with emission enhanced by $\times 4.0$ [178], for WSe_2 flakes on a SiO_2 substrate. By combining this type of super-SIL with metallic nanorings on a GaAs substrate (which has a higher refractive index contrast), larger enhancements should be available, leading to high brightness photon sources.

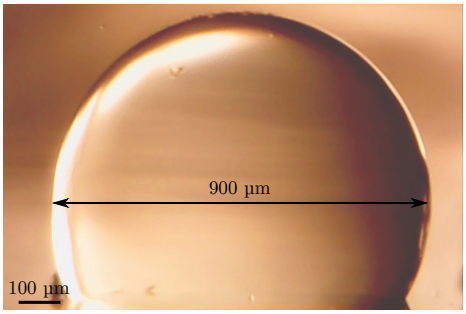

Figure 4.12: Optical micrograph of a typical UV-cured resin super-SIL, with diameter shown, taken whilst immersed in glycerol.

4.7.2 Characterization and Results

Initial characterizations were made using the dual light emitting diode (LED) configuration to image the sample, Figure 4.13. By comparison with the photoluminescence (PL) image shown in Figure 4.7, it can be seen that the image is enlarged by the SIL. Another effect is modification and distortion of the image, the QD shown in Figure 4.13 looks 'diffracted', this distortion occurs to emitters that are located a far away ($> 80\,\mu m$) distance from the SIL apex.

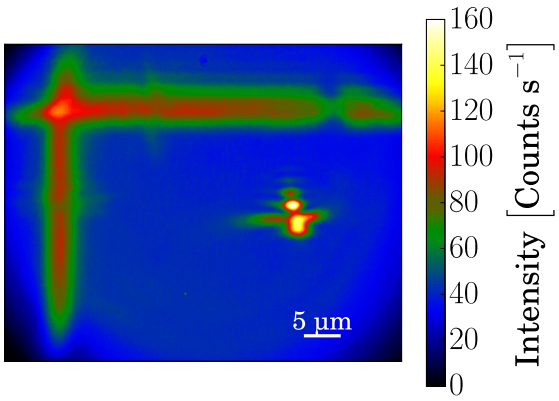

Figure 4.13: PL image of solid state quantum dot (SSQD) with nanoring imaged through a SIL using 455 nm LED excitation and 940 nm LED illumination, with a 550 nm longpass filter (LPF). 2 s integration, 180 acquisitions, no gain, 10.5 K.

To characterize the effects of the individual components, QDs were spectrally characterized in bulk, after nanoring deposition around the QDs and after SIL deposition over a target area. As with the nanorings alone, QDs were selected to be used as references to quantify the spectrometer coupling, which were outside of the SIL area.

Pump-power resolved measurements were taken at each stage, to determine the brightness of individual QDs at saturation. The flux of photons on the first lens is reported here, as this measure allows direct comparison of the photon source to others, decoupling the losses of the experimental apparatus, the calculation of the transmission factor is shown in section 4.7.3. Typical results are shown in Figure 4.14, the QD intensity is first enhanced by the ring and then further by the SIL. The effects stack, allowing photon fluxes as high as 900 kHz from a single QD. The plot shows that the nanoring provides enhancement of $\times 4.3$ and the SIL provides $\times 5.4$, for a total combines of $\times 23.1$.

The statistics of multiple devices was investigated, both for QDs in bulk and those with nanorings. These are shown in Figure 4.15, where the highest enhancement by the SIL is $\times 10$; the SIL enhancement is uniform for all emission lines, unlike that of the nanorings. There is some variation in the enhancement factors of the emitters under the SIL, this can be attributable to the distance the emitter is from the apex of the SIL, as shown in Table 4.1, however the distances are all below 100 µm, which is an order of magnitude below the SIL diameter of 900 µm. An optimally positioned nanoring is able to provide $\times 25$ enhancement of emission (shown in Figure 4.9); which, if directly under the SIL apex would be further enhanced by $\times 10$; provides a theoretical enhancement of $\times 250$ for a

single emission line. This could be further increased by the incorporation of a back reflector into the substrate.

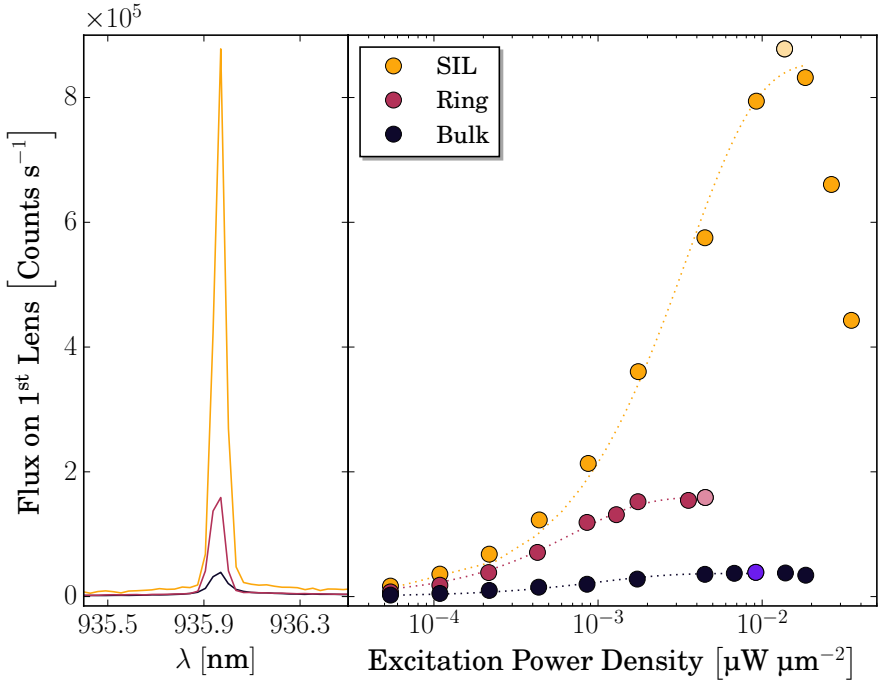

Figure 4.14: Left panel: PL spectra collected at saturation pump power for the QD in bulk (purple), with nanoring (pink) and after super-SIL deposition (amber). Right panel: Power resolved intensity of the emission lines shown in the left panel, lighter dots correspond to the the spectra shown in left panel, dashed lines are fits to the data using Equation 4.1.

4.7.3 Setup Transmission Calculation

To be able to compare brightnesses of light sources, it is most useful to compare the flux of photons incident on the first collection optic; as different experiments will vary, making detector count rates incomparable. To this end, the transmission of the set-up (as shown in Figure 4.16), from photon entry into the objective to registration as a count, needed to be determined. This required evaluation of four parts of the setup: the objective, the path to the spectrometer, the spectrometer itself, and the charge coupled device (CCD).

The objective and path to spectrometer transmission values were determined by shining a laser along the light-path and measuring the beam power to determine attenuation. Data-sheet values were used for the CCD quantum efficiency, gain (photon to electron conversion), and window transmission.

To determine the transmission of the spectrometer, a laser beam of a known power was shone into the spectrometer and the CCD count rate recorded. A measurement of the laser power incident on the spectrometer was made, and by using wavelength to determine the energy of a single photon, the number of photons incident could be calculated. By convolving: the CCD gain losses,

Device №	Distance [µm]	Error [µm]
1	78.77	0.06
2	28.48	0.14
3	97.01	0.05
4	70.35	0.06
5	54.98	0.08
6	54.98	0.08
7	42.87	0.09
8	99.22	0.03
9	71.28	0.03
10	90.12	0.03
11	58.03	0.04
12	20.82	0.11

Table 4.1: Distances of numbered devices from apex of the PL.

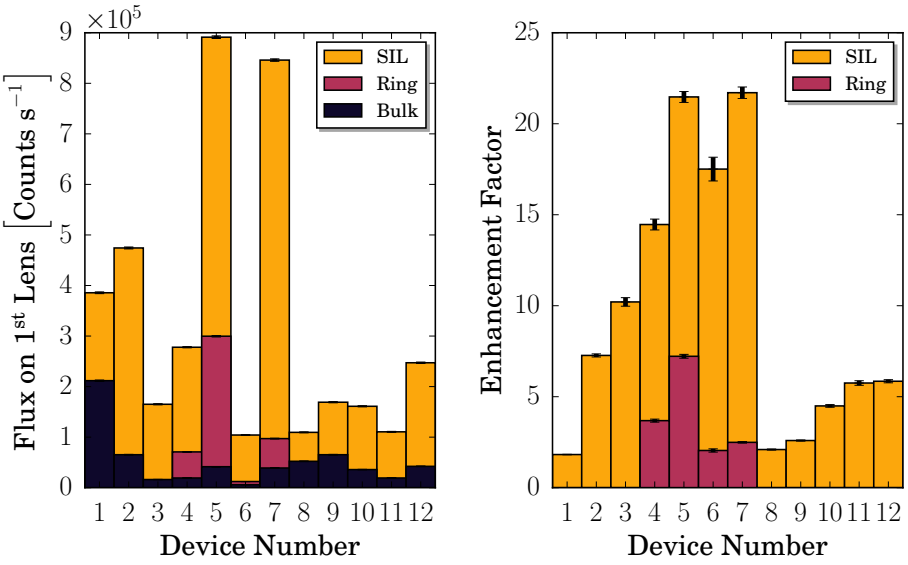

(a) (b)

Figure 4.15: (a) Histogram showing the photon flux incident on the first lens at pump saturation power for QDs in bulk (purple), with nanoring deposited around the QD (pink) and with a super-SIL (with or without nanoring) deposited onto the sample surface (amber). (b) Enhancement factors attributable to the nanorings and super-SILs, compared to emission in bulk; for the QDs shown in (a), using same colour coding. For devices 4 to 7, the enhancement for the PL includes that of the nanoring.

detection efficiency, and window losses; the number of photons incident on the detector window could be calculated. The spectrometer transmission is the difference between the photons incident on its entrance and those incident on the detector window. The transmission of the objective and optical path to the spectrometer were measured by sending a laser through these components and measuring the reduction in beam power.

The transmission values for the system are shown in Table 4.2. The spectrometer transmission T_{spec} is directly measured and is a convolution of the reflectivities of the components in the spectrometer (R_{m} and R_{gra}). The total transmission is 1.76(±0.08)%.

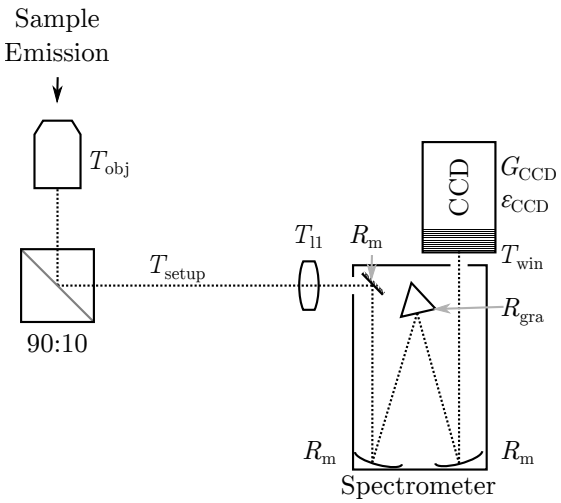

Figure 4.16: Diagram showing transmission and reflectivity of optical components in the µ-PL set-up, not shown: T_{spec}, the transmission of the spectrometer system.

	Component	F
T_{obj}	Objective	0.641
T_{setup}	Optical Path to Spectrometer	0.635
T_{l1}	Lens	0.992
T_{spec}	Spectrometer	0.230
T_{win}	CCD Window	0.994
$\varepsilon_{\mathrm{CCD}}$	CCD Q.E.	0.189
G_{CCD}	CCD Gain	0.333
	Total	$1.76(\pm 0.08) \times 10^{-2}$

Table 4.2: Fractional values (F) for transmission, reflectance, or efficiency for parts of optical path identified in Figure 4.16. The total transmission indicates the transmission from first collection optic to a registered count on the detector.

4.7.4 Conclusions

The combination of a deterministically positioned super-SIL and metallic nanoring has been shown to provide a cumulative enhancement of $\times 20$, with the potential of up to $\times 250$ with optimally positioned nanorings and super-SILs (combining the $\times 10$ SIL enhancement with the $\times 25$ from a nanoring). The QDs examined have a peak bright emission rate approaching 1 MHz. The device is wavelength insensitive as it relies entirely on the broadband lensing effects of the nanoring and SIL. The emitters remain in bulk, avoiding the detrimental effects that lead to reduced coherence and stability of the light emission, caused by etched surfaces in close proximity to the emitter [158]. The fabrication of these hybrid devices is relatively simple, the nanorings are a single lithographic process that is within the reach of optical and nano-imprint lithography; the SIL requires a simple immersion and dispensing set-up. These devices are scalable and can work with a selection of solid-state emitters which can be placed in the centre of the nanorings, or embedded below a protective capping layer.

Chapter 5

Quantum Dots for Plasmonic Applications

> Why can't we make them very small, make them of little wires, little elements – and by little, I mean *little*.
>
> Richard Feynman
> *There's Plenty of Room at the Bottom (1959)*

PURCELL enhancements are needed to increase the spontaneous emission rate from emitters such as solid state quantum dots (SSQDs) and decrease de-coherence effects [69], leading to brighter and highly indistinguishable single-photon sources. Currently the nanoring devices are only able to provide a broadband lensing effect, without any Purcell enhancement. Plasmonics have been shown to allow Purcell enhancements [179], the metallic nanoring could be adapted to also act as a plasmonic antenna. Quantum dots (QDs) provide high quality optical emission: high single-photon purity [27], high indistinguishibility [180], high brightness and emitter stability. However, the relatively thick capping layers required for high optical quality ($> 30\,\text{nm}$) [132] mean that the QDs couple poorly to the highly local field enhancement provided by plasmonic devices. Attempts using patterned substrates to grow SSQDs with thin capping layers (10 nm) have resulted in increased broadening of the emission lines (up to 1 meV) [181]. Presented here is an alternative growth technique, whereby droplet QDs can be grown with thin capping layers, whilst retaining good optical characteristics. The sample growth was performed by the group at KIST, headed by Jin Dong Song. The atomic force microscopy was performed by Luca Sapienza. I fabricated a reference grid onto a sample and performed optical characterization. This work is published as [182].

5.1 The Road to Plasmonic Enhancement

Plasmonic devices confine the electric field on the nano-scale, using metallic structures [127] and have been shown to allow modification of spontaneous emission [179] and can alter emission directionality [183]. This tight confinement of the field has found application in scanning-probe microscopy [184], where field concentration can provide enhanced interaction at the end of a scanning tip. Light concentrating structures exhibit modest quality-factor (Q-factor) of $\sim$ 10-100, however they can provide mode volumes much smaller than dielectric cavities, $V \sim \left(\frac{\lambda}{2}\right)^3$, leading to large Purcell factors [185]. Bowtie devices have emerged as one of the leading device types [186] for emission enhancement, due to their strong sub-wavelength light confinement, high spectral tunability, and polarization control. They have been demonstrated with single-molecule florescence, where emission was enhanced by ≈ 1340 [128].

The tight field confinement poses a problem when trying to couple emitters to plasmonic devices, since emitters need to be in close proximity (few nanometres range) in order to couple with the plasmonic mode [185]. This renders SSQDs unsuitable, the capping layer is too thick. As the capping layer is thinned the line-width broadens and the photoluminescence (PL) intensity decreases, due to dephasing and spectral diffusion [132]. Line-width broadening, caused by dephasing, is undesirable as it decreases indistinguishibility of the emitted photons, as two emitted photons can have different energies to each other, with their wavefunctions no-longer being identical; decreased brightness means that the source emits less photons; both of these factors decrease the usefulness of SSQDs as a viable single-photon source for quantum information technologies. Plasmonic devices with SSQDs have been demonstrated using QDs with line-widths of $\sim$1.1 nm [187].

Lack of high-quality optical emission from suitable SSQDs has prevented them from being extensively used with plasmonic devices. This has led to other classes of quantum light emitters being used: colloidal quantum dots [188, 130], single molecules [128], fluorescent dyes [189], and nitrogen vacancy centres [82]. Some emitters (colloidal QDs, molecules and dyes) suffer from instability which leads to blinking and bleaching over varying time-scales, making device longevity a key barrier. Also, these emitters are incorporated into devices by means of dip- [189] and spin-coating [188] of plasmonic device substrates. Such fabrication techniques are non-deterministic so lack scalability.

Currently the dominant route to growing SSQDs with thin capping layers has been to use filled nanoholes. During growth, nanoholes are etched into the substrate *in situ* using local droplet etching. Ga droplets are formed on a GaAs substrate, with no As flux in the deposition chamber. This causes As in the substrate to diffuse into the Ga droplet, causing it to sink into the surface. This forms a cone-shaped Ga feature buried in the substrate, a filled nanohole [190]. Using this technique thin capping layers of a few nanometres are possible. However, the apex of the cone (where exciton wave-function is concentrated) is pointed into the substrate – further away from the localized field of a plasmonic device on the substrate surface. Table 5.1 shows the current state-of-the-art in growth of thin capping layers. There is a trend of increasing line-widths as capping thickness decreases, with QDs accessible to plasmonics characterized by broader emission lines compared to Stranski-Krastanov (SK) QDs.

Droplet epitaxy is an alternative technique to form quantum dots on a sub-

Capping Thickness [nm]	Line-width	
10	1 meV	[181]
12.5	344 µeV	[191]
15	186 µeV	[192]
100	70 µeV	[193]

Table 5.1: Comparison of reported line-widths of nanohole QDs with thin capping layers, showing the trend of line-width increase with decrease of capping thickness.

strate. The GaAs substrate is heated in an As flux at high temperature (590°C) to stabilize the surface. The chamber is then heated to $\sim$ 200°C and a Ga flux is then introduced, equivalent to $\sim$ 2-3 monolayers. The Ga forms droplets on the substrate surface [194]. After *ex situ* annealing to eliminate strain, the droplets can be capped with AlGaAs using conventional molecular beam epitaxy (MBE) to complete the band-structure [195]. Typically this capping layer is thinner that that required for SK QDs: line-widths of 26 µeV are reported with 40 nm capping [196]; and capping at 10 nm is reported, but optically characterized at high density [195]. By introducing As into the chamber after droplet formation, a range of different shapes can be obtained [197]: QDs, double-QDs (two QDs next to each-other, within $\sim$ 30 nm), Q-rings (a ring of low bandgap material) [198], and double-Qrings (two concentric Qrings) [199].

5.2 Droplet QD Growth with Internal Thermal Heating

The size and shape of a droplet control the optical characteristics of the QD, of paramount importance for quantum photonics. The shape of droplet QDs can change during post-growth annealing performed to improve the crystalline structure; this step is necessary as during droplet epitaxy the group III and V elements become separated. Thin capping layers are deposited over the droplets to help maintain their shape at high temperatures, which can cause deformities of shape or loss of the droplets. Rapid thermal annealing (RTA) is typically used post-growth to anneal the crystalline structure.

Internal thermal heating (ITH) is a process where the annealing takes place in the growth chamber immediately after the droplet growth, at high vacuum. This process allows better control of the droplet height compared to *ex situ* RTA. The annealing also takes place within the same ultra-high vacuum growth chamber, reducing processing time and decreasing contamination. The capping layer can also be grown at the ITH temperature – higher than the formation temperature of the droplets.

A schematic of the growth procedure is shown in Figure 5.1. Firstly a GaAs substrate de-oxidized in As_4 at 580°C, and a 50 nm-thick $Al_{0.3}Ga_{0.7}As$ layer is grown on a $\sim$200 nm GaAs buffer (as shown in Figure 5.2). On this surface, Ga droplet islands are grown (substrate temperature: 321°C, 2 Ga monolayer (ML) growth, 0.5 ML/s Ga flux as GaAs equivalent), with growth interrupted after 10 s. After cooling to room temperature, an As_4 flux of 1×10^{-5} Torr is injected

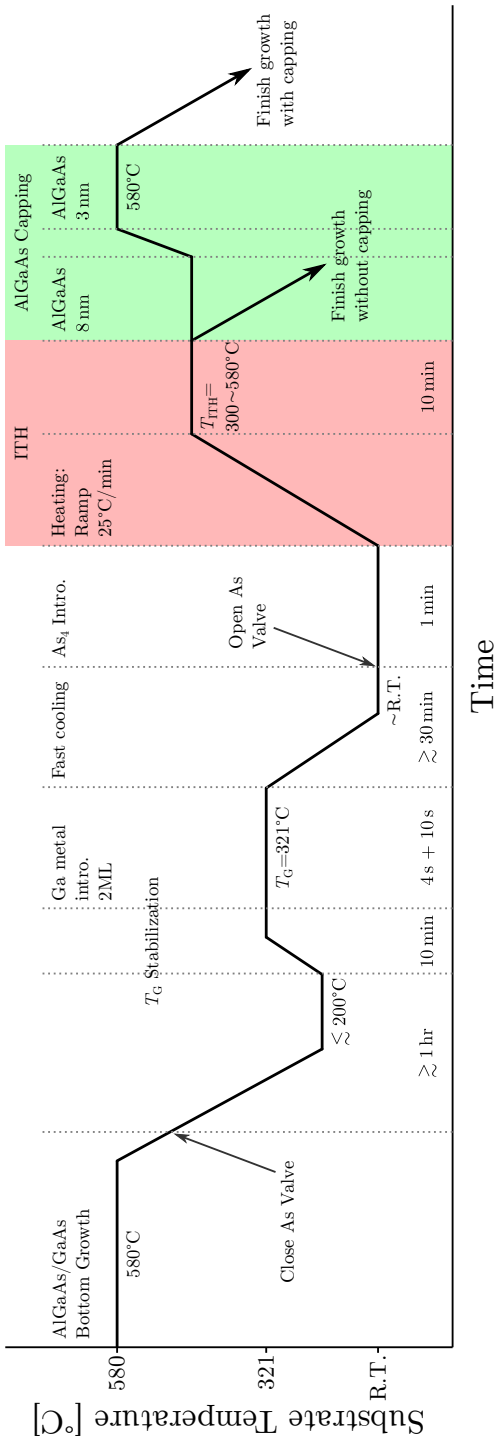

Figure 5.1: Schematic of droplet QD growth recipe, with an ITH step. Axes not to scale.

into the growth chamber, on the liquid Ga droplets. The substrate temperature is then brought up to T_{ITH} for the ITH process. This temperature was varied for study, with 580°C proving optimal. The ITH for island growth is continued for 10 mins, with an As_4 flux of 6×10^{-6} Torr, to prevent As evaporation (which would cause droplet deformation). An 11 nm $Al_{0.3}Ga_{0.7}As$ capping layer is grown over the Ga islands after the ITH is complete: an initial 8 nm is grown at 563°C, with an additional 3 nm grown at 580°C. The higher temperature of capping layer growth (the same as the ITH) reduces formation of defects, leading to a reduction in emission line-width by removing strain effects. Narrow line-width is a key attribute for high indistinguishibility single-photon sources.

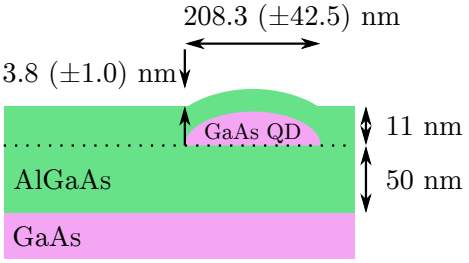

Figure 5.2: Schematic of droplet QD, showing growth thicknesses and average measurements from capped QDs, not to scale.

5.3 Characterization

Atomic force microscope (AFM) examinations were made of samples grown using ITH, which allowed the morphology as a function of T_{ITH} to be characterized. The width (long-axis) of the droplets did not significantly change with T_{ITH}, with the height decreasing as T_{ITH} was increased to 580°C. Figure 5.3 shows a 11 nm capped droplet QD annealed at $T_{\mathrm{ITH}} = 580$°C, with a height of 8.7 ± 3.4 nm, and width 104.2 ± 13.4 nm. The AFM measurements indicate a 3.8±1.0) nm deformation of the sample surface over a QD location, this is less than the thickness of uncapped droplets, so the capping layer is likely to be less than the deposited 11 nm directly over the QDs. Post-capping, the change in height, but not width results in a flattening of the tops of the droplets, which is consistent with previous accounts [200].

The optical properties of the droplet QDs were examined. Firstly the location and density of the QD growth was examined. Whilst illuminating the sample with a 455 nm light emitting diode (LED) excitation source, the PL in a narrow window of 700-800 nm was imaged, Figure 5.4. This was achieved using edge-pass filters, and was necessary to eliminate the bright wetting-layer PL at 820 nm. The image shows the high density of QDs which was present across the chip, which was confirmed by AFM examination, this shows that most emitters are optically active. The density of droplet QDs was determined to be $\sim 6\,\mu\mathrm{m}^{-2}$.

Single QDs were selected, an example is circled in Figure 5.4, and excited with the 405 nm laser, of spot diameter 2 µm. Sharp emission lines are visible in the spectrum from a single emitter, Figure 5.5a, with single emission lines as narrow as 0.175 nm full-width half-maximum (FWHM) from a Lorentzian fit, Figure 5.5c. By taking power resolved spectra, a power series can be taken,

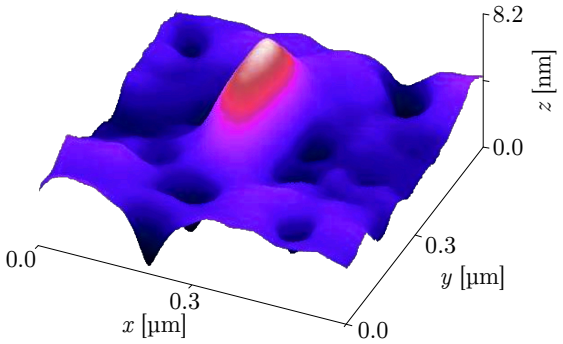

Figure 5.3: Atomic force micrograph of a single droplet QD. AFM parameters: tip radius, 7 nm; spring constant, 26 Nm^{-1}; resonance frequency, 300 kHz.

Figure 5.5b; the response is linear, indicating that the QDs are operating below saturation, this could be attributable to poor absorption at the pump wavelength of 405 nm, which was far away from the 700-800 nm emission region. The response can be reproduced over multiple cool-down cycles, showing that the emission is stable, despite the thin capping layer.

The spectrum in Figure 5.5c shows a sharp resonance centred at 727.4 nm and a broader peak at longer wavelengths. The latter could be due to coupling to phononic states, so-called phonon sideband. Even though at the measurement temperature of 4.8K, it would be expected that most of the phononic modes would be inactive. However some transitions between the electronic excited state and the phononic manifold might still be possible and give rise to a lower-energy and broader emission peak, as see for instance in InAs/GaAs QDs [201].

The side-band visible in the spectrum (Figure 5.5c) could be attributed to phonon interaction. The ground and excited states have a number of vibrational modes, providing a manifold of different energy transitions [72]. At the low temperature ($T = 4.8\,\mathrm{K}$), most photon emission is into the zero phonon line (ZPL); however other phonon-mediated pathways are possible and give rise to lower-energy photon emission forming the side-band.

5.4 Conclusions

Droplet epitaxy using ITH has been shown to produce SSQDs with thin capping layers of 11 nm, and narrow line-widths (175 pm) compared to state-of-the-art 10 nm thin-capped QDs (0.5 nm) [181]. This provides a route to exploiting the benefits of SSQDs, namely the superior optical properties and stability of a solid-state emitter, whilst dispensing with the thick capping layer which posed a barrier to plasmonic applications [127].

Such emitters are ideal for studying plasmonic effects, example structures which can enhance the light-matter interaction include: metallic nanorings deterministically deposited around the emitters, chapter 4; bowtie antennas [186]; or metallic nanocubes [189]. In comparison to other fluorescent emitters such as dye molecules and colloidal quantum dots which have been the workhorse emitters in plasmonic experiments [185], the droplet QDs provide stable emission which is not degraded by laser excitation, changes in temperature or environ-

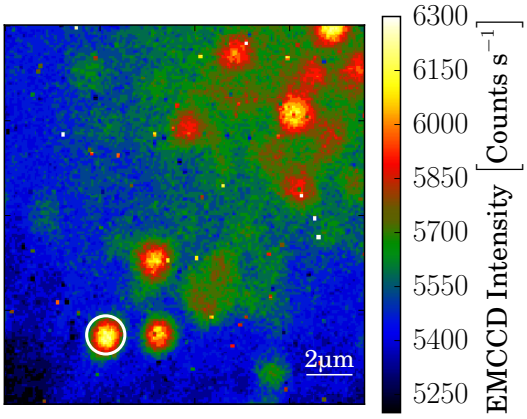

Figure 5.4: PL image of the droplet QD sample, showing emission in the 700-800 nm region, under 45 nm LED excitation. Circled QD indicated location where spectral characterization was performed in Figure 5.5 Image parameters: 2 s integration, 180 acquisitions, $\times 200$ gain, $T = 4.8$ K.

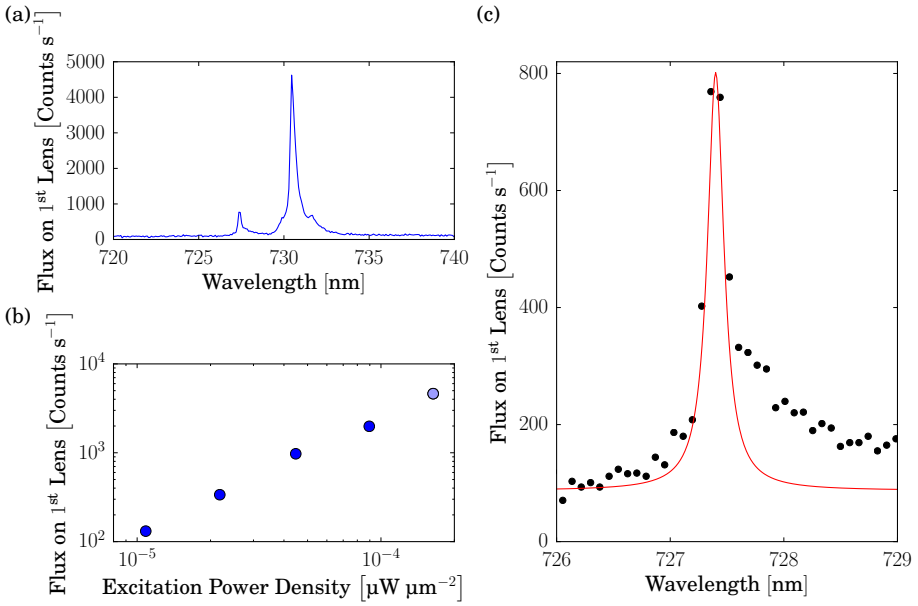

Figure 5.5: (a) PL spectrum of droplet QD sample, under 405 nm laser excitation, with a power density of 1.8×10^{-4} µW/µm^2 at 4.7 K, showing sharp emission lines. (b) Emission intensity as a function of excitation laser power density, for the emission line at 727.4 nm, highlighted point corresponds to spectrum show in (a). (c) Zoom-in on emission line at 727.4 nm (symbols) from panel (a), with a Lorentzian fit (red line).

mental interaction. They are also compatible with deterministic device fabrication, where emitters can be pre-positioned (as in section 3.2); in comparison to QDs which are deeply buried, the shallow-buried droplet QDs can be located using alternative techniques such as AFM. This can allow charge-tunable nanoring devices to be developed, which exploit plasmonics for Purcell enhancement of QDs, to allow bright single-photon emitters.

Chapter 6

Photonic Crystal Cavities

> And now for something
> completely different.
>
> Monty Python

PHOTONIC crystals introduce a photonic bandgap into material, providing control over light propagation. By carefully introducing defects into their periodic structure, devices can be made: such as cavities. As the target wavelength of photonic crystal (PhC) devices shortens, to head form the infra-red into the visible light regime, the feature sizes (lattice periodicity and hole radius) of the devices become smaller. However, imperfections introduced during fabrication remain, and non-negligibly degrade the performance of devices at the size-scales required for visible light operation[1]. Consequently PhCs require high levels of engineering to fully realize design performance. The PhC cavity provides a handy potted example demonstrating this. The simulations of the device were performed by Josh Nevin, with Chris White helping with characterization and analysis of the devices. I fabricated the devices, performed characterization and analysis.

6.1 The L3 Cavity

As mentioned briefly in section 2.2.2, cavities can be made within a photonic crystal by removing some of the air holes: creating a small region of bulk material with no photonic bandgap, surrounded by a photonic band-gap material. PhC cavities are a very attractive device, as they offer a high level of configurability. Firstly the photonic crystal lattice can be tuned, by altering the home size and separation. Then, holes surrounding the cavity can can be altered (displacement from periodic spacing, and hole size) to precisely tune the cavity.

Here, discussion shall be restricted to the 2-dimensional (2D) geometry only. Cavities are usually labelled by the number of missing holes, for example the device shown in Figure 6.1 is an L3 cavity. To maximize the light-matter interaction a high quality-factor (Q-factor) and a small mode volume are desired.

[1] Fabrication imperfections also affect devices at longer wavelengths, however devices for shorter wavelengths are more sensitive.

Typically the L3 has served this purpose, whilst the L1 (a single hole removed) cavity has a smaller mode volume, it is too leaky; and an L2 has a node at its centre.

The PhC itself is defined by: the lattice constant (a), the centre-to-centre spacing of the holes; and the hole radius (r). It is convenient to describe the dimensions as a fraction of a, as this prevents overlap or hole size from exceeding the lattice parameter. To create the L3 cavity, three holes are removed, Figure 6.1.

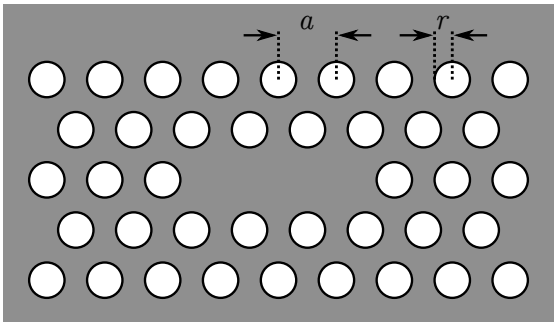

Figure 6.1: Schematic of L3 PhC cavity, with holes (white) etched out of a slab of material (grey). The PhC parameters are shown: lattice constant, a; and hole radius, r.

This type of cavity has been successfully used across several wavelength ranges: in the telecom C band at 1.57 µm with $Q = 45,000$ [117]; at ~ 950 nm with $Q \approx 30,000$ [137]; and in the visible at ~ 650 nm, with $Q = 1460$ [202]. The clear trend here is that Q-factor decreases as wavelength decreases, with devices for the visible providing Q-factors $\times 30$ lower than in the telecom band. Other tuning schemes have also been applied: groups of holes at the end of the cavity can be moved as a group (with hole position tuned using a genetic algorithm), giving rise to $Q \approx 1,960,000$ at 1.55 µm [203]; by designing for longer wavelengths, a longer cavity is permissible, such as an L15 which has been demonstrated to have $Q = 9,000,000$ at 1.63 µm [204].

The visible light regime is of particular interest as a number of quantum light emitters are optically active in this region (see Table 2.2). However as the wavelength of operation decreases, the feature size of the PhC devices must decrease as well, with visible light devices having lattice constants of $a \approx 270$ nm and hole radius of $R \approx 0.3a$. Shorter wavelengths are also more sensitive to imperfections in the devices. Defects introduced during fabrication to begin affect device operation at these small size scales, decreasing performance. Examples of these defects include: distorted hole shapes (non-circular), roughness of the hole size-walls, non-verticality of the hole side-walls. These imperfection increase scattering of light out of the crystal plane, and reduce the reflectivity of the cavity edges. Work on devices for visible light confinement has progressed slowly, with $Q \approx 1000$ at 683 nm in 2005 with an L1 cavity [126]; $Q = 1460$ at 660 nm in 2007, from a simulated $Q \approx 4700$ [202]; later work in 2010 produced $Q = 1200$ at ~ 648 nm [205]. Actual device performance is $\sim \frac{1}{3}$ of the design where the device has been simulated prior to fabrication. This is again due to unavoidable fabrication defects which modify the original design.

Visible light operation is desirable because there are a number of emitters that can produce quantum light in the visible: nitrogen-vacancy (NV) centres, colloidal quantum dots (QDs), carbon nanotubes, 2D materials, and molecules. Photonic crystals have been unable to adequately service this wavelength region, fabricated devices are susceptible to imperfections introduced during fabrication, which reduce actual device performance compared to simulations. Therefore, a new approach is needed to see if the performance of the L3 cavity can be pushed further.

6.2 Device Design

To simulate the operation and to optimize the L3 cavity design finite-difference time-domain (FDTD) simulations were performed [162]. In this case, light was injected into the cavity region by electric dipoles placed randomly, this is to ensure approximately uniform coupling of light to the cavity mode. As the quality of the cavity is quite high (> 300), the electric field is unable to fully decay in the simulation, preventing Q-factor from being determined directly from the device resonance spectrum. Instead, the envelope of the decay is examined using [206]:

$$Q = \frac{-2\pi f_{\mathrm{R}} \log_{10}(e)}{2m} \tag{6.1}$$

where: f_{R} is the frequency of the mode resonance; m is the time constant of the electric field decay.

The L3 cavity resonance can be modified by altering five characteristic parameters (shown schematically in Figure 6.2): the lattice constant (a); the role radius (r); the radius of the holes in the rows above and below the cavity region (r'') and at the ends (r'); the end holes can also be displaced from the periodic lattice positions, by a distance d (applied symmetrically to the pair of holes).

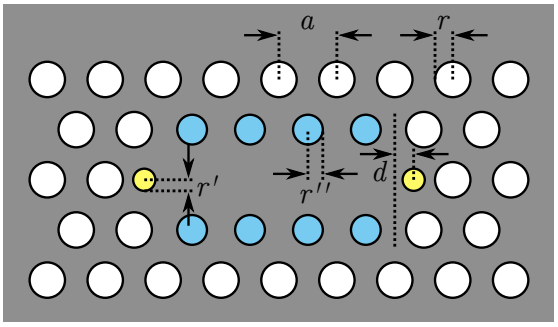

Figure 6.2: Schematic of L3 PhC cavity, with holes (white) etched out of a slab of material (grey), showing critical parameters: lattice constant, a; hole radius, r; radius of cavity end-holes (yellow), r'; radius of holes above and below cavity (blue), r''; end-hole displacement, d.

The simulation time for a single device was in the region of ~ 6 hrs; this coupled with the need to tune 5 parameters, made a full optimization run prohibitively time-consuming. Instead, parameters were swept individually, with optimal values being kept; this slowly walked the device design to a maxima. The result was an L3 cavity with a Q-factor of 4816, with design parameters:

$a = 270\,\text{nm}$, $r = 0.3a$, $r' = 0.2a$, $r'' = 0.26a$, $d = 0.2a$, membrane thickness $T = a$. A simulation of the electric field is shown in Figure 6.3; the tight confinement of the electric field in the centre of the device can be seen.

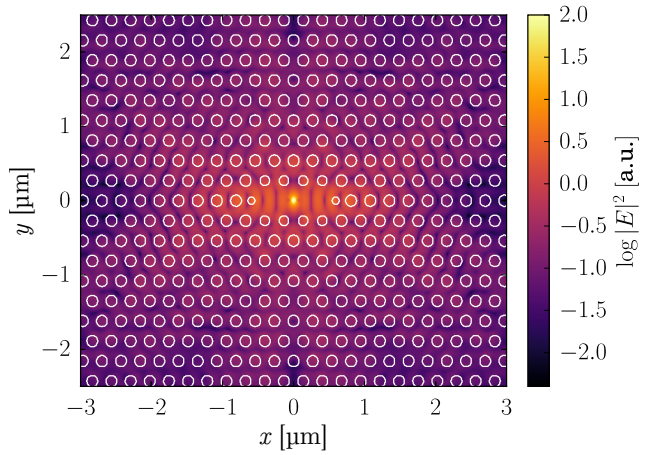

Figure 6.3: FDTD simulation of the electric field of the L3 cavity, with optimized design parameters. A dipole source was used to inject broadband light into the cavity. The simulation shows a localization of the electric field in the centre of the cavity region.

6.3 Fabrication

Photonic crystal devices were fabricated using a multi-stage planar process, Figure 6.4, recipes described in section A.2. Firstly a 250 nm layer of silicon nitride (Si_3N_4) was deposited onto a {100} Si substrate using plasma-enhanced chemical vapour deposition (PECVD), Figure 6.4a. PECVD is a process where precursor gas species are injected into a chamber where a plasma is formed. Large inductive coils encircle the chamber provided with high-power alternating current, energizing the plasma. Within the plasma, the precursors react and are deposited onto the target sample. The photoluminescence (PL) form Si_3N_4 is due to defects in the crystal structure [207, 208]. Different deposition techniques affect the number of defects, PECVD produces impure hydrogen-containing Si_3N_4 films [209], which upon examination provided the brightest PL signal. A bright PL signal is useful as it is able to inject more photons into the cavities, so can excite more cavity modes and lead to a lower signal-to-noise ratio of cavity resonances.

Using the simulated L3 cavity design, lithography masks could be prepared; several variations of the device parameters were made: the lattice constant (a) was varied $\pm 10\,\text{nm}$; hole radius (r) was varied by $\pm 0.02a$. This was to provide a selection of different sizes to compensate for fabrication defects and errors. Proximity effect correction was applied to the designs to compensate for electron scattering during EBL [210]. The mask is broken down into small parts and assigned dose modifiers. Parts of the mask in close proximity to other parts to be written receive a lower dose, as scattering of the electron beam will

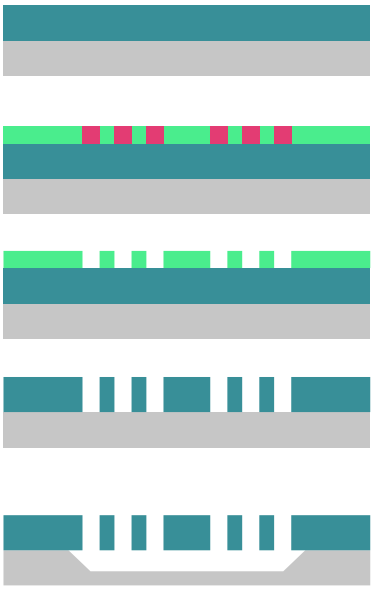

(a) PECVD of Si_3N_4 layer, blue; onto Si substrate, grey.

(b) Electron beam lithography (EBL) write of mask onto resist layer, green. Pink regions show exposed areas.

(c) Resist layer is developed to produce a soft-mask on the top of the substrate.

(d) Inductively-coupled plasma (ICP) dry-etch, etches downwards through Si_3N_4 film.

(e) KOH wet-ech process removes Si from underneath the Si_3N_4 layer, creating a suspended membrane.

Figure 6.4: Fabrication steps for suspended waveguide structures, shown in schematic cross-section.

cause the residual dose received to increase so less exposure is needed in these areas. Conversely, parts that were isolated, such as at the device edges, receive a higher dose.

EBL is used to transfer the finalized mask to the sample. Prior to this process the sample was plasma ashed to clean the surface to improve resist adhesion. CSAR resist was used [211], as it provides the same high-resolution offered by poly(methyl methacrylate) (PMMA), but is more resistant to plasma etch processes which would otherwise quickly destroy PMMA coatings. An electron beam is used to selectively expose areas of the sample, Figure 6.4b, corresponding to the mask. Developing removes the exposed areas, allowing access to the Si_3N_4 below, Figure 6.4c.

The device pattern is then transferred to the Si_3N_4 layer using ICP etching, by removing Si_3N_4 from unprotected areas of the sample (Figure 6.4d). A plasma is created in a chamber and is heated inductively. The plasma is directed downwards onto the sample below. This vertical bombardment permits etching of near-vertical profiles, a key aspect of the planar PhC design. Material is ablated by bombardment and chemically reacts with species in the plasma, carrying the material away. This process is highly sensitive and slight changes in temperature and gas chemistry can alter etch rate, side-wall verticality, and the selectivity of the etch.

The photonic crystal is able to confine light horizontally, by preventing the propagation of wavelengths within the bang-gap region. Confinement within the crystal plane is achieved by total internal reflection due to the refractive index contrast between the Si_3N_4 of the PhC membrane ($n \approx 2.03$ [212]) and air ($n = 1$). This is done by rendering the device a free-standing membrane by removing the silicon underneath. A potassium hydroxide (KOH) wet etch

process is used, as KOH reacts with silicon leaving the Si_3N_4 undamaged[2]. The KOH accesses the silicon substrate via the holes of the PhC device. The KOH etch process is isotropic, attacking the {111} plane preferentially, creating a tetrahedral-shaped trench underneath the PhC device (this is responsible for the cross-shaped shadow in Figure 6.5a). The finished chip is rinsed in isopropyl alcohol (IPA) and dried, rendering the finished L3 cavity device, as shown in Figure 6.5.

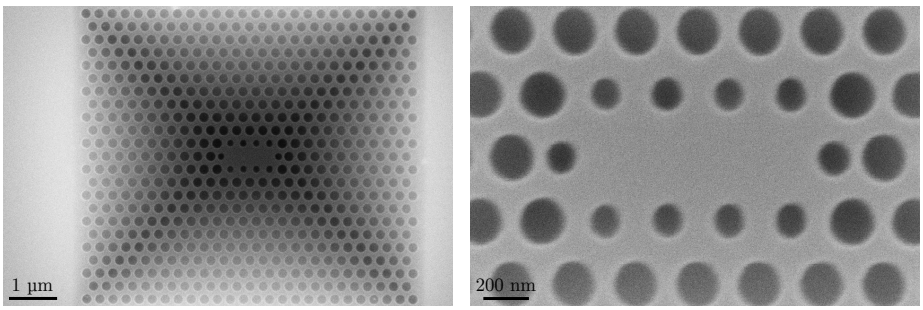

(a) (b)

Figure 6.5: Scanning electron micrographs of: (a) L3 PhC cavity, etched out of a Si_3N_4 membrane, with Si undercut visible underneath device; (b) zoom-in of cavity region.

6.4 Results

The devices exploit PL from silicon nitride as an internal light source to inject photons directly into the PhC cavity. An example bulk emission spectrum is shown in Figure 6.6a, under excitation: a continuous wave (CW) laser at 405 nm. The PL is caused by defects in the Si_3N_4 lattice [207] which are optically active. The absorption occurs at 400 nm and emission occurs at 660 nm, this Stokes shift is caused by the loss of vibrational energy [72]. This broad in-chip light source is able to excite all modes in a device, which is very useful in identifying where resonances are without the need to couple resonant emitters. When a wide area light-source such as a 455 nm light emitting diode (LED) is used, PL images, such as Figure 6.6b can be taken. It shows bright emission from the Si_3N_4 in bulk at the edges of the image and a hotspot in the centre of the device corresponding to the cavity region. Further detail about the cavity (such as exact cavity size, or hole positions) cannot be discerned due to the diffraction limit of the objective.

PL spectra were taken to assess the quality of light confinement within the L3 cavity devices. This was done by using the 405 nm CW laser to excite the central cavity region of a device, with the emitted PL being collected and a spectrogram taken. A typical example of a spectrum is shown in Figure 6.7a: superimposed over the Si_3N_4 PL continuum are several peaks, similar to previous reports where multiple features due to cavity were visible in the 600-670 nm region [202]. The sharp peak at 701.9 nm is shown in Figure 6.7b, with a Lorentzian least-squares

[2]This is not strictly true, potassium has a high diffusivity and impregnates the Si_3N_4, rendering this process non-complementary metal oxide semiconductor (CMOS) compatible.

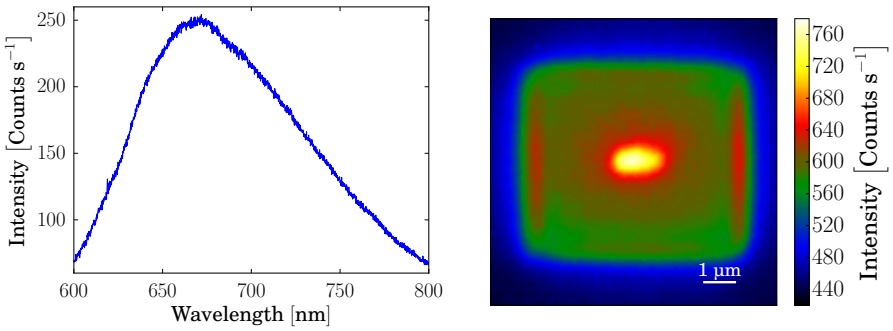

(a) (b)

Figure 6.6: (a) PL spectrum of Si_3N_4 in bulk, under 405 nm CW laser excitation. (b) PL image of an L3 cavity. The cavity in the centre of the device can be seen to emit brightly, the non-zero background is due to PL from the bulk Si_3N_4. Taken using 455 nm LED excitation, with a 550 nm longpass filter (LPF), 2 s integration, 180 acquisitions, room temperature (R.T.)

fit. The peak shown has a line-width of 0.50 nm, resulting in a Q-factor of 1395 ± 77.

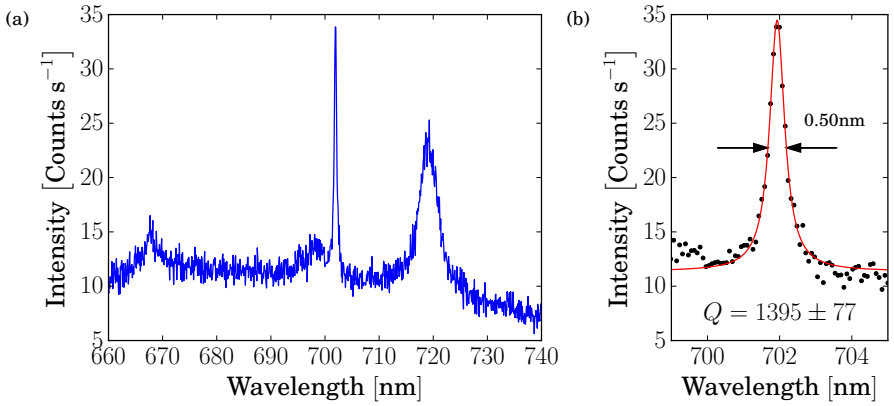

Figure 6.7: (a) PL spectrum showing an L3 cavity resonance. (b) Peak at 701.9 nm (symbols) with Lorentz fit (red line), peak width and Q-factor indicated. Spectrogram taken at 30 s integration time.

The overall trend of Q-factor upon variation of the device parameters is shown in Figure 6.8, with the current record performance of a Si_3N_4 L3 cavity for visible light indicated [202]. The sharp changes in Q-factor with the small 10 nm changes in a, or the $\sim$ 4 nm changes in r, demonstrate how sensitive these kinds of device are to modification of device parameters. The maximum Q-factor of 1395 ± 77 compares unfavourably to the simulated value of 4816. This is caused by fabrication defects altering the fabricated device to that of the simulation. However, this is similar to state-of-the-art values of $Q = 1460$ for similar devices [202].

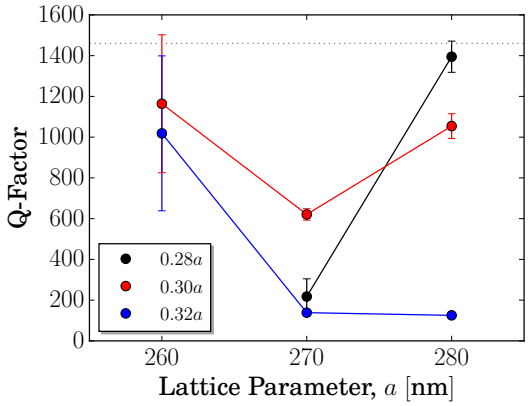

Figure 6.8: Q-factor with variation of: lattice parameter, a; and hole radius (different colours), r, expressed as a fraction of a. The grey dotted line indicates the highest reported performance of $Q = 1460$ as reported in [202].

6.5 Conclusions

The design, fabrication and characterization of L3 PhC cavities has been undertaken, with the aim of identifying if further improvements in performance can be achieved in the visible regime. Simulations indicated that a maximum Q-factor of 4816 was possible, only marginally higher than previous reports (~ 4700), therefore any substantial increase in performance would have to come from reduced fabrication imperfections; achieved by engineering-out sources of fabrication imperfections. The maximum Q-factor attained was 1395 ± 77, not significantly different to the current record performance of 1460 [202]. Furthermore, the devices show sensitivity to small changes in critical parameters: a 4 nm change in hole radius can cause a drop of $\Delta Q \approx 800$; and a 10 nm change in lattice parameter causes a drop of $\Delta Q = 1200$. This shows that highly engineered PhC devices are vulnerable to small changes in key parameters. This is further evidenced by the fact that with the L3 cavities shown, the ratio of experiment to simulation Q-factor is low: 0.29 (the ratio for the current record Q-factor is 0.31 [202]).

Other geometries such as 1-dimensional (1D) photonic crystal nanobeams have demonstrated higher Q-factors in the visible regime: $Q \sim 6000$ at 671.4 nm [213]; $Q \approx 55,000$ at 623.7 nm [214]; and $Q \approx 5400$ at 599.5 nm [215]. Such 1D nanobeams provide generally higher light confinement as they are less sensitive to fabrication imperfections, as the PhC only confines light in one axis. However, nanobeams are difficult to couple emitters to, due to decreased device area. Microdisc cavities have also been able to achieve higher quality light confinement: $Q \approx 46,000$ at 636.7 nm [216]; and $Q \approx 3,400,000$ at 654.1 nm [217]. These devices exhibit many resonances, multiple orders of the whispering gallery mode of the disc. To reduce light loss at the edges of the device, they must be fairly large ($\sim 20\,\mu$m diameter), this causes the mode volumes to be high ($\approx 700\left(\frac{n}{\lambda}\right)^3$) compared to photonic crystal devices ($\approx 2\left(\frac{n}{\lambda}\right)^3$), this decreases the Purcell enhancement. Also the modes are relatively inaccessible without the use of tapered fibres [76].

Ultimately 2D PhC devices in the visible appear to be limited by their sensitivity to imperfections such as: irregularity of hole circularity, side-wall roughness and verticality of the etch. The performance in the visible is unable to be bettered after a decade of improved nano-fabrication techniques, whereas devices in the telecoms band has improved [204]. This creates an obstacle that must be overcome: in order to access new applications and physics by using a range of light sources that emit in the visible light regime, good light-matter coupling is desired, however the most promising technology appears to have run out of steam and has plateaued; a new approach is needed.

Chapter 7

Disorder Induced Anderson Localization

> Very few believed [localization] at the time, and even fewer saw its importance; among those who failed to fully understand it at first was certainly its author.
>
> Philip W. Anderson
> *Nobel Lecture (8^{th} December 1977)*

DISORDERED photonic crystal devices utilize multiple scattering events to confine light in cavity-like modes. In this chapter, photonic crystal (PhC) waveguides are fabricated with induced disorder. Anderson localization is shown in the visible, in a nanophotonic chip, and the modes are imaged directly for the first time. The modes are spectrally characterized, and compared to state-of-the-art engineered devices. A device utilizing Anderson localization for light confinement is shown, for the first time, to exceed the performance of a highly-engineered equivalent. Initial investigations into the disordered waveguides were carried out by Henry Nelson [218]. Tom Crane performed the simulations of the photonic crystal, imaged the devices, took spectral measurements and performed analysis [219] . My contribution was to fabricate the devices, help with the analysis, make additional spectral measurements (including finding the 9330 Q resonance) and make additional analysis, and performing the intensity analysis. The work in this chapter was published as [125].

7.1 Disordered Photonic Devices

Disordered photonic devices utilize disorder in order to trap light using multiple scatterings (as shown in Figure 7.1). A macroscopic example of this is if milk is added to water: the light entering the water now undergoes multiple scatterings due to the added milk, although this effect is not strong enough to confine the light locally. By using a photonic crystal, a device can operate in the slow light

regime where light propagation is more sensitive to disorder [220]. Disorder can be added in a number of different ways: by displacing holes randomly [221, 222]; by using misshapen holes [223]; by changing lattice constant [224]; and by relying on intrinsic fabrication imperfections [225]. If light can be scattered multiple times, in a manner akin to a cavity; what happens when the light is scattered many times, do cavities form?

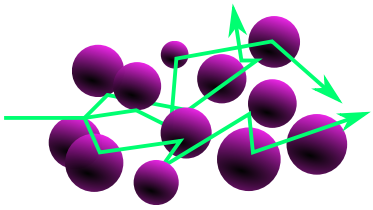

Figure 7.1: Representation of multiple scattering of light (green arrow) scattering off of particles (purple).

7.2 What is Anderson Localization?

Anderson localization was originally developed to explain the behaviour of electrons as they propagate through semiconductors with impurities [226][1]. The classical Drude theory linked conductivity of a material to the mean-free-path of the electrons, the average distance they were able to travel between collisions with the lattice. For materials such as semiconductors, the mean-free path of electrons was theorised to decrease as disorder of lattice through which they propagated increased (by the addition of impurities or dopants). However, it was observed that after a critical degree of disorder was applied, this ballistic propagation came to a stop and the electrons became localized [227].

By reinterpreting the localization as multiple scatterings instead of quantum tunnelling, it was predicted that localized states would exist near the band edges of a photonic crystal [228], this allowed photonic crystals to be used to probe Anderson localization. Furthermore, slow light propagation in PhCs interacts with disorder resulting in multiple scatterings of light near the band edge [229]. The added benefit of moving to optical systems, was that photons do not interact with each other, unlike electrons. In a perfect transmission medium, light would propagate ballistically; once defects are introduced, the mean-free-path decreases. Once this reaches the order of the wavelength of the light, the light becomes a standing wave, and becomes stuck in a small cavity [230].

Ballistic propagation comes to a stop and the waves are fully localized when the localization length (ξ) is shorter than the sample size. Localized waves propagate without any diffusion, and instead exhibit an exponentially decaying field profile:

$$I \propto e^{\frac{-r}{\xi}} \tag{7.1}$$

[1]The original paper is cited as it was the nexus of the field; however this is usually as an "unrecognisable monster" as Anderson described in 1983. This is the manner in which I do so now.

The intensity of the localized mode, I, decays exponentially with distance from the mode centre, r [231]. This forms one of the major experimental proofs of Anderson localization – observing modes with an exponential decay. However, the losses within a system will also manifest as exponential decays of the propagating wave, making identification of Anderson localization experimentally difficult.

The transition between the ballistic propagation regime and localization is dictated by the relative values of: sample size L, the mean-free-path between scattering events l, and the localization length ξ (the length beyond which diffusive transport cannot occur). The sample size refers to the physical size of the medium in which the scattering is occurring. The different regimes of propagation are:

$$\begin{aligned} L \ll l, \xi &\qquad \text{Ballistic Propagation} \\ l \ll L \ll \xi &\qquad \text{Diffusive Propagation} \\ l, \xi \ll L &\qquad \text{Localization} \end{aligned}$$

If the mean-free-path between scattering events is longer than the sample length, then the waves propagate ballistically. If the mean-free-path is shorter than the sample length, multiple scatterings can take place, causing diffusive propagation.

Anderson localization is a wave phenomenon that can be observed in any wave-like system [227]: electron propagation [232], acoustic waves [233], Bose-Einstein condensates (BECs) [234], microwaves [235] and optical waves [236]. 1-dimensional (1D) localization dependent on the dimensionality of the system (ξ is shorter) – if it is sufficiently large ($\xi \ll L$) then Localization should occur.

The length requirement means that in order to observe Anderson localization, a long sample size (or device length) is needed. Waveguides are devices which can guide electromagnetic wave propagation, and typically have long device lengths. Photonic crystals provide the ability to tune the waveguide, a means to introduce disorder and can access the slow light regime. These will trap a stream of guided light, along which disorder can be introduced. Devices with $Q \approx 150,000$ have been demonstrated in the telecom C band at $\sim 1.5\,\mu\text{m}$ [223]; where disorder was introduced by using pentagonal air hole, where the pentagons of some holes were rotated. At the telecom wavelength, these devices do not match the performance of engineered devices: $Q \approx 9,000,000$ at $1.57\,\mu\text{m}$ [204]. Waveguides at the shorter near-infra-red have shown $Q \approx 30,000$ at $\sim 940\,\text{nm}$ [137]. Disordered PhC waveguides, where disorder is achieved by randomly displacing the air holes from the perfectly periodic lattice, have shown $Q \approx 10,000$ at $\sim 975\,\text{nm}$ [221].

As Anderson localization uses disorder as a resource for light confinement, instead of acting as a obstacle (as with highly engineered devices), this may provide a route to achieving high-quality photonic cavities in the visible light regime.

7.3 Design of Photonic Crystal Waveguides

PhC waveguide devices were designed using finite-difference time-domain (FDTD) simulations. Firstly a waveguide within a perfectly periodic photonic crystal was designed. The process for this was to place a dipole emitter with a Gaussian

emission profile at one end of a waveguide channel (at $x = 0.1\mu m$). A Gaussian profile was chosen as it is a good approximation of the silicon nitride (Si_3N_4) photoluminescence (PL) spectrum (as shown in Figure 6.6a, $\lambda \approx 650\,nm$), and the Si_3N_4 PL originates from defects interacting with a thermal bath. A field monitor was placed 4.7 µm away from the source, along the waveguide. The PhC parameters (lattice parameter, a; and hole radius, r) were tweaked to optimize the electric field flux that passed through the monitor – this was analogous to the amount of light guided along the waveguide channel. Optimal parameters were found to be $a = 310\,nm$, $r = 0.35a$, with a total waveguide length of 100 µm. This large value of L was chosen to place the device into the Anderson localized regime. A plot of a simulation of the light guiding is shown in Figure 7.2.

Disorder was introduced to the perfectly periodic PhC structure by perturbing the locations of the holes in the three rows above and below the waveguide channel. Each hole was displaced from its correct position be randomly selecting an angle (to provide displacement direction), and a distance. The distance was randomly selected from a Gaussian distribution with an adjustable standard deviation. The standard deviation was expressed as a percentage of the lattice parameter a. These disorders were not optimized through simulation, as it was expected that small fabrication defects would dominate device performance so fine-tuning of the devices would be futile. A simulation of a device with 5% disorder is shown in Figure 7.2, the guided mode can be seen to zig-zag across the waveguide channel.

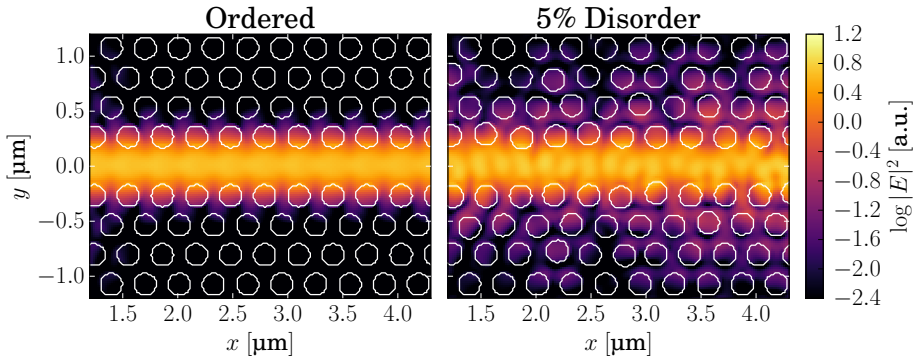

Figure 7.2: FDTD simulations of PhC waveguides with: (a) no intentional disorder; (b) with the three rows of holes above and below the waveguide channel displaced from the perfectly periodic structure by a 5% disorder.

The band-structure of the PhC waveguides was calculated using a Bloch mode expansion (BME) technique [237]. In this technique, the eigenmodes of a perfectly periodic photonic crystal are described using the magnetic **H** field and the dielectric structure of the photonic crystal. By expanding the modes into a summation, a set of linear equations for the magnetic field are produced. From these solutions the electric field can be computed, hence the modes of the photonic crystal can be simulated. The band-structure is shown in Figure 7.3 in wavelength-space, with plots of the modes. The region above the light-line to the right of the plot is the allowed region. The simulations indicate that two guided modes can propagate along the waveguide, at the visible and near infra-red boundary.

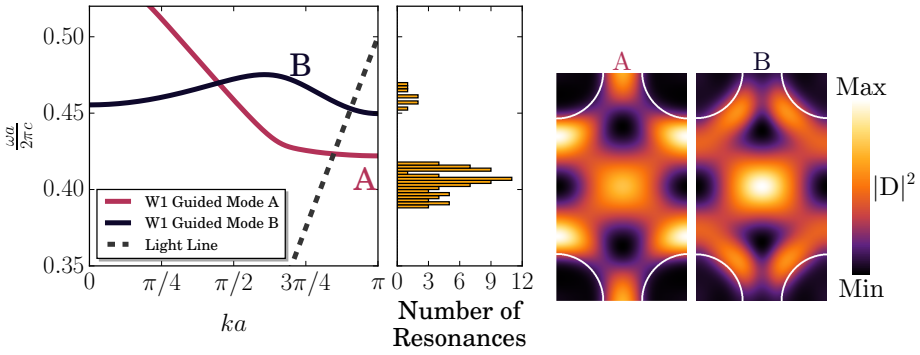

Figure 7.3: Left panel: Calculations of photonic band structure for guided modes with a perfectly periodic lattice. Where, ω is the photon frequency, a is the lattice constant, c is the speed of light in a vacuum. Centre panel: Experimentally measured modes in waveguides with 0% disorder, as a function of energy. Right panel: Calculated profiles of the mode intensity of the two modes at the edge of the Brillouin zone (as shown in left); where $\mathbf{D}$ is the electric displacement field ($\mathbf{D} = \varepsilon\mathbf{E}$, where ε is the permittivity, and $\mathbf{E}$ is the electric field).

7.4 Fabrication of Waveguides

The waveguides were fabricated using the same process as described in section 6.3, with a 250 nm thick Si_3N_4 layer being deposited. A range of degrees of disorder were fabricated, from 0% to 10% in 1% steps. Figure 7.4[2] shows micrographs of finished devices: the disorder of the three rows adjacent to the waveguide channel can be seen in Figure 7.4c.

7.5 Photoluminescence Imaging

Using a 455 nm light emitting diode (LED) for wide-area excitation, the PL emission from the waveguides can be imaged directly: Figure 7.5 shows PL images for waveguides with increasing levels of disorder. The intrinsic Si_3N_4 PL acts as a homogeneous internal light source which can probe all modes of the waveguide. This is the first time such direct imaging of Anderson localization has been performed. This allows the direct observation in the far field of confined optical modes without the need to resort to raster scanning a laser spot [221], near-field scanning or cathodoluminescence. Prior to fabrication the location of the modes is unknown, however by using the positioning technique, their locations can be recovered from PL images.

In the images the waveguide channel is the bright emission feature along the centre, the photonic crystal region extends above and below to the extent of the image, the PL in this region is the intrinsic PL form the Si_3N_4 itself. Waveguides without any intentional disorder (perfectly periodic, so-called 0% devices) are observed to have a bright signal from the waveguide channel, without any hot-spots. Such hot-spots can be seen along the waveguides shown in Figure 7.5, becoming more prominent as disorder increases, with the 9% disorder exhibiting

[2]The anisotropic etch of the silicon can be seen as the inverted pyramid under the marker above the device in Figure 7.4a.

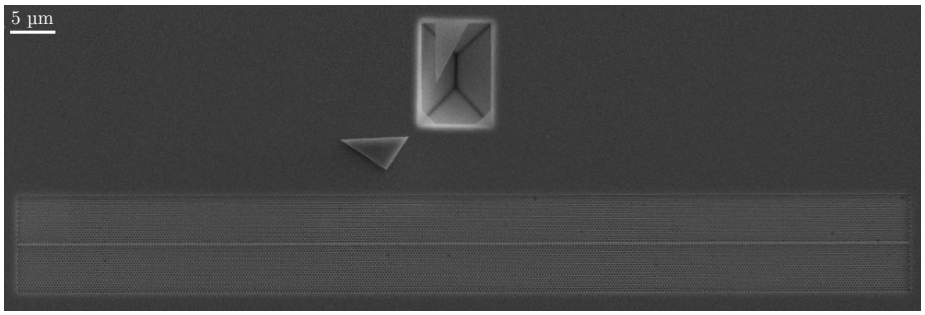

(a)

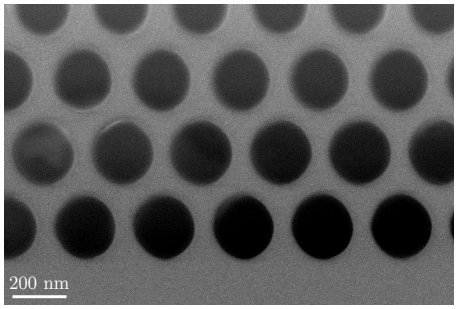

(b)

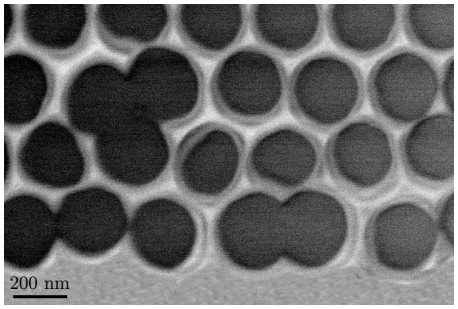

(c)

Figure 7.4: Scanning electron micrographs of: (a) wide-angle view of finished device (100 µm long), with label; (b) perfectly periodic photonic crystal beside waveguide channel (bottom); (c) three rows of holes with intentional positional disorder (10% disorder) beside waveguide channel.

the brightest. These areas of localized high-intensity are an indication of light confinement in an optical cavity.

By extracting line-cuts along the waveguide channel the far-field spatial extent of the cavities can be assessed, shown in the right panels in Figure 7.5. Gaussian fits of the line-cut data allow the exact locations and an upper limit of the cavity mode extent to be determined, within a few nanometre accuracy. This allows a key problem to be addressed: the random location of the light confinement. By imaging the locations of the modes, their exact locations can be identified, and emitters can be deterministically coupled to them. The distribution of spatial extents as a function of disorder is shown in Figure 7.6, the lowest disorders (0 and 1%) did not exhibit strong hot-spots that could be fitted. The spatial extent of all modes are below 1.2 µm – two orders of magnitude shorter than the device path length (100 µm) – consistent with localization.

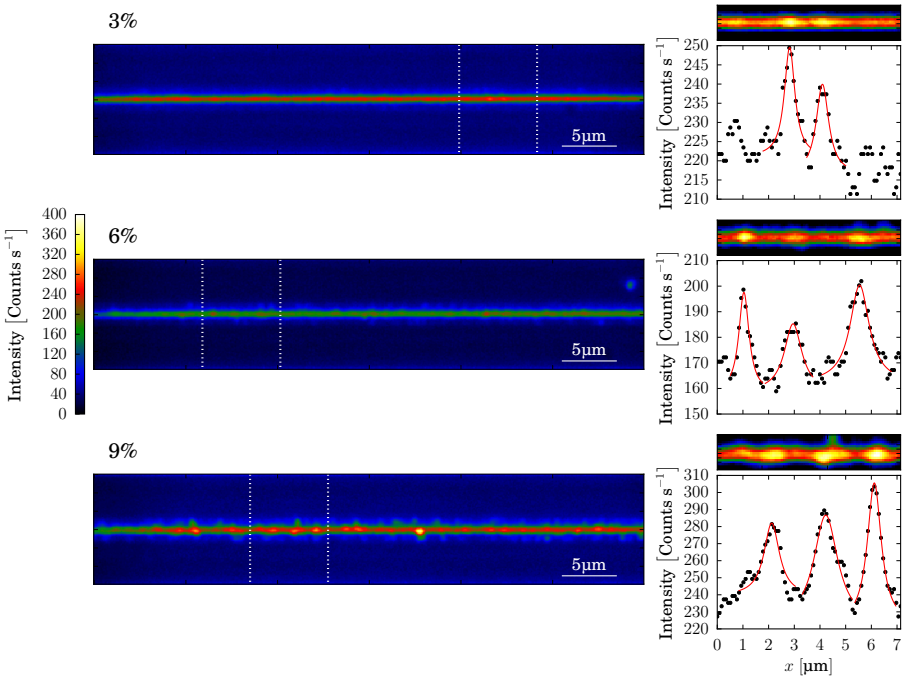

Figure 7.5: PL images of waveguides with different levels of intentional disorder (3, 6, and 9%), taken under 455 nm LED excitation. Left panels: Wide-area PL images of waveguide devices. Right: Line-cuts of regions indicated in left panels by dotted lines (black symbols) with Lorentz fits (red line). Small adjusted-contrast images of regions of interest are shown above the line-cuts, highlighting the locations of the modes.

7.6 Photoluminescence Spectra

7.6.1 Spectral Signatures of Localization

Once modes have been identified using the combined imaging and positioning technique, the spectral signatures need to be examined. The modes can be individually probed using an excitation laser (473 nm continuous wave (CW)), to

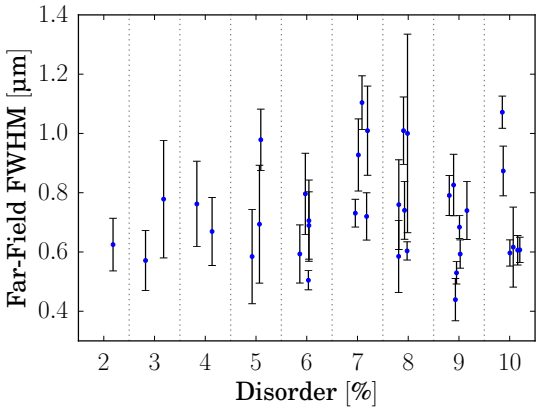

Figure 7.6: Far-field mode extent as a function of disorder, horizontally offset for clarity.

provide high-power spot-excitation. Figure 7.7 shows a typical spectrum of the Si_3N_4 which was used as a light-source to probe the cavities along the waveguide. A typical spectrum from a waveguide with no intentional disorder is also shown, it has multiple sharp and bright resonances above the modified Si_3N_4 continuum within the 2 µm-diameter laser spot. Such sharp resonances are a signature of high-quality light confinement, and appear close to the band edges shown in Figure 7.3. The result that resonances are observed with no intentional disorder proves that the intrinsic disorder introduced during the fabrication process is sufficient to cause light confinement. The spectral resonances change as the laser is moved across the 100 µm-long waveguide, with many tens of resonances visible along the full length.

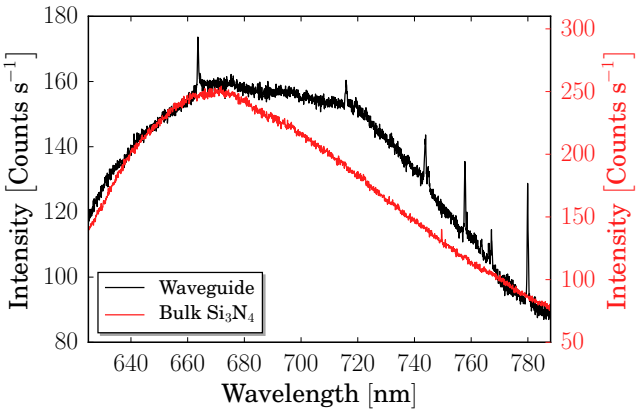

Figure 7.7: Spectra of: the Si_3N_4 bulk PL (red); and of a waveguide with no intentional disorder (black), with multiple resonances visible.

Line-widths are extracted from spectra (Figure 7.8) using Lorentz fits, with line-widths as narrow as 0.085 nm measured; using Equation 2.9, the quality-factor (Q-factor) can be calculated. The highest, as shown, is 9330($\pm$800). The dependence of the emission on the laser power density was examined: laser

power was varied and spectra recorded, Figure 7.9. The resonance blue shifts with increasing power, as the heating provided by the laser modifies the local refractive index. This also modifies the light-confinement of the cavity, changing the Q-factor. At the lowest of powers, the poor signal-to-noise-ratio leads to a lower extracted Q-factor.

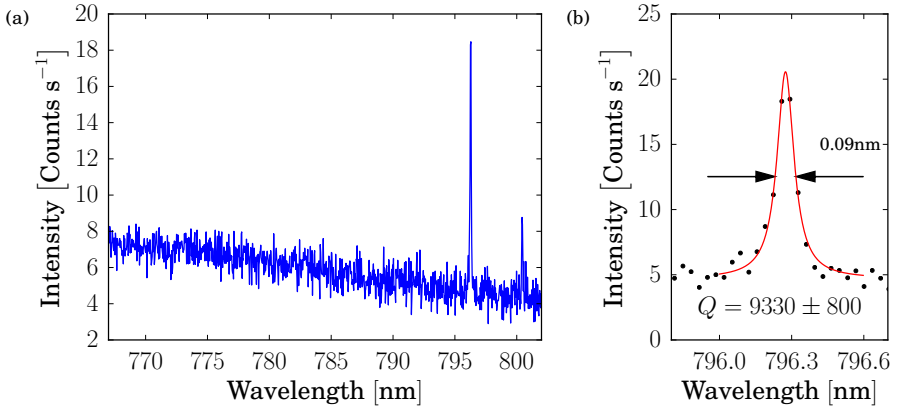

Figure 7.8: (a) Spectrum taken from a waveguide device with no intentional disorder, under 405 nm CW laser excitation, ad 3.78 nW/µm^{-2}. (b) Zoom-in of resonance (symbols), with Lorentz fit (red line). Line-width and calculated Q-factor indicated.

7.6.2 Statistics of Optical Resonances

Light confinement within optical cavities along the waveguides relies upon multiple scattering from imperfections; therefore a distribution of cavity Q-factors and wavelengths is expected. Light will be scattered along different paths for different cavities, causing variation in their confinement. The dependence of Q-factor on degree of disorder is shown in Figure 7.10a. Overall, Q-factors are measured between ~ 100 and $\sim 10,000$, with the mean Q-factor decreasing with increasing disorder. The grey bars indicate mean Q-factors from BME simulations for the different degrees of disorder, which agree well with the experimental data. Figure 7.10b shows the dramatic shift in the quality of light confinement as disorder is increased. The decrease in Q-factor, is caused by increased photon loss from the cavities. Light is confined to the crystal plane by total internal reflection, from the refractive index contrast between the Si_3N_4 and air. As disorder is increased, one can expect the probability that light may be scattered out of the plane increases, leading to increased losses from the cavities. This is why the cavities are more visible in the PL images (Figure 7.5) at higher disorders. This relationship is consistent with previous reports of Anderson localization [221], showing that the intrinsic disorder from the fabrication process is alone sufficient to create the highest quality cavities, and no other source of disorder is required.

The Q-factor of 9330 is the highest reported Q-factor of a 2-dimensional (2D) PhC device operating in the visible. Furthermore, this is also the first time that a device operating in the Anderson localized regime has exceeded the performance of an engineered device. If the ratio, $\frac{Q_{\mathrm{AL}}}{Q_{\mathrm{2D}}}$, between the highest reported Q-factor for an Anderson localized device and their highly-engineered counterpart

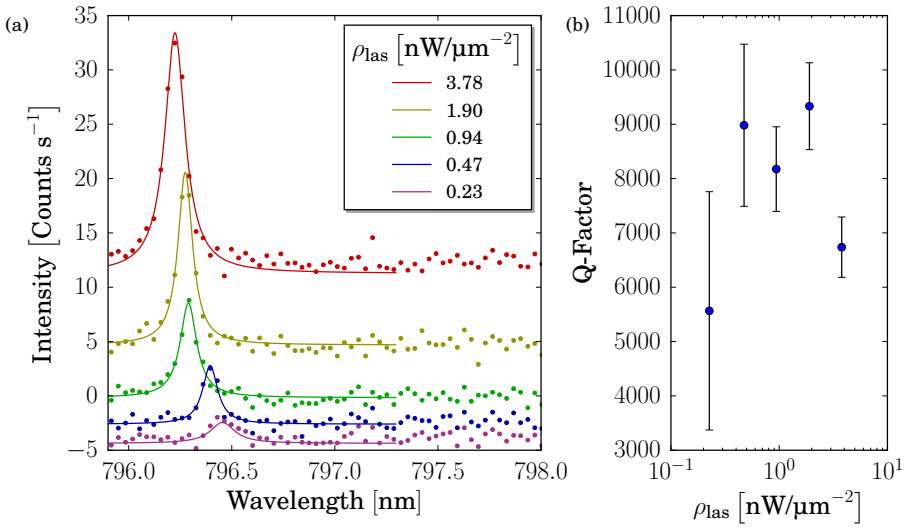

Figure 7.9: (a) Power resolved spectra for the resonance shown in Figure 7.8, where ρ_{las} is the laser power density. (b) Variation of calculated Q-factors, extracted from (a), with ρ_{las}.

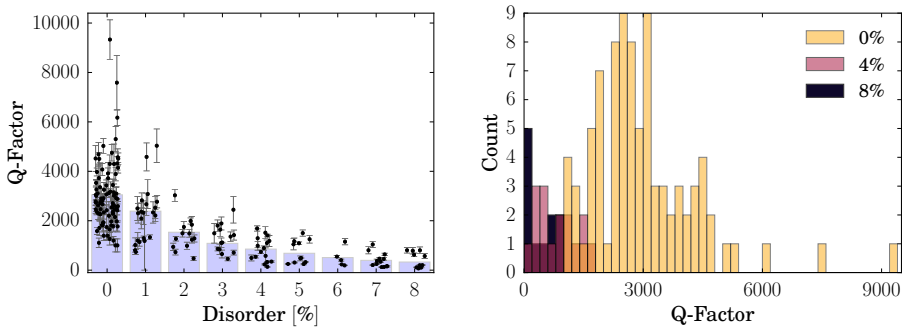

(a) (b)

Figure 7.10: (a) Statistics of cavity Q-factors as a function of disorder (symbols), errors calculated from fit parameter covariance, horizontally offset for clarity. Grey bars indicate mean values for each degree of disorder based on BME simulations. (b) Histograms of the number of resonances identified as a function of Q-factor, for three different degrees of disorder (0%, cream; 4%, pink; and 8%, purple).

(shown in Table 7.1) is considered; it shows that Anderson localized devices have trailed behind the performance of highly engineered devices. However as the wavelength of operation shortens, this ratio shifts towards the Anderson localized devices. As device features become smaller (to operate at the short wavelengths required for visible light), unavoidable fabrication defects begin to affect device performance and their ability to confine light. In the visible, where this effect is most pronounced, disordered devices (where these imperfections are a resource instead of an nuisance) are able to exceed the performance of engineered devices. This is an important result, as it provides a route to high quality cavities in the otherwise inaccessible visible-light regime.

Wavelength	Material	Q_{2D}		Q_{AL}		$\frac{Q_{AL}}{Q_{2D}}$
Telecom C Band	Si	$9,000,000$	[204]	$150,000$	[223]	0.02
NIR ($\sim 900\,\text{nm}$)	GaAs	$30,000$	[137]	$10,000$	[221]	0.33
Visible	Si_3N_4	$3,400$	[224]	$9,330$		2.74

Table 7.1: Record Q-factors for 2D engineered PhC devices (Q_{2D}) and Anderson localized devices (Q_{AL}) for a range of wavelength regimes.

BME simulations were undertaken to calculate mode volume. In fact, this is the only way of assessing the mode volume of the cavities in these waveguides without resorting to near-field scanning techniques. Typical approaches measure the lifetime modification by Purcell enhancement as an emitter interacts with the cavity, but with these devices there are no single photon emitters; the bulk Si_3N_4 PL is used, which is most definitely not a quantum light source [207]. Figure 7.11 shows distributions of simulated mode volumes: the mode volumes are all below $4\left(\frac{\lambda}{n}\right)^3$, where λ is wavelength of the cavity resonance, and n is the refractive index of the membrane[3], giving $V \lesssim 0.2\,\mu\text{m}^3$. This is larger than the limit of $\frac{1}{4}\left(\frac{\lambda}{n}\right)^3$ for the smallest photonic crystal cavity [239]; or $\sim 0.1\left(\frac{\lambda}{n}\right)^3$ for the smallest micropillars [240]. However it is smaller reported mode volumes of $\sim 1\,\mu\text{m}^3$ for Anderson localized modes in the near infra-red at $\sim 900\,\text{nm}$.

7.6.3 Anderson Localization

The most concrete proof of Anderson localization is to observe an exponential decay of intensity with length. This poses a number of experimental difficulties, as many losses are also manifested as exponential decays. To provide a more experimentally robust criterion, examination of the sharp peaks in the emission spectrum is used [235][4]. Intensity spectra from systems with Anderson localization will have multiple, sharp, high-intensity peaks (relative to the background). Therefore, by calculating the variance (spread of intensities relative to the mean intensity) of the normalized intensity (normalized to the mean intensity), the localization can be quantified, whilst ignoring any losses from

[3] $\lambda \approx 750\,\text{nm}$, $n_{Si_3N_4} \approx 2$ [238], so $V \lesssim 0.2\,\mu\text{m}^3$.

[4] Clearly, any spectrum with sharp peaks cannot be used, otherwise the L3 cavity devices in chapter 6 could be declared to be Anderson localized! Instead only spectra from devices where every other type of cavity or resonator has been ruled out, such as the waveguides, should be examined this way.

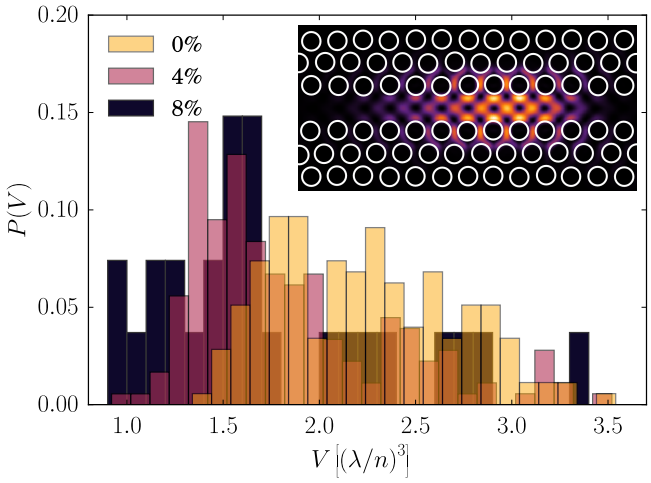

Figure 7.11: Simulated mode volumes for selected degrees of disorder (0%, cream; 4%, pink; 8%, purple). Volume expressed in units of $\left(\frac{\lambda}{n}\right)^3$, where λ is wavelength of the cavity resonance, and n is the refractive index of the membrane. Inset: Example electric field profile for a cavity mode for a waveguide with 0% disorder.

the system. A spectrogram is first normalized to the mean intensity, then a histogram prepared. In the case of the spectrogram shown in Figure 7.7, the Si_3N_4 continuum was subtracted prior to normalization. The final intensity plot is shown as Figure 7.12. For non-Anderson localized light, there would be little-to-no tail at high $\frac{I}{\langle I \rangle}$. If Anderson localization is present, there should be a long monotonic tail, with some high very high intensity points, as is shown in Figure 7.12. The variance of the distribution shown is 3.3, which is comfortably above the minimum criterion of $\frac{7}{3}$ [221, 235].

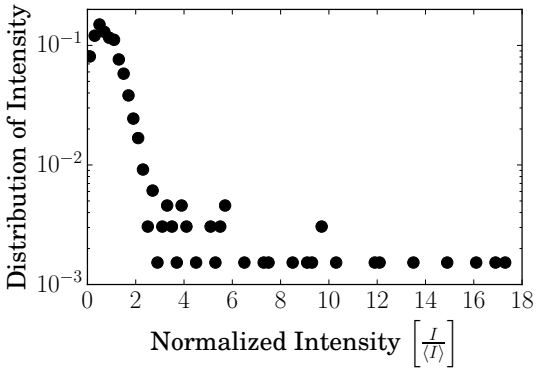

Figure 7.12: Normalized spectrum intensity plot.

7.7 Conclusions

Photonic crystal waveguides have been designed, fabricated, and characterized with the aim of demonstrating Anderson localization. Anderson localization has been demonstrated for the first time in the visible on a nano-photonic chip.

Using the imaging set-up, the first direct imaging of Anderson-localized modes has been performed, opposed to re-constructive techniques such as laser scanning, near-field scanning techniques or cathodoluminescence. From these images the position and spatial extent of modes can be determined. This provides a means to mitigate the lack of control of position of the cavities, which spontaneously form along the waveguide channel; they can be mapped post-fabrication, with nanometre accuracy. The far-field spatial extent provided hinted that Anderson localization may be present, by placing an upper limit on mode size – far below that of the device length.

Spectral characterization revealed multiple sharp cavity resonances within single spectrograms, a signature of light confinement. Q-factors up to ∼10,000 have been observed, which for the first time exceed those of comparable highly engineered 2D photonic crystal cavities (chapter 6) and heterostructure cavities [224], and are a record for a 2D PhC in the visible. The final clinching proof of Anderson localization was provided by examining the intensity distributions of spectra, assessing the intensity distribution of the resonances.

Cavities for high-quality confinement of visible light are important resources with a broad array of applications able to benefit: energy harvesting, imaging, sensing. Applications in fundamental research into the light-matter interaction can also benefit, for instance: random lasers [241], and cavity quantum electrodynamics (QED) experiments using visible light emitters such as colloidal quantum dots (QDs) [111], 2D materials [88] or diamond nitrogen-vacancy (NV) centres [77]. NV centres are of particular interest as these emitters can work at room temperature and have good spin-coherence [242]. Monolithic devices in diamond are difficult to fabricate, so a device incorporating NV centre-containing nano-diamonds is attractive.

Many modes appear along a single waveguide device, making these devices attractive for sensing, multiple sites can be measured with a single device. Photonic crystal based sensors have had limited use, due to scalability issues; issues which disordered devices are able to overcome. Additionally spatial overlap between the many modes along the waveguide may provide a network to convey quantum light between sites [29], using coupled Anderson localized modes, known as necklace states [243]; these would allow quantum light propagation with Purcell enhanced emission of light in cavities, therefore improved coherence.

Chapter 8

Sensing with Anderson Localized Light

"How do you know that anything else exists?"
"My sensory apparatus reveals it to me."

Lt. Doolittle talking to Bomb №20
Dark Star (1974)

Optical sensors are able to detect changes in target parameters (refractive index, temperature, strain) using an all-optical readout system. Here the use of the sharp resonances which spontaneously form along a photonic crystal (PhC) waveguide channel, arising from Anderson localization, are used for sensing. The sharpness of the resonances provides a high resolution for contaminant and temperature sensing. This work used the waveguides fabricated in chapter 7: Tom Crane performed the contaminant sensing experiment; summer students Hector Stanyer and John Nevin provided help during the temperature measurements; I performed the simulations to retrieve the refractive index, made additional analysis, and made the temperature sensing measurements. The work in this chapter was published as [244].

8.1 Optical Sensors

Optical sensing is an established field based on transmission, reflection and absorption spectroscopy. Such sensors can be used in environments with electrical noise, combustible gasses or where readout throughout a chemical process is needed.

Photonic crystals provide a mechanism to control light confinement, and are highly sensitive to modification of the refractive index contrast [118]. This makes them ideal sensors, as the presence of a contaminant can alter the device by locally modifying the refractive index contrast between the crystal and air. A cavity resonance would, when subjected to this change, shift in wavelength; due

to modification of the photonic crystal bandgap. Sharp, high-quality, cavity resonances are key to the high performance of these devices; maximizing the resolution of the device to any change in environment [245].

Such PhC based sensors already surpass plasmonic based sensors, which can have resonances as broad as 100 nm with simple patterned substrates [246]; alternatively more-complex cup structures have been reported with line-widths of $\sim$ 3 nm and sensitivities of $\frac{\Delta\lambda}{\Delta n} \approx 714\,\text{nm/RIU}$ (RIU $\equiv$ Refractive Index Unit) [247]. Ring-shaped plasmonic absorbers have been developed for the mid infra-red for bio-medical sensing [248]. PhCs are able to provide much sharper resonances than plasmonic devices, at the expense of decreased scalability of fabrication. Current record performance in a PhC platform is reported as: $Q \approx 7,500$ with a sensitivity $\frac{\Delta\lambda}{\Delta n} \approx 370\,\text{nm/RIU}$ at 1.57 µm [249]; $Q \approx 50,000$ with a sensitivity $\frac{\Delta\lambda}{\Delta n} \approx 1,500\,\text{nm/RIU}$ at 1.58 µm [250].

The main obstacle to widespread adoption of a PhC-based sensing platform is the effort required to optimize the fabrication process to reduce fabrication imperfections. As demonstrated in chapter 6, PhCs devices are sensitive to small changes in the critical parameters: hole sizes can vary between 1-4 nm between devices [251], requiring expensive and time-consuming tuning of devices through multiple rounds of fabrication. furthermore, as shown in chapter 7, unavoidable fabrication defects will occur, which cannot be engineered around. This has limited the performance and scalability of PhC devices for most applications. Devices exploiting Anderson localization, which confine light via multiple scattering, have sharp resonances which are disorder robust: this offers a means to overcome the challenge of scalability, and level of engineering, required to exploit PhC sensors.

PhCs cavities have strong field confinement and high quality-factors (Q-factors), causing the resonant wavelength to be highly sensitive to changes in refractive index contrast: allowing the development of refractive index sensors. Most work has been centred in the infra-red, where high-quality cavities are routinely fabricated. The first demonstration was in 2004 with a device at 1.5 µm and $Q \approx 400$ [252]. Other devices have followed in the infra-red: $Q = 438$ at 1.486 µm and $Q = 2742$ at 1.488 µm in 2008 [253]; and 50,000 in 2009 at 1.56um [250]. A device for sensing in the visible is based on a 1-dimensional (1D) silicon nitride (Si_3N_4) cantilever, a 1 µm wide membrane, with a 1D PhC region $\sim$ 10 µm long. It is able to achieve $Q \approx 1700$ and perform sensing at $\sim$ 700 nm [254]. This device is also highly engineered: with great sensitivity to modification of hole size and spacing. As will be shown, Anderson localized resonances are already competitive with resonances from these high-engineered PhC devices.

8.2 Contaminant Sensing

The sensitivity of the PhC waveguide devices in chapter 7 to the presence of a small amount of contaminant was tested. A suitable position along a waveguide was found: where several cavity resonances were visible in the emission spectrum, under 473 nm continuous wave (CW) laser excitation power density of $28\,\text{kW cm}^{-2}$. A small quantity of isopropyl alcohol (IPA) (refractive index of 1.38) was deposited over the device using a micro-pipette. The resultant quantity of IPA within the excitation spot of the laser was estimated to be 20 pℓ on

the waveguide area of 1,000 µm^3; estimated from volume of IPA applied and the area of the waveguide region. The experiment was conducted at atmospheric pressure and at room temperature.

Figure 8.1 shows the time evolution of the emission spectra for the waveguide, with Figure 8.2 showing a zoomed-in section of the bright resonance. The IPA was applied at time $t = 0$, causing the resonances to red-shift markedly: up to 15.2 nm at 40 s (second resonance from right, 764.7 nm to 779.5 nm). Figure 8.3 shows selected extracts from Figure 8.1 for two resonances. At $t = 40$ s after the IPA application, the resonance initially at 775.9 nm (panel (a)) shifts by 12.6 nm: $\sim \times 30$ the line-width of 0.4 nm. Whereas the resonance initially at 764.7 nm (panel (b)) shifts by 15.2 nm: a $\sim \times 100$ the line-width of 0.15 nm. The difference in shifts are due to the two resonances relying on different multiple scattering paths in the waveguide to form cavities, different pathways which are affected differently by the modification in refractive index. This proves that the device provides a high level of sensitivity to contaminants, exceeding the performance of state-of-the-art devices using PhCs [252]; where a peak of line-width 3-4 nm shifts up to 90nm for a change in refractive index of $n = 1 \rightarrow 1.5$, shifting $\sim \times 30$ its line-width. It should be noted that the width of the resonances soon after the IPA deposition are larger than those $t > 400$ s. This is due to the resonance shifting wavelength relatively quickly, smearing the resonance over the spectrometer charge coupled device (CCD) during the 10 s integration time.

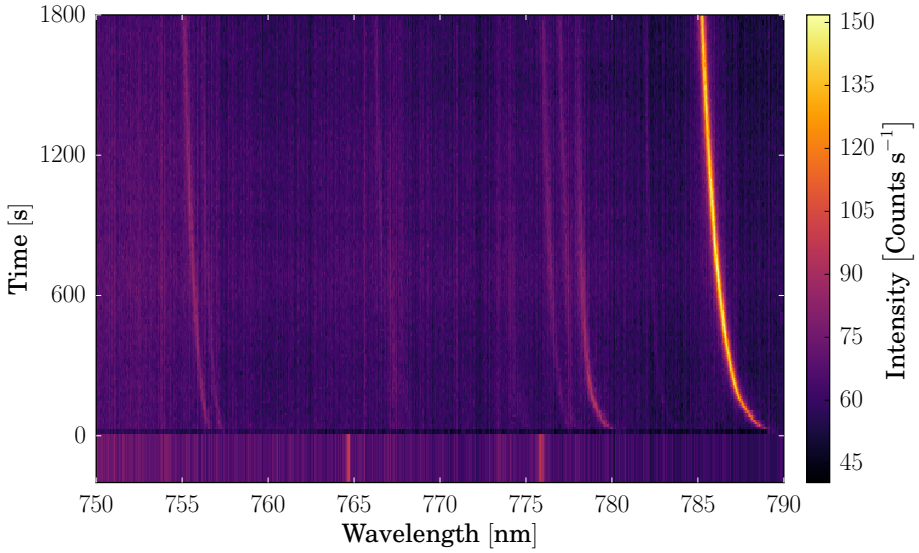

Figure 8.1: Photoluminescence (PL) spectra from a waveguide as a function of time, under 28 kW cm^{-2} 473 nm CW laser excitation at room temperature, showing wavelength tuning. IPA was applied to the device at $t = 0$, causing the resonances to red-shift, the spectrum taken before application is stretched to earlier times to aid visibility. The resonances gradually return to their original wavelengths as the IPA evaporates.

As time evolves the resonances migrate towards the original wavelength, due to evaporation of the highly volatile IPA from the surface of the device. To understand the dynamics of the shift, the evaporation was fitted using exponential

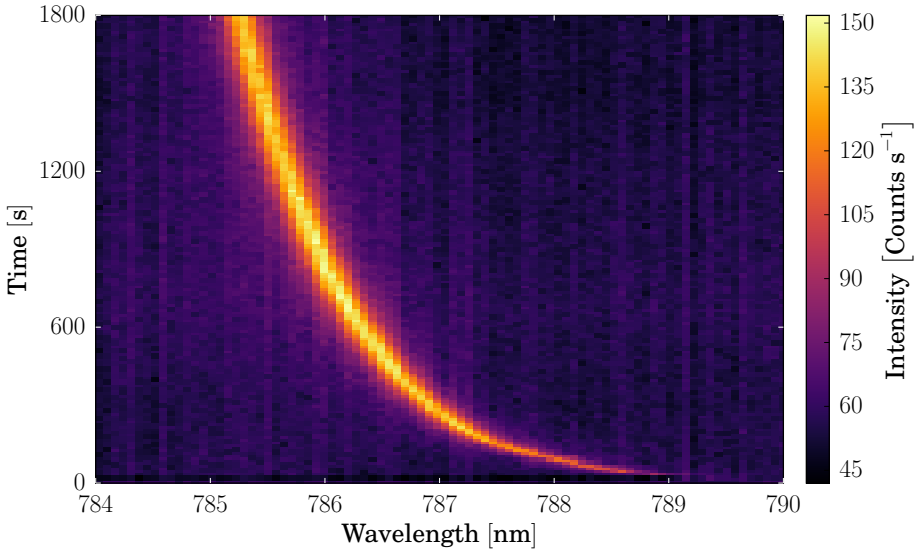

Figure 8.2: Zoom-in on the brightest resonance in Figure 8.1, showing time evolution of the wavelength shift as the IPA evaporates.

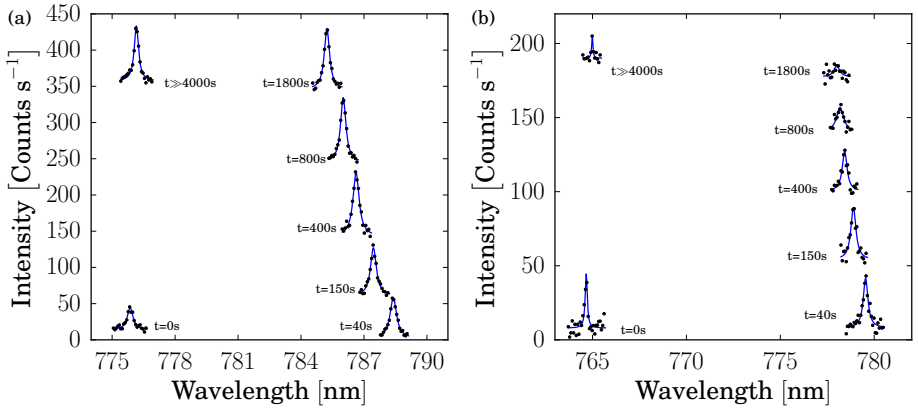

Figure 8.3: Example spectra (symbols) extracted from Figure 8.1, and their Lorentz fits (blue lines), for resonances at (before IPA application): (a) 775.9 nm (brightest) and (b) 764.7 nm (largest shift). Spectra vertically offset for clarity.

decays. The shift can be described by a double exponential fit (Figure 8.4a, showing the resonance initially at 775.9 nm):

$$\lambda = 775.9 + 1.7e^{\frac{92.3-t}{222.1}} + 10.5e^{\frac{92.3-t}{16075.5}} \tag{8.1}$$

An explanation for the dependence on two exponentials, is differing rates of evaporation of the IPA from the top surface of the membrane and from within the holes. By extrapolating the exponential fit over several hours, Figure 8.4b, the eventual return of the resonance to the initial wavelength can be seen. This is corroborated experimentally by the points in Figure 8.3 at $t \gg 4000$ s, which were taken the following day: the spectra indicate that the resonances have almost completely returned to their initial wavelengths. This proves reversibility of the shift, a key property required for these devices to be useful sensors – they can be reused and would not exhibit strong hysteresis.

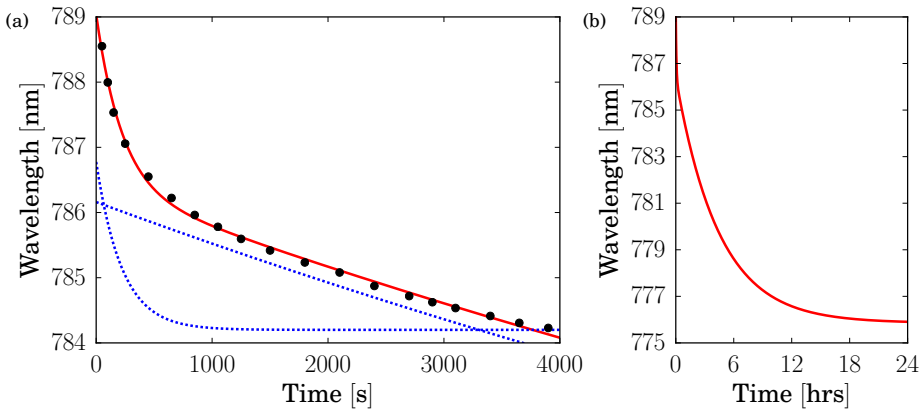

Figure 8.4: (a) Wavelengths of the optical resonance at 775.9 nm as a function of time, wavelengths extracted from Lorentz fits of spectra (symbols). Fitted with a double exponential (red), composed of two component exponentials (blue dashed) which are vertically offset for clarity. (b) Exponential fit plotted over a 24 hour period, showing the resonance returning back to its original wavelength.

Simulations were performed to recover the effective refractive index of the contaminant, providing a means of linking the wavelength shift of the resonances to a physical quantity. The simulations were performed using finite-difference time-domain (FDTD), with a waveguide with no introduced disorder. To simulate the IPA, the holes of the photonic crystal were filled with a material of variable refractive index: index which was varied from 1 (air filling) to 1.38 (fully IPA filled). The partial filling of the holes was modelled as an intermediate refractive index. This produced the relatively linear relationship shown in Figure 8.5a. The simulations were mapped onto the spectral information for the resonance initially at 775.9 nm, shown in Figure 8.5b. The changes in effective refractive index seem to indicate that the holes are not fully filled with IPA during the experiments: a potential ~ 30 nm shift could be possible if the sample were fully immersed.

Suitable calibration of this device would enable, not only verification of the presence of a chemical species, but also measurement of the quantity via refractive index change – as a percentage change from that of air.

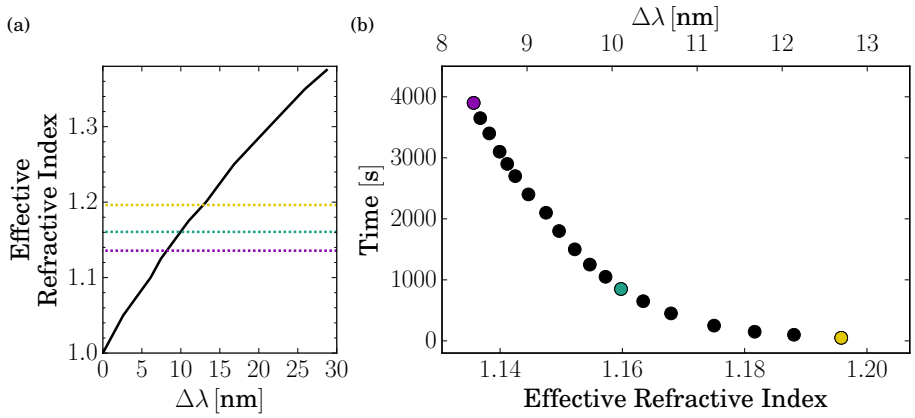

Figure 8.5: (a) Simulated resonance shift from central wavelength ($\Delta\lambda$) as the refractive index of the PhC hole filling material is changed. (b) Experimental shifts in resonance wavelength mapped to simulated refractive index change. Coloured points correspond to points marked in (a).

8.3 Temperature Sensing

The temperature response of the resonances was also studied. The waveguide chip was placed into a helium flow cryostat and cooled from 300 K to 10 K; PL spectra were taken at each 20 K step. As the temperature varies, the refractive index of the Si_3N_4 varies. Photonic crystals are sensitive to small changes in refractive index and to index contrast between the crystal membrane and the surrounding air, as demonstrated previously (section 8.2). Therefore as the temperature changes, the cavity resonances shift, Figure 8.6, with multiple resonances shifting in sympathy. A single resonance can shift by as much as ~ 2 nm (Figure 8.7a). This shift is fully reversible, and is able to provide a local temperature measurement from a device as the resonance is due to a cavity move with a maximum extent of 1.2 µm.

The temperature response behaviour can also be used to temperature-tune the optical modes into and out-of resonance with the emission from a range of quantum light sources such as: diamond defect-centres, 2-dimensional materials. This would be of use in cavity quantum electrodynamics (QED) experiments where resonant emitter-cavity coupling is required. As the device is cooled the resonances increase in Q-factor by a factor of ~ 2 (Figure 8.7b), this could be caused by a reduction in cavity losses at lower temperatures [255]; showing that by moving to cryogenic temperatures, the light-matter interaction could be enhanced further.

8.4 Conclusions

The use of Anderson localized modes within a waveguide for sensing has been demonstrated. Contaminant (IPA, $n = 1.38$) sensing has shown shifts of the cavity up to 100 times the resonance line-width, whilst proving to be fully reversible. Additionally, reversible temperature shifts up to ~ 2 nm have been observed when cooling from 300 K to 10 K. This shows that disorder-induced

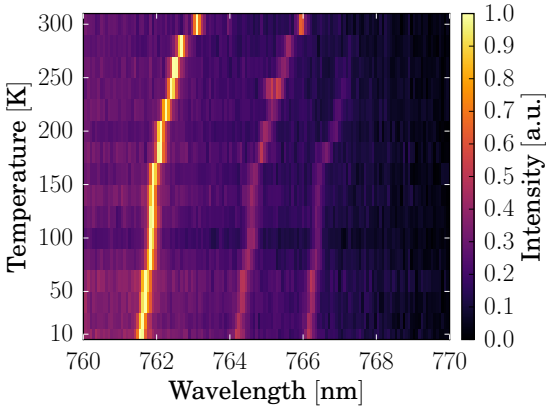

Figure 8.6: PL spectra from a waveguide device, under 405 nm CW laser excitation at 28 kW cm^{-2}, as a function of temperature (in 20 K intervals); showing multiple resonance peaks shifting with temperature. Normalization is applied to individual spectra. The increased background at shorter wavelengths is due to the Si_3N_4 PL.

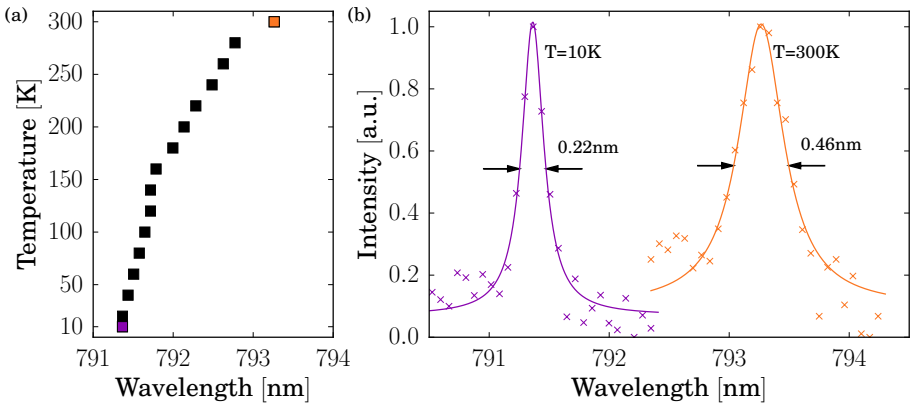

Figure 8.7: (a) Central wavelength of cavity resonance peaks, extracted from PL spectra, temperature varied in steps of 20 K. Error bars too small to be visible. (b) Normalized PL spectra collected at 10 K (purple symbols) and 300 K (orange symbols), with Lorentzian fits (lines). Full-width half-maximum (FWHM) are shown for both fits.

light-confinement in a Si_3N_4 chip is able to provide high sensitivity, room-temperature optical sensors. The narrow line-widths of 0.15 nm ($Q = 2742$) compare favourably to plasmonic devices ($\sim$ 100 nm [245]). No comparable 2-dimensional (2D) PhC devices exist in the visible [251]; although a 1D suspended device at $\sim$ 700 nm has shown $Q \approx 1700$ [254]. Overall PhC devices utilizing Anderson localization are able to operate in the visible light regime, with high quality resonances, providing higher sensitivity over traditional plasmonic devices.

Multiple high-quality resonances appear along a single waveguide device, allowing multiple sites to be probed simultaneously. The individual cavity modes can be identified using the imaging technique demonstrated in section 7.5, allowing sensing targets such as single molecules to be coupled to the resonances, potentially via the use of micro-fluidics [135].

The use of disorder means that they are able to side-step the limitations to scalability of conventionally engineered PhC-based sensors, as they dispense with the need for multiple iterations of fabrication to perfect the optimal device and fabrication parameters. The relaxed conditions for the fabrication of disordered devices means that alternative fabrication techniques such as nano-imprint [170] or deep ultra violet (UV) photo-lithography [256] could be used, removing the requirement of fabrication using slow and expensive electron beam lithography (EBL).

Chapter 9

Aperiodic Photonic Crystal Devices

> I have approximate knowledge of many things.
>
> Demon Cat
> *Adventure Time (2010)*

APERIODIC photonic crystals are structures where the hole positions are not regularly spaced, but use a mathematical progression to position the holes in a faux-random pattern. Devices with this pattern were fabricated and examined, they were found to confine light in the visible regime with quality-factors (Q-factors) similar to photonic crystal (PhC) cavities. These devices were designed and their performance simulated by Hossein Alizadeh and Ren Wang. I fabricated the devices, took measurements and have analysed the results. Connor Murray helped with measurements and analysis of the devices, with Chris White providing assistance during the measurements and analysis of the disordered devices. The work in this chapter will be published as [257].

9.1 What are Aperiodic Photonic Crystals?

Anderson localization is difficult to realize in 2-dimensional (2D) systems, due to an increased number of loss channels. This has launched a search for alternative systems that are able to confine light, so that high quality cavities and confinement can be realized. One such approach relies on aperiodic photonic crystals [258]. Aperiodicity is where something is not periodic, it is unevenly distributed, for example the distribution of prime numbers. In this case, aperiodicity represents a middle-ground between perfectly periodic PhCs and a fully-disordered one. Aperiodic structures can be deterministically generated based upon mathematical rules, which greatly simplifies the design of devices, as pseudo-random structures can be created repeatedly and deterministically, and improves scalability.

Perfectly periodic structures, crystals, have X-ray diffraction patterns with well defined peaks in a regular arrangement. It was realized that aperiodic

structures can also have these sharp diffraction peaks, and have long-range symmetry, not as a crystal but as a quasicrystal. The only regular polygons that can be tiled are $n = 3, 4, 6$ sided shapes. However, it was demonstrated that by using two shapes (the kite and the dart), an aperiodic structure can be tiled over an infinite plane, a technique called Penrose tiling [259]. Such a pattern has sharply-defined Bragg diffraction peaks, with rotational symmetry.

Aperiodic devices have been realized in systems with multiple dimensions of periodicity. 1-dimensional (1D) devices consist of dielectric stack gratings where layers are varied in thickness according to Fibonacci progression, these devices showed broad resonances of $\sim 20\,\text{nm}$ at $650\,\text{nm}$ [260]. 2D structures such as photonic quasi-crystal membranes based on Penrose tiling can be created with complete photonic bandgaps [261]; lasers using patterns visually similar to Hadamard transforms have been created, with line-widths $\approx 2\,\text{nm}$ [262]. 3-dimensional (3D) structures based on icosahedral packing can be fabricated using bottom-up techniques, and have also shown bandgaps. Initial work was made with metallic devices in the microwave regime [263], with recent work resulting in visible lasers at $\sim 590\,\text{nm}$ with $\sim 1\,\text{nm}$ line-widths [264].

The Vogel spiral is one such mathematically generated aperiodic structure [265]. They are evident in nature, governing the distribution of sunflower seeds and the structure of shells [266]. They have recently been used at the structure for photonic devices [258, 267, 268]. Vogel spirals are defined in polar space (r, θ) by:

$$r_n = a_0\sqrt{n} \tag{9.1}$$

$$\theta_n = n\alpha \tag{9.2}$$

where: $n = 1, 2, 3...$ is an integer index, a_0 is a scaling factor, α is the divergence angle. So-called golden angle Vogel spirals (GAVSs) can be created by setting α to the golden angle, α_G:

$$\alpha_\text{G} = \frac{360^\circ}{\varphi^2} \approx 137.508^\circ \tag{9.3}$$

where φ is the golden ratio:

$$\varphi = \frac{\left(1+\sqrt{5}\right)}{2} \approx 1.618 \tag{9.4}$$

In reality, φ is approximated by using the ratio of two adjacent Fibonacci numbers. Large variations in device structure can be achieved by modifying α, small changes of 0.3° are all that is necessary to completely change the local density of states (LDOS) and location of localized light in photonic GAVSs [267]. GAVSs result in isotropic photonic band-gaps [269] in reciprocal-space, which has made them of particularly attractive for photonic devices as they confine light in all directions. It has also been shown that Vogel spirals impart angular momentum to scattered light, creating polarization vortices [270].

The optical properties of the GAVSs are dictated by their LDOS, Figure 9.1. The LDOS was calculated at the centre of the structure using a Green's function finite-element method to calculate propagations of waves between pairs of points, as described in [267]. The LDOS is characterized by a large number of peaks on the high-energy band edge, which is where the photonic modes are to be expected. The spatial distribution of the modes was calculated, Figure 9.2:

the modes form in a ring around the centre of the spiral structure – the light is confined by multiple scattering in this region.

GAVS have been shown to have photonic bandgaps, which can be used to localize light [271]; with simulations showing light trapped in modes encircling the centre [267]. These have been realized as plasmonic devices, with metallic cylinders on substrates, where: they have been shown to provide modest $\approx \times 2$ emission enhancement at $\sim 600\,\text{nm}$ via the plasmon resonance [272]; the near-field has been mapped [273]; and their polarization and angular momentum dependence studied [270].

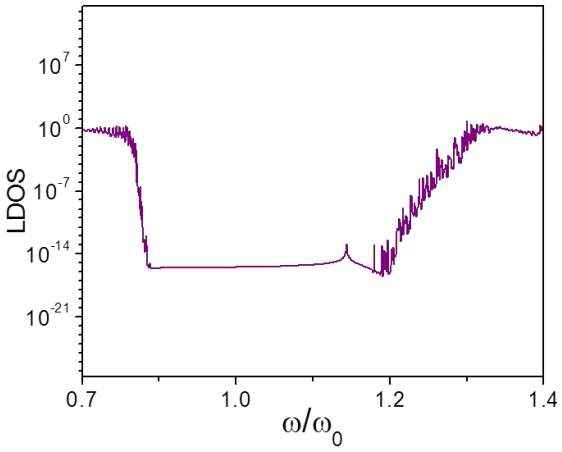

Figure 9.1: Simulation of the LDOS for a GAVS PhC device, where ω/ω_0 is the normalized frequency, $\omega_0 = 13.2 \times 10^{14}\,\text{Hz}$. Reproduced from [267], under the 'OSA Open Access Publishing Agreement'.

9.2 Fabrication of Devices

The GAVS PhC devices were fabricated using the process described in section 6.3, using a silicon nitride (Si_3N_4) thickness of 340 nm. A range of hole sizes were fabricated (140, 165, 190, 215 and 240 nm), due to concerns about the fragility of the devices with the desired 240 nm diameter holes; these concerns proved to be true, as the devices with the simulated hole size were too weak and either partially or fully collapsed. Micrographs of finished devices are shown in Figure 9.3, with zoomed in images showing how the hole size variation was manifested.

9.3 PL Imaging

Initial examination of the spiral devices was done using photoluminescence (PL) imaging. A typical PL image is shown in Figure 9.4a; the device has bright emission from the centre despite a lack of a mode in this region (as shown in Figure 9.2), later spectral measurements did not find a spectral feature associated with this bright spot. The high brightness may be due to very poor confinement, so there may be a very broad spectral feature associated with it – which was

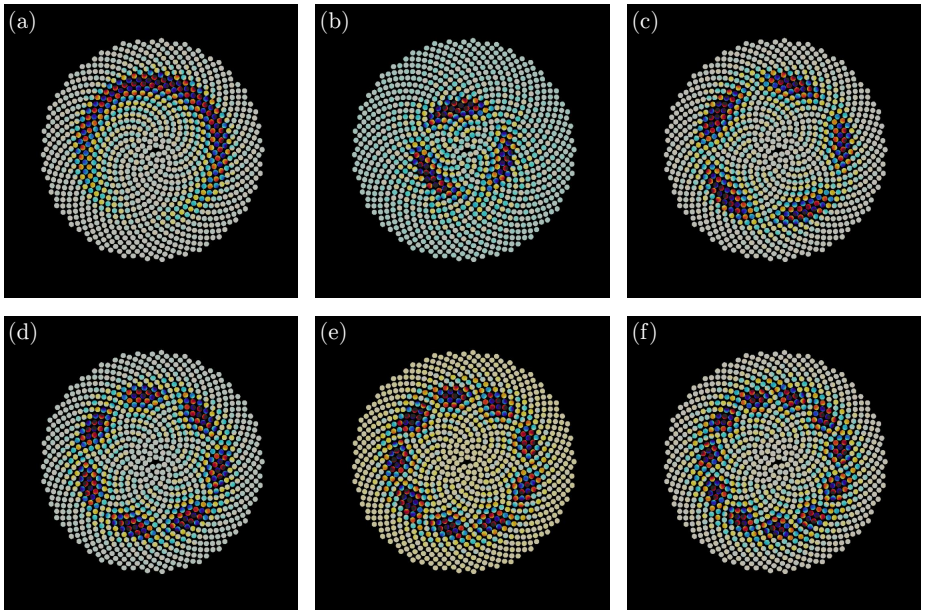

Figure 9.2: (a)-(f) Simulated mode profiles for the first six mode orders.

lost amongst the Si_3N_4 PL. There is also a bright ring around the edge of the device; this is believed to be caused by scattering of light, propagating through the Si_3N_4 membrane, from the edge of the PhC.

If the contrast of the image is altered to reduce the central bright-spot, a region of bright emission is seen surrounding the centre of the device, shown in Figure 9.4b. The ring-like nature of this feature would agree with the integration of all of the simulated modes shown in Figure 9.2, as the PL image was taken without spectral filtering, indicating that the light is confined strongly in this region.

9.4 Spectral Characterization

Devices were probed using a 405 nm continuous wave (CW) laser to excite the Si_3N_4, injecting photons into and probing selected regions of the device (within the $\sim 2.5\,\mu$m spot size). Almost all resonances were located in the region between the device centre and the crystal edge, in a ring-shaped distribution. Multiple resonances were seen in spectra taken throughout the device, with one location exhibiting 18 resonances within a 35 nm window, as shown in Figure 9.5a. Emission lines were fitted using a multi-peak Lorentz fit, one such example is shown in Figure 9.5b.

9.5 Analysis

Spectra from multiple positions on each device were taken (~ 16), for several devices, for the range of hole-size geometries fabricated. The spectral resonances were fitted to build-up a range of resonance wavelength and Q-factor statistics

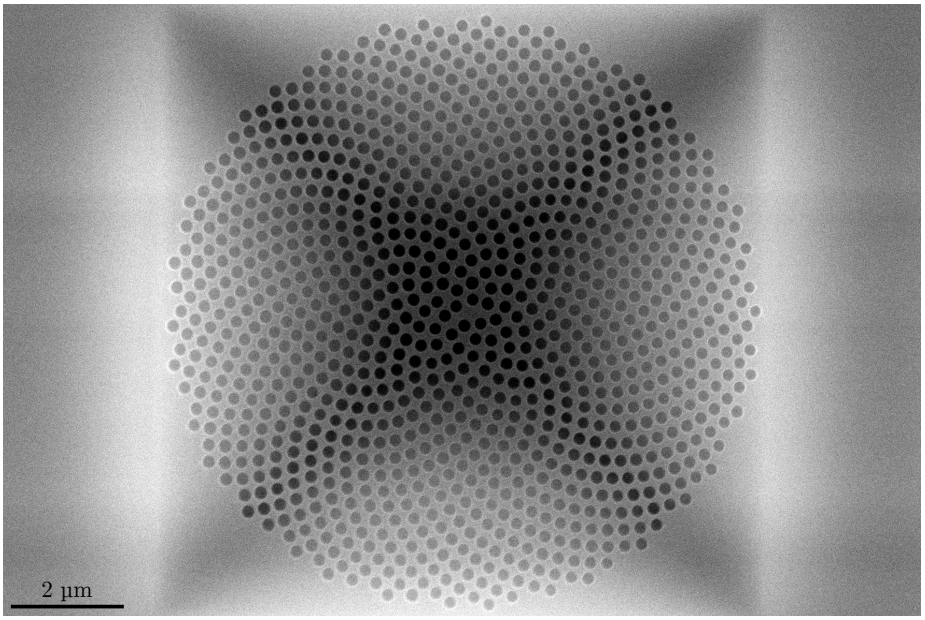

(a)

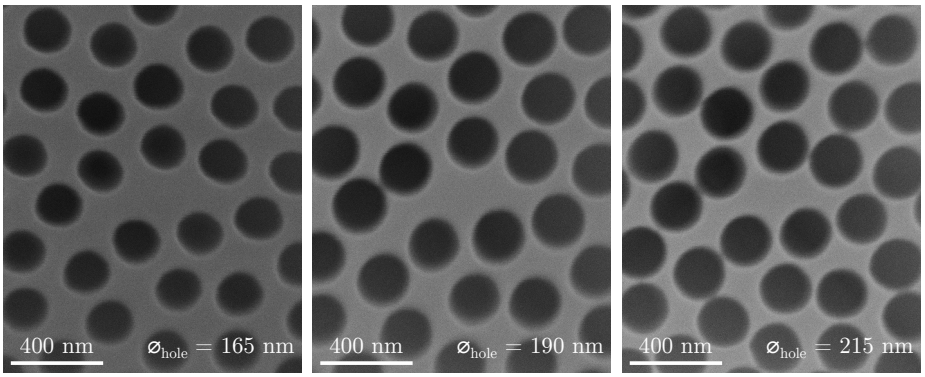

(b) (c) (d)

Figure 9.3: Scanning electron micrographs of: (a) Wide view of entire device with $\varnothing_{\text{hole}} = 165\,\text{nm}$. (b-d) Zoomed-in images of the centre of the devices for three hole sizes fabricated, respectively: 165 nm, 190 nm, and 215 nm.

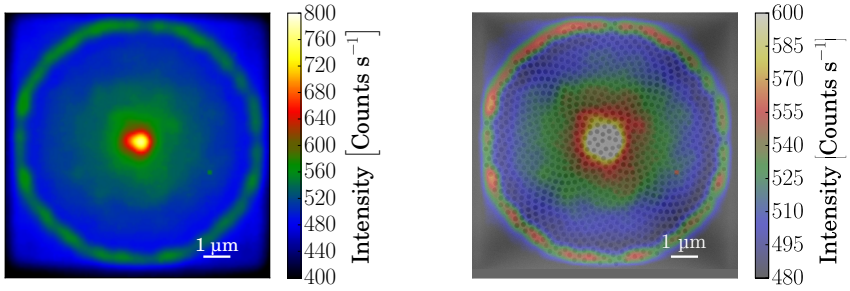

(a) (b)

Figure 9.4: PL images of a GAVS device with $\varnothing_{\text{hole}} = 165\,\text{nm}$. Taken using 455 nm light emitting diode (LED) excitation, with a 550 nm longpass filter (LPF), 2 s integration, 120 acquisitions, room temperature (R.T.) (a) Full-range colour scale image. (b) High-contrast image, showing the circular confinement of light around the device centre, overlaid with a scanning electron micrograph.

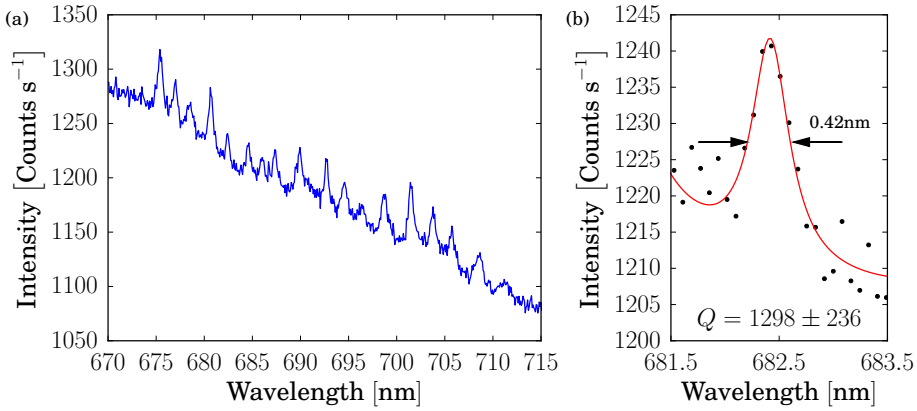

Figure 9.5: (a) PL spectrum taken from a GAVS device with $\varnothing_{\text{hole}} = 165\,\text{nm}$, showing 18 resonances within a 35 nm window. Taken under 405 nm CW laser excitation. (b) Spectral peak at 682.5 nm (symbols) shown with multi-peak Lorentz fit line.

(Figure 9.6). The distributions are made up of several devices for each hole size. As the hole size increases the resonances blue-shift, and decrease in Q-factor; the change is due to modification of the PhC bandgap. The individual distributions show some clustering of resonances into several bands: for example, with 165 nm hole size, there is increased density of resonances at 690, 710 and 725 nm. This clustering is predicted in simulations, as the modes of the structure occur at discrete wavelengths.

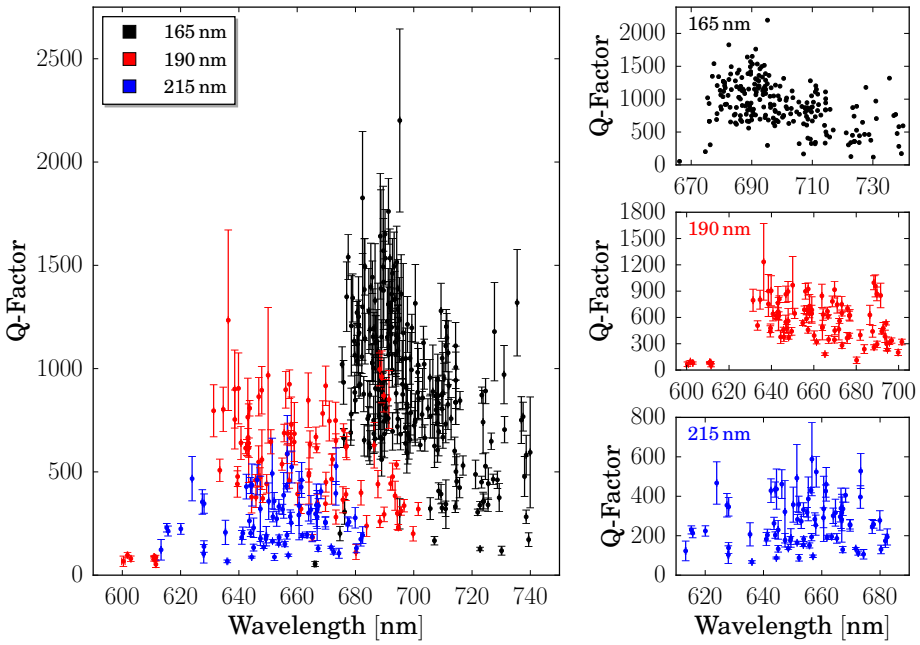

Figure 9.6: Left panel: Q-factor and peak wavelength for fitted resonances from three device geometries, showing blue-shifting of resonance distributions as hole diameter is increased. Right panels: individual plots for each geometry, error bars omitted for clarity on 165 nm plot.

The occurrence of Q-factors is shown in Figure 9.7. Anderson localized light would produce log-normal distributions [222], such as those shown in Figure 7.10b. The histogram for 165 nm holes is similar to a log-normal function, but there is insufficient data to say with certainty if the Q-factors are distributed as such at this stage.

9.6 Introducing Disorder

Initial work on the spiral devices started with devices designed to work in the 680-780 nm region; this was changed to better match the Si_3N_4 PL emission spectrum, allowing brighter excitation of the modes, for the devices reported in earlier sections. During the fabrication of these longer-wavelength devices, unintentional disorder was introduced during the lithographic stage, resulting in a variation in hole size. Measurements indicated that devices with an intended diameter of 225 nm, had a mean diameter of 236.6 nm and a standard deviation of 18.8 nm. This variation can clearly be seen in Figure 9.8a. As with the

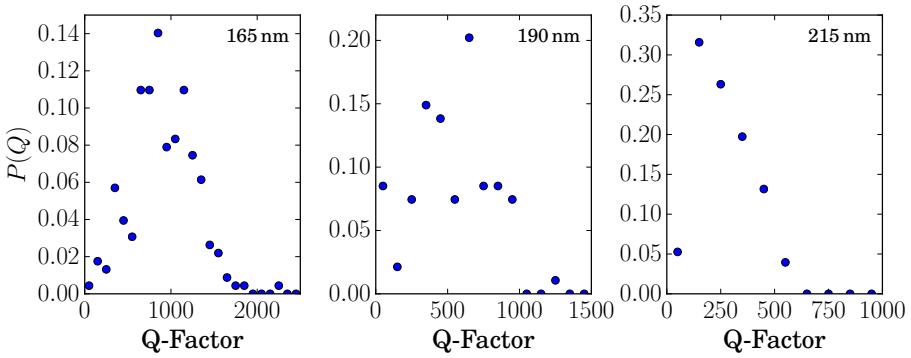

Figure 9.7: Histograms of Q-factor occurrence (symbols) for each geometry, fitted with a log-normal function (grey line).

localized modes in the PhC waveguides, as disorder was introduced hot-spots became visible in the PL images, Figure 9.8b for example. The increased disorder increases the rate of out-of-plane scattering of the light, allowing the modes to leak more light and become more visible when the emission is imaged. The PL image shows the modes form in the region surrounding the device centre.

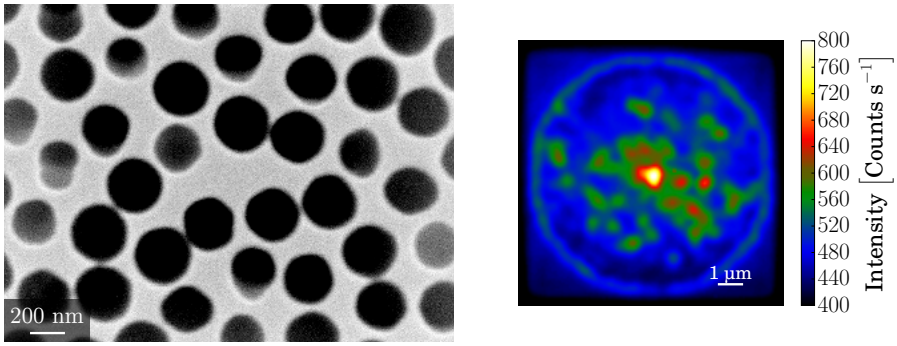

(a) (b)

Figure 9.8: Images of a $\varnothing_{\text{design}} = 225\,\text{nm}$ GAVS device with added disorder. (a) Scanning electron micrograph of device centre, showing hole size variation. (b) PL image showing randomly-distributed emission hot-sots. Taken using 455 nm LED excitation, with a 550 nm LPF, 2 s integration, 120 acquisitions, R.T.

When the distribution of the resonances is examined Figure 9.9a, it can be seen that these disordered devices have lower Q-factors than those from non-disordered devices; again, this is the same behaviour seen with the waveguides. The resonances seem to be grouped into clusters in wavelength-space; similar to that shown in simulations (Figure 9.9b), which is due to the modes forming only at certain wavelengths. As with ordered devices, the wavelength blue-shifts as the hole size increases.

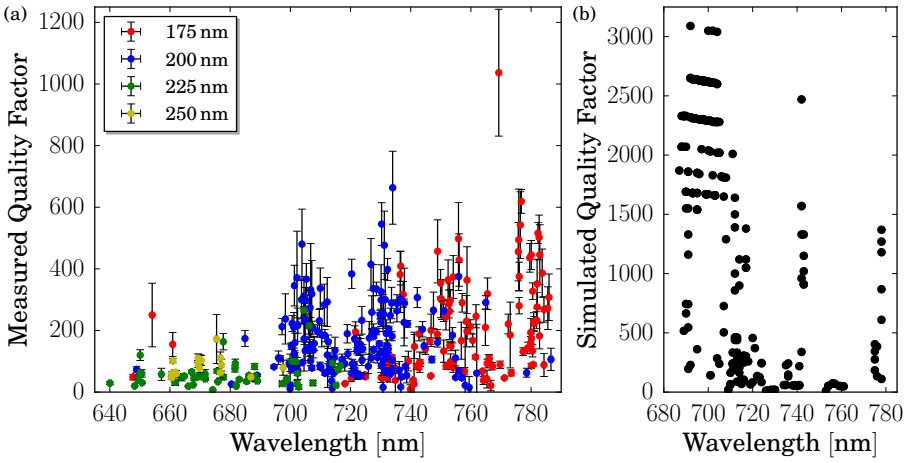

Figure 9.9: Resonance distributions (Q-factor and peak wavelength) for four different hole diameters with added disorder (coloured symbols), with the simulated performance (black symbols).

9.7 Conclusions

GAVSs structures have been fabricated in membranes crating aperiodic PhCs. PL images of the devices show light-confinement in a doughnut-like region surrounding the device centre, as predicted in simulations. Spectral characterization shows a distribution of resonances, with a maximum Q-factor of 2201 ± 443. Exceeding that of comparable L3 cavity systems [224]. Furthermore, as disorder is added, the visibility of modes when imaged increases, coupled with a decrease in Q-factor – as seen in Anderson localized systems.

This is an experimental demonstration of light confinement in an aperiodic system in 2D, which has the advantages of Anderson localization (high-quality light confinement), whilst removing the requirement of random disorder. These devices provide an alternative way of modifying the LDOS to that of using a cavity; this LDOS modification still provides the same benefits of increased light-matter coupling, such as Purcell enhancement. All of the demonstrations that have been made in sensing and cavity-quantum electrodynamics (QED) with periodic PhCs are applicable to this device.

Until now, GAVS devices have been studied in plasmonic systems, looking at modification of reflected light [272]. This work presents the first time that these devices have worked in emission, with light being directly injected, and using a PhC. This opens a new way to explore GAVSs, investigate the statistics of the light confinement, and investigate if light-confinement using aperiodic structures shows the same statistical signatures as other localization regimes [222].

Chapter 10

Concluding Remarks

> "The time has come," the Walrus said, "To talk of many things: Of shoes – and ships – and sealing-wax, Of cabbages – and kings, And why the sea is boiling hot, And whether pigs have wings."
>
> Lewis Carroll
> *The Walrus and The Carpenter (1871)*

Metallic Nanorings

The extraction of light to free space is a obstacle that needs to be overcome; for instance, when using solid-state emitters that are embedded in high refractive materials, such as GaAs. A number of devices have been developed to this ends: micropillars, nanowires and bullseye gratings. However, these devices suffer from fragility, difficulty of fabrication or narrow band-widths. A new device has been proposed: the metallic nanoring, which is deposited around a solid-state quantum dot. By using a confocal imaging and positioning technique, solid state quantum dot samples can be characterized and the location of quantum dots (QDs) retrieved. Metallic nanorings were fabricated around selected QDs using aligned electron beam lithography, metal evaporation and lift-off. The metallic nanorings increased the emission of QDs, compared to that of bulk, by up to $\times 25$. These devices no not require specialized growth of the substrate (as with micropillar cavities), and require only one lithographic step. Their relatively large feature size makes them accessible via nano-imprint and optical lithography. The device relies on a lensing effect to concentrate and focus the emitted light, and is intrinsically broadband. This allows compatibility with any emitter/substrate combination, such as single molecules, colloidal QDs, or diamond centres. These nanorings have shown proof-of-concept that they are able to provide emission enhancement. The metallic nanoring can be used as an electrical contact, allowing charge tuning of QDs via the Stark effect or direct electrical injection of carriers. The nanoring could also be coupled to an optical

fibre, creating a monolithic fibre-coupled single-photon source, as these devices are planar, whereas other cavity devices are not.

Combined Metallic Nanorings and Super-SILs

The metallic nanoring device was combined with a super-solid immersion lens (SIL), using a positionable deposition technique, to achieve a high-brightness photon source. The SIL provided a cumulative enhancement to the ring of up to $\times 10$, and 1^{st} lens fluxes of $\approx 1\,\text{MHz}$. This indicates that a potential enhancement of $\times 250$ is possible with optimally positioned nanorings and super-SILs. Again this scheme is emitter independent and compatible with a wide range of emitters, as it is broadband. The super-SIL has already been demonstrated to provide enhancement of emission from 2-dimensional materials. Combined super-SILs and nanoring devices mean that it is possible to realize high brightness single-photon sources in a single solid-state monolithic device, utilizing the best-in-class performance of solid state quantum dot. The nanorings enhance the lines from a QD differently, due to them arising from different charged states. The super-SIL is able to provide uniform enhancement, with enhancement of the emission for a brighter emitter. By also introducing a bottom reflector, to capture light lost down into the substrate, the brightness of a single QD can be increased further; realizing a bright, pure and indistinguishable source of single photons.

QDs for Plasmonic Applications

Plasmonic devices offer a route to high confinement of the electromagnetic field, but are generally cut-off from exploiting solid state quantum dot. Plasmonics confine the electric field on small length scales (10s of nanometres), whereas high-optical-quality Stranski-Krastanov QDs are typically buried under a comparatively thick ($> 50\,\text{nm}$) capping layer. Nanohole QDs have been grown with thin capping layers, but have degraded optical performance, with line-widths broader than 1 nm. A new annealing technique, internal thermal heating, which allows *in situ* annealing of droplet QDs, allows growth of QDs with extremely thin capping layers of 11 nm; whilst retaining relatively sharp emission lines. These bright, stable and narrow line-width emitters of single photons can be coupled to plasmonic devices where fundamental quantum electrodynamics experiments can be performed, as well as using plasmonic antenna devices to enhance emission of the emitters via the Purcell effect. Plasmonic devices, the metallic nanorings, can be deterministically deposited around selected QDs, providing lensing of the emission, Purcell enhancement (for spontaneous emission rate enhancement and increased indistinguishibility) and electrical control of the QD.

Anderson Localization of Visible Light

Photonic crystal devices provide control of the optical properties of a material. However, as devices shift to the visible light regime, fabrication imperfection begin to dominate, and performance drops. Highly engineered devices such a L3 cavities, which are highly sensitive to small ($\lesssim 5\,\text{nm}$) variations in design parameters, suffer from reduced quality-factors (Q-factors). Disordered photonics offers a route to realizing high Q-factor devices. By inducing Anderson

localization using disorder as a resource, high quality light confinement can be spontaneously made to appear along a photonic crystal (PhC) waveguide channel. The performance of these devices ($Q \approx 10,000$) exceed that of comparable highly engineered devices without the high investment of time and number of iterations to optimize the fabrication process. Furthermore, it has been shown that locations of the light confinement can be imaged and the positions determined. This represents the first time that Anderson localization has been directly imaged, and also for the first time demonstrated in the visible light regime in a photonic chip. The direct imaging allows the randomly distributed cavity modes to located with nm accuracy. This would allow emitters (such as a nitrogen-vacancy (NV)-centre containing nanodiamonds embedded within the bulk material before the PhC is fabricated) to be coupled to the waveguide resonances, exploiting the cavity effect they provide. By using low pressure chemical vapour deposition-grown Si_3N_4, the photoluminescence background can be substantially removed, removing the background of non-quantum light; this would clear the way for work coupling single photon emitters to the resonances for quantum applications. The modes also overlap, opening the way for necklace states, where photons can be passed from mode-to-mode, to be investigated; this could have application in transmission of quantum information encoded on photons in a network.

Sensing with Anderson Localization

The sharp resonances provided by Anderson localization can also be used as high-sensitivity sensors. A single mode was seen to shift by up to 100 times its line-width in response to the additional of isopropyl alcohol as a contaminant. This shift was fully reversible and repeatable. Additionally, when cooled (300 to 10 K), resonances blue-shifted by ~ 2 nm and halved in line-width. Proving that disorder-induced light confinement can be used to realize high-sensitivity sensors using a disorder-robust fabrication platform. PhC devices operating in the visible light regime have had limited scalability, due to the need to carefully engineer the devices and optimize the fabrication process over many iterations to mitigate against unavoidable fabrication imperfections. By using disorder as a resource, this barrier to scalability is removed. PhCs could be used to measure and quantify a contaminant reversibly. The temperature response of the devices can be used to tune them to the resonance of a chosen emitter, or to provide local temperature measurement in a device.

Aperiodic Photonic Crystals

Aperiodic PhCs offer a half-way-house between fully disordered devices and highly engineered ones. A mathematical relationship was used to procedurally place positions of holes in a membrane: the Vogel spiral. These devices modify the local density of states, creating regions of high density near the PhC band edge where modes can exist in the structure. These devices were fabricated and shown to have a maximum $Q = 2200$, again exceeding a comparable L3 cavity. Such devices are able to achieve light localization in 2 dimensions, relying on aperiodic structure instead of the disorder which is characteristic of Anderson localization. This is the first experimental demonstration of light confinement in a 2-dimensional (2D) aperiodic PhC structure, where the properties can be

studied in emission (previous demonstrations involving plasmonics worked in reflection). Therefore, as well as the high-quality light-confinement, these devices can allow further study and verification of the confinement mechanism in emission, and study of the localization statistics.

Unless I sneakily close the quote first."

Oliver Trojak

Appendix A

Fabrication Recipes

> Laws, like sausages, cease to inspire respect in proportion as we know how they are made.
>
> John Godfrey Saxe
> *(1869)*

Appendix A.1 Metallic Nanorings

A.1.1 Lithography of Grid

Resist: Dual methyl methacrylate (co-polymer) (MMA) EL6/poly(methyl methacrylate) (PMMA) 950A4 stack. MMA spun at 4000 RPM, 110°C hot-plate (HP) bake 2 mins. PMMA spun at 4000 RPM, 110°C HP bake 2 mins.

Step	Time [s]	End RPM
1	4	400
2	2	400
3	2	4000
4	40	4000
5	1	0

Tool: JEOL JBX 9300FS

Beam condition: '100kv_1na_60um'; Dose: 500 µC cm^{-2}; EHT: 100 kV; Beam current: 1.0 nA; Aperature: 60 µm; Shot pitch 4 nm; PEC layers: 16

Pattern: 30a,µm long, 1 µm wide, crosses in a 6×6 array

Develop: isopropyl alcohol (IPA):methyl isobutyl ketone (MIBK) 50:50, 50 s; IPA stop

A.1.2 Thermal Evaporation

Tool: Edwards 306A

Deposition pressure: 3×10^{-6} Torr minimum

1. 7 nm (typical) Cr, 1 Å s^{-1}; Variac: 18
2. Au, 1 Å s^{-1}; Variac: 40; 5 min pause every 50 nm with shutter closed to allow sample to cool

A.1.3 Aligned Lithography of Nanorings

Resist: PMMA 950A4 spun at 4000 RPM, 110°C HP bake 2 mins

Tool: JEOL JBX 9300FS

Beam condition: '100kv_100pa_60um_otj'; Dose: 500 µC cm^{-2}; EHT: 100 kV; Beam current: 0.1 nA; Aperature: 60 µm; Shot pitch 4 nm; No PEC; 4 Chip alignment cross scan: single scan, low gain, length: 5 µm

Develop: IPA:MIBK 50:50, 50 s; IPA stop

Appendix A.2 Photonic Crystal Membranes

A.2.1 PECVD of Si_3N_4

Tool: Oxford Instruments Plasma Lab LDS PECVD

1. Table heater to 350°C, 10 s
2. SiH_4 12 sccm, NH_3 20 sccm, N_2 500 sccm. Pressure 750 mTorr, 3 mins
3. SiH_4 12 sccm, NH_3 20 sccm, N_2 500 sccm. Pressure 750 mTorr, RF: 20 W forward. Deposit 250 nm at 0.28 nm s^{-1}
4. N_2 100 sccm, 2 mins

Chamber seasoned for 15 mins before deposition on samples.

A.2.2 Plasma Ashing

Tool: Gala Instrumente Plasma $Prep_2$

5 mins; Ar: 80%; Power: 80 W

A.2.3 Lithography of Photonic Crystals

Resist: CSAR6200.13, spun at 4000 RPM, 120°C HP bake 2 mins.

Tool: JEOL JBX 9300FS

Develop: CSAR developer, 70 s; IPA stop

Photonic Crystal Waveguides

Beam condition: '100kv_2na_60um'; Dose: 280 µC cm^{-2}; EHT: 100 kV; Beam current: 2.0 nA; Aperature: 60 µm; Shot pitch 6 nm; PEC layers: 16; Dose variations: 80%, 90%, 100%, 110%, 120%

Photonic Crystal L3 Cavities

Beam condition: '100kv_100pa_60um_otj'; Dose: 150 µC cm^{-2}; EHT: 100 kV; Beam current: 0.1 nA; Aperature: 60 µm; Shot pitch 4 nm; PEC layers: 16; Dose variations: 110%, 120%, 130%, 140%, 150%

Photonic Crystal Spiral Devices

Beam condition: '100kv_100pa_60um_otj'; Dose: 150 µC cm^{-2}; EHT: 100 kV; Beam current: 0.1 nA; Aperature: 60 µm; Shot pitch 4 nm; PEC layers: 16; Dose variations: 40%, 60%, 80%, 90%, 100%, 120%, 140%, 160%, 200%

A.2.4 Lithography of Etch Calibration Pattern

Resist: CSAR6200.13, spun at 4000 RPM, 120°C HP bake 2 mins.

I. probe: 2.4 pA; Spot size: 180 Å; I. target: 1.825 A; EHT: 20 kV; Beam current: 12 µA; Aperture: 20 µm; Step size: 12.0 nm; Exposure current: $\sim$ 44 pA; Dose: 65 µC cm^2; No PEC; Dose modifier: 1.0

Pattern: 3$\times$ 100 µm long, 300 nm wide trenches, 300 nm separation arrayed to form 1 mm long feature

Develop: CSAR developer, 70 s; IPA stop

A.2.5 ICP Etching of Silicon Nitride

Tool: Oxford Instruments Plasma Lab ICP380

1. Preflow: 30 s, 7.5$\times$10^{-9} mbar, He cooling 10.0 sccm, APC set pressure 5 mTorr. Gasses: SF_6 24 sccm, C_4F_8 44 sccm. Step transition hold.
2. Strike at 5mTorr: 5 s, 7.5$\times$10^{-9} mbar, He cooling 10.0 sccm, APC set pressure 5 mTorr. Gasses: SF_6 24 sccm, C_4F_8 44 sccm. RF forward power 21 W, ICP power 1000 W. Step transition hold.
3. Walk to 10 mTorr: 5 s, APC set pressure 10 mTorr. Step transition hold.
4. Walk to 15 mTorr: variable time, APC set pressure 15 mTorr. Step transition hold.
5. Purge: 30 s, 7.5$\times$10^{-9} mbar, He cooling 0.0 sccm, APC set pressure 15 mTorr. Gasses: Ar 50 sccm. Step transition hold.

Chamber seasoned for 15 mins before etching samples. Etch rate calibrated before each use (Figure A.1), as the rate varies between uses. Good thermal bonding of chip to carrier with vacuum grease is essential for a reliable etch rate. Nominally $\sim$1.74 nm s^{-1}.

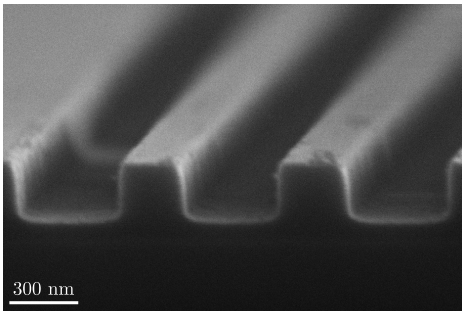

Figure A.1: Cross-sectional scanning electron micrograph of 300 nm wide trenches etched using inductively-coupled plasma (ICP), into a plasma-enhanced chemical vapour deposition (PECVD) grown silicon nitride (Si_3N_4) layer on a Si chip, used for etch rate calibration and process qualification.

A.2.6 Wet Undercut

Used to etch Si{100} anisotropically, $\sim$ 2 µm around features which provided undercut access. HCl step to remove potassium salt crystallization.

1. Etch: KOH; 45% w/w (deionized (DI) water dilution) at 70°C, 15 mins
2. Rinse: DI water; 1 min
3. Neutralize: HCl:DI 1:4 v/v; 5 mins
4. Rinse: DI water; 1 min
5. Dehydration: IPA; 1 min
6. Bake at 110°C, 1 min

Appendix A.3 Colloidal Quantum Dot Substrates

A.3.1 Indium tin oxide (ITO) Growth

Tool: BOC Edwards E500a E-Beam Evaporator

Deposition pressure: O_2 flow adjusted to keep chamber at 2.28×10^{-4} mBar after initial 1 hr pumpdown; Beam current: 11 mA; Deposition rate: 1.8 Å s^{-1}

Oxidization bake in ambient air (furnace vent holes opened) after deposition:

Step	Time [hrs]	Start Temp. [°C]	End Temp. [°C]
1	1	room temperature (R.T.)	500
2	1/2	500	500
3	4	500	R.T.

A.3.2 CdSe Quantum dot (QD) Coating

Tool: SPS Spin 150 Spin Coater

Solution make-up: CdSeS/ZnS 1 mg mℓ^{-1} toluene solution further diluted 1:2 with toluene, 0.18 µℓ mm^{-2} on chip

Step	Time [s]	End RPM	Ramp Rate [RPM s^{-1}]
1	10	1500	150
2	60	1500	150
3	10	1000	150
4	10	500	150
5	10	0	150

A.3.3 Lithography of Metallic Markers

Resist: Dual MMA EL6/PMMA 950A4 stack. MMA spun at 4000 RPM, 110°C HP bake 2 mins. PMMA spun at 4000 RPM, 110°C HP bake 2 mins.

Tool: LEO 1455VP, with Raith ELPHY Quantum

I. probe: 2.4 pA; Spot size: 180 Å; I. target: 1.825 A; EHT: 20 kV; Beam current: 12 µA; Aperture: 20 µm; Step size: 19.2 nm; Exposure current: $\sim$ 44 pA; Dose: 110 µC cm^2; PEC layers: 16; Dose modifier: 1.2

Pattern: 30 µm long, 1 µm wide, crosses in a 6 $\times$ 6 array

Develop: IPA:MIBK 50:50, 50 s; IPA stop

A.3.4 Aligned Lithography of Micro-rings

Resist: Dual MMA EL6/PMMA 950A4 stack. MMA spun at 4000 RPM, 110°C HP bake 2 mins. PMMA spun at 4000 RPM, 110°C HP bake 2 mins.

Tool: LEO 1455VP, with Raith ELPHY Quantum

I. probe: 2.4 pA; Spot size: 180 Å; I. target: 1.825 A; EHT: 20 kV; Beam current: 12 µA; Aperture: 20 µm; Step size: 19.2 nm; Exposure current: $\sim$ 44 pA; Dose: 110 µC/cm^2; No PEC; Dose modifier: 1.1

Pattern: Nanoring mask, fractured to 19.2 nm grid using BEAMER, 6-side polygon fracture; alignment scan boxes in layer 63

Develop: IPA:MIBK 50:50, 50 s; IPA stop

Figure A.2 shows a feature size test of three designs of metallic nanorings patterned using the above recipe and metallized in Au. A detailed description of the alignment procedure can be found in [274].

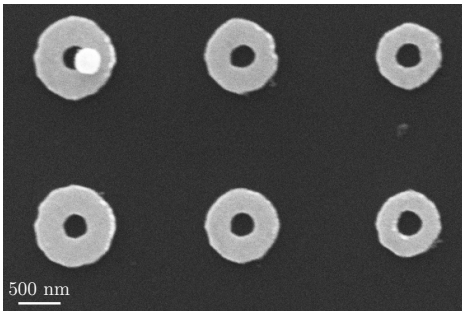

Figure A.2: Scanning electron micrograph of metallic nanorings. The three designs have $\varnothing_{\text{design}} = 400\,\text{nm}$; and wall thicknesses of: 250, 200 and 150 nm (left to right).

References

[1] J. D. Hunter, "Matplotlib: A 2D graphics environment," *Computing in Science and Engineering*, vol. 9, no. 3, pp. 99–104, 2007. [Online]. Available: http://dx.doi.org/10.1109/MCSE.2007.55

[2] O. Darrigol, *A History of Optics from Greek Antiquity to the Nineteenth Century*. Oxford University Press, 2012.

[3] Euclid and H. E. Burton, "The Optics of Euclid," pp. 357–372, 1945. [Online]. Available: http://dx.doi.org/10.1364/JOSA.35.000357

[4] J. Al-Khalili, "In retrospect: Book of Optics," *Nature*, vol. 518, no. 7538, pp. 164–165, feb 2015. [Online]. Available: http://dx.doi.org/10.1038/518164a

[5] I. Newton, *Opticks: Or a Treatise of the Reflections, Refractions, Inflections and Colours of Light*, ser. Cosimo classics science. Cosimo, 2007.

[6] ——, "A Letter of Mr. Isaac Newton, Professor of the Mathematicks in the University of Cambridge; Containing His New Theory about Light and Colors: Sent by the Author to the Publisher from Cambridge, Febr. 6. 1671/72; In Order to be Communicated to the R. S." *Philosophical Transactions of the Royal Society of London*, vol. 6, no. 69-80, pp. 3075–3087, jan 1671. [Online]. Available: http://dx.doi.org/10.1098/rstl.1671.0072

[7] C. Huygens, *Treatease on Light*, S. P. Thompson, Ed. London: Macmillan and Co., Limited, 1912. [Online]. Available: http://www.nrel.gov/docs/fy02osti/30769.pdf

[8] T. Young, "The Bakerian Lecture: On the Theory of Light and Colours," *Philosophical Transactions of the Royal Society of London*, vol. 92, no. January, pp. 12–48, 1802. [Online]. Available: http://dx.doi.org/10.1098/rstl.1802.0004

[9] ——, "The Bakerian Lecture: Experiments and Calculations Relative to Physical Optics," *Philosophical Transactions of the Royal Society of London*, vol. 94, pp. 1–16, 1804. [Online]. Available: http://dx.doi.org/10.1098/rstl.1804.0001

[10] J. Clerk Maxwell, "A Dynamical Theory of the Electromagnetic Field," *Philosophical Transactions of the Royal Society of London*, vol. 155, no. January, pp. 459–512, 1865. [Online]. Available: http://dx.doi.org/10.1098/rstl.1865.0008

[11] A. A. Michelson and E. W. Morley, "On the Relative Motion of the Earth and the Luminiferous Ether," *American Journal of Science - Third Series*, vol. 34, no. 203, pp. 333–345, 1887. [Online]. Available: https://history.aip.org/exhibits/gap/PDF/michelson.pdf

[12] A. Einstein, "On the electrodynamics of moving bodies (Zur Elektrodynamik bewegter Körper), Translated by John Walker," *Annalen der Physik*, vol. 17, p. 891, 1905. [Online]. Available: http://dx.doi.org/10.1002/andp.19053221004

[13] ——, "Does The Inertia of a Body Depend Upon Its Energy-Content (Ist die Trägheit eines Körpers von seinem Energieinhalt abhängig?), Translated by John Walker," *Annalen der Physik*, vol. 323, no. 13, pp. 639–641, 1905. [Online]. Available: http://dx.doi.org/10.1002/andp.19053231314

[14] M. Planck, "On the law of the energy distribution in the normal spectrum," *Annalen der Physik*, vol. 4, p. 553, 1901. [Online]. Available: http://dx.doi.org/10.1002/andp.19013090310

[15] A. B. Arons and M. B. Peppard, "Einstein's Proposal of the Photon Concepta Translation of the Annalen der Physik Paper of 1905," *American Journal of Physics*, vol. 33, no. 5, pp. 367–374, may 1965. [Online]. Available: https://doi.org/10.1119/1.1971542

[16] W. E. Lamb and M. O. Scully, "The photoelectric effect without photons," University of Miami / Coral Gables, Florida, Miami, Tech. Rep., 1968. [Online]. Available: http://users.unimi.it/aqm/wp-content/uploads/Lamb-1968.pdf

[17] H. J. Kimble, M. Dagenais, and L. Mandel, "Photon antibunching in resonance fluorescence," *Physical Review Letters*, vol. 39, no. 11, pp. 691–695, 1977. [Online]. Available: https://doi.org/10.1103/PhysRevLett.39.691

[18] L. de Broglie, "Ondes et Quanta (Waves and Quanta), Translated by Jean Perrin," *Comptes Rendus*, vol. 177, pp. 507–510, 1923. [Online]. Available: http://strangepaths.com/wp-content/uploads/2008/01/rendus-e.pdf

[19] A. H. Compton, "A Quantum Theory of the Scattering of X Rays By Light Elements," *The Physical Review*, vol. 21, no. 5, pp. 483–502, 1923. [Online]. Available: http://dx.doi.org/10.1103/PhysRev.21.483

[20] G. P. Thomson and A. Reid, "Diffraction of Cathode Rays by a Thin Film," *Nature*, vol. 119, no. 3007, pp. 890–890, jun 1927. [Online]. Available: http://dx.doi.org/10.1038/119890a0

[21] G. P. Thomson, "Experiments on the Diffraction of Cathode Rays," *Proceedings of the Royal Society of London. Series A*, vol. 117, no. 778, pp. 600–609, 1928. [Online]. Available: http://dx.doi.org/10.1016/S0016-0032(28)90933-3

[22] D. Jones, *Atomic Physics*, ser. Physics and Its Applications. CRC Press (Taylor & Francis), 1997.

[23] M. Fox, *Quantum Optics: An Introduction*, ser. Oxford Master Series in Physics. Oxford University Press, 2006.

[24] R. Hanbury Brown and R. Q. Twiss, "A Test of a New Type of Stellar Interferometer on Sirius," *Nature*, vol. 178, no. 4541, pp. 1046–1048, 1956. [Online]. Available: https://doi.org/10.1038/1781046a0

[25] ——, "Interferometry of the Intensity Fluctuations in Light. I. Basic Theory: The Correlation between Photons in Coherent Beams of Radiation," London, pp. 300–324, 1957. [Online]. Available: https://doi.org/10.1098/rspa.1957.0177

[26] ——, "Interferometry of the Intensity Fluctuations in Light II. An Experimental Test of the Theory for Partially Coherent Light," pp. 291–319, 1958. [Online]. Available: https://doi.org/10.1098/rspa.1958.0001

[27] L. Sapienza, M. Davanço, A. Badolato, and K. Srinivasan, "Nanoscale optical positioning of single quantum dots for bright and pure single-photon emission," *Nature Communications*, vol. 6, p. 7833, 2015. [Online]. Available: http://dx.doi.org/10.1038/ncomms8833

[28] C. M. Santori, "Generation of Nonclassical Light Using Semiconductor Quantum Dots," Ph.D. dissertation, Stanford University, 2003.

[29] E. Knill, R. Laflamme, and G. J. Milburn, "A scheme for efficient quantum computation with linear optics." *Nature*, vol. 409, no. 6816, pp. 46–52, 2001. [Online]. Available: http://dx.doi.org/10.1038/35051009

[30] D. Bouwmeester, J.-W. Pan, K. Mattle, M. Eibl, H. Weinfurter, and A. Zeilinger, "Experimental quantum teleportation," *Nature*, vol. 390, no. 6660, pp. 575–579, 1997. [Online]. Available: https://doi.org/10.1038/37539

[31] Y. Shih and C. O. Alley, "New Type of Einstein-Podolsky-Rosen-Bohm Experiment Using Pairs of Light Quanta Produced by Optical Parametric Down Conversion," *Physical Review Letters*, vol. 61, no. 26, pp. 2921–2924, 1988. [Online]. Available: https://doi.org/10.1103/PhysRevLett.61.2921

[32] C. K. Hong, Z. Y. Ou, and L. Mandel, "Measurement of Subpicosecond Time Intervals between Two Photons by Interference," *Physical Review Letters*, vol. 59, no. 18, pp. 2044–2046, 1987. [Online]. Available: http://dx.doi.org/10.1103/PhysRevLett.59.2044

[33] M. Jachura and R. Chrapkiewicz, "Shot-by-shot imaging of Hong-Ou-Mandel interference with an intensified sCMOS camera." *Optics letters*, vol. 40, no. 7, pp. 1540–1543, 2015. [Online]. Available: http://dx.doi.org/10.1364/OL.40.001540

[34] L. Monniello, A. Reigue, R. Hostein, A. Lemaître, A. Martinez, R. Grousson, and V. Voliotis, "Indistinguishable single photons generated by a quantum dot under resonant excitation observable without postselection," *Physical Review B*, vol. 90, no. 4, p. 041303, 2014. [Online]. Available: http://dx.doi.org/10.1103/PhysRevB.90.041303

[35] H. Fearn and R. Loudon, "Theory of two-photon interference," *Journal of the Optical Society of America B*, vol. 6, no. 5, p. 917, 1989. [Online]. Available: https://doi.org/10.1364/JOSAB.6.000917

[36] H. J. Kimble, "The quantum internet," *Nature*, vol. 453, no. 7198, pp. 1023–1030, jun 2008. [Online]. Available: https://doi.org/10.1038/nature07127

[37] M. M. Waldrop, "The chips are down for Moore's law," *Nature*, vol. 530, no. 7589, pp. 144–147, feb 2016. [Online]. Available: https://doi.org/10.1038/530144a

[38] "Death notice: Moores Law. 19 April 1965 2 January 2018," https://www.theregister.co.uk/2018/01/24/death_notice_for_moores_law/, accessed: 2018-01-24.

[39] P. Shor, "Algorithms for quantum computation: discrete logarithms and factoring," in *Proceedings: 35th Annual Symposium on Foundations of Computer Science*. Santa Fe, NM, USA: IEEE Computer Society Washington DC, 1994, pp. 124–134. [Online]. Available: http://dx.doi.org/10.1109/SFCS.1994.365700

[40] L. K. Grover, "From Schrodinger's equation to the quantum search algorithm," *Pramana*, vol. 56, no. 2-3, pp. 333–348, 2001. [Online]. Available: http://dx.doi.org/10.1007/s12043-001-0128-3

[41] D. P. DiVincenzo and IBM, "The Physical Implementation of Quantum Computation," *Fortschritte der Physik*, vol. 48, pp. 771–783, 2000. [Online]. Available: http://arxiv.org/abs/quant-ph/0002077

[42] C. Monroe, "Quantum information processing with atoms and photons," *Nature*, vol. 416, no. 6877, pp. 238–246, mar 2002. [Online]. Available: http://dx.doi.org/10.1038/416238a

[43] G. Wendin, "Quantum information processing with superconducting circuits: A review," *Reports on Progress in Physics*, vol. 80, no. 10, p. aa7e1a, 2017. [Online]. Available: https://doi.org/10.1088/1361-6633/aa7e1a

[44] C. Song, K. Xu, W. Liu, C. P. Yang, S. B. Zheng, H. Deng, Q. Xie, K. Huang, Q. Guo, L. Zhang, P. Zhang, D. Xu, D. Zheng, X. Zhu, H. Wang, Y. A. Chen, C. Y. Lu, S. Han, and J. W. Pan, "10-Qubit Entanglement and Parallel Logic Operations with a Superconducting Circuit," *Physical Review Letters*, vol. 119, no. 18, pp. 1–6, 2017. [Online]. Available: https://doi.org/10.1103/PhysRevLett.119.180511

[45] H. Paik, D. I. Schuster, L. S. Bishop, G. Kirchmair, G. Catelani, A. P. Sears, B. R. Johnson, M. J. Reagor, L. Frunzio, L. I. Glazman, S. M. Girvin, M. H. Devoret, and R. J. Schoelkopf, "Observation of high coherence in Josephson junction qubits measured in a three-dimensional circuit QED architecture," *Physical Review Letters*, vol. 107, no. 24, pp. 1–5, 2011. [Online]. Available: https://doi.org/10.1103/PhysRevLett.107.240501

[46] K. R. Brown, J. Kim, and C. Monroe, "Co-designing a scalable quantum computer with trapped atomic ions," *npj Quantum Information*, vol. 2, no. 1, p. 16034, nov 2016. [Online]. Available: https://doi.org/10.1038/npjqi.2016.34

[47] A. Cho, "Quantum or not, controversial computer yields no speedup," *Science*, vol. 344, no. 6190, pp. 1330–1331, jun 2014. [Online]. Available: http://dx.doi.org/10.1126/science.344.6190.1330

[48] D. Castelvecchi, "IBM's quantum cloud computer goes commercial," *Nature*, vol. 543, no. 7644, pp. 159–159, mar 2017. [Online]. Available: https://doi.org/10.1038/nature.2017.21585

[49] T. D. Ladd, F. Jelezko, R. Laflamme, Y. Nakamura, C. Monroe, and J. L. O'Brien, "Quantum computers," *Nature*, vol. 464, no. 7285, pp. 45–53, 2010. [Online]. Available: http://dx.doi.org/10.1038/nature08812

[50] J. L. O'Brien, "Optical Quantum Computing," *Science*, vol. 318, no. 5856, pp. 1567–1570, dec 2007. [Online]. Available: http://dx.doi.org/10.1126/science.1142892

[51] W. K. Wootters and W. H. Zurek, "A single quantum cannot be cloned," *Nature*, vol. 299, no. 5886, pp. 802–803, 1982. [Online]. Available: http://dx.doi.org/10.1038/299802a0

[52] H.-K. Lo, M. Curty, and K. Tamaki, "Secure quantum key distribution," *Nature Photonics*, vol. 8, no. July, p. 595, 2014. [Online]. Available: https://doi.org/10.1038/nphoton.2014.149

[53] C. H. Bennett and G. Brassard, "Quantum cryptography: Public key distribution and coin tossing," in *International Conference on Computers, Systems & Signal processing*, vol. 1. Bangalore: IEEE, 1984, pp. 175–179. [Online]. Available: https://doi.org/10.1016/j.tcs.2011.08.039

[54] K. Svozil, "Staging quantum cryptography with chocolate balls," *American Journal of Physics*, vol. 74, no. 9, pp. 800–803, sep 2006. [Online]. Available: https://doi.org/10.1119/1.2205879

[55] H. Singh, D. L. Gupta, and A. K. Singh, "Quantum Key Distribution Protocols: A Review," *IOSR Journal of Computer Engineering*, vol. 16, no. 2, pp. 1–9, 2014. [Online]. Available: https://doi.org/10.9790/0661-162110109

[56] C. H. Bennett and G. Brassard, "Experimental quantum cryptography: the dawn of a new era for quantum cryptography: the experimental prototype is working!" *Sigact News*, vol. 20, no. 4, pp. 78–80, 1989. [Online]. Available: https://doi.org/10.1145/74074.74087

[57] E. O. Kiktenko, N. O. Pozhar, A. V. Duplinskiy, A. A. Kanapin, A. S. Sokolov, S. S. Vorobey, A. V. Miller, V. E. Ustimchik, M. N. Anufriev, A. S. Trushechkin, R. R. Yunusov, V. L. Kurochkin, Y. V. Kurochkin, and A. K. Fedorov, "Demonstration of a quantum key distribution network in urban fibre-optic communication lines," *Quantum Electronics*, vol. 47, no. 9, pp. 798–802, sep 2017. [Online]. Available: http://dx.doi.org/10.1070/QEL16469

[58] R. Ursin, F. Tiefenbacher, T. Schmitt-Manderbach, H. Weier, T. Scheidl, M. Lindenthal, B. Blauensteiner, T. Jennewein, J. Perdigues, P. Trojek, B. Ömer, M. Fürst, M. Meyenburg, J. Rarity, Z. Sodnik, C. Barbieri, H. Weinfurter, and A. Zeilinger, "Entanglement-based quantum communication over 144km," *Nature Physics*, vol. 3, no. 7, pp. 481–486, 2007. [Online]. Available: http://dx.doi.org/10.1038/nphys629

[59] S.-K. Liao, W.-Q. Cai, W.-Y. Liu, L. Zhang, Y. Li, J.-G. Ren, J. Yin, Q. Shen, Y. Cao, Z.-P. Li, F.-Z. Li, X.-W. Chen, L.-H. Sun, J.-J. Jia, J.-C. Wu, X.-J. Jiang, J.-F. Wang, Y.-M. Huang, Q. Wang, Y.-L. Zhou, L. Deng, T. Xi, L. Ma, T. Hu, Q. Zhang, Y.-A. Chen, N.-L. Liu, X.-B. Wang, Z.-C. Zhu, C.-Y. Lu, R. Shu, C.-Z. Peng, J.-Y. Wang, and J.-W. Pan, "Satellite-to-ground quantum key distribution," *Nature*, vol. 549, no. 7670, pp. 43–47, aug 2017. [Online]. Available: https://doi.org/10.1038/nature23655

[60] C. H. Bennett, G. Brassard, C. Crépeau, R. Jozsa, A. Peres, and W. K. Wootters, "Teleporting an unknown quantum state via dual classical and Einstein-Podolsky-Rosen channels," *Physical Review Letters*, vol. 70, no. 13, pp. 1895–1899, mar 1993. [Online]. Available: https://doi.org/10.1103/PhysRevLett.70.1895

[61] A. Einstein, B. Podolsky, and N. Rosen, "Can Quantum-Mechanical Description of Physical Reality Be Considered Complete?" *Physical Review*, vol. 47, no. 10, pp. 777–780, may 1935. [Online]. Available: https://doi.org/10.1103/PhysRev.47.777

[62] J.-G. Ren, P. Xu, H.-L. Yong, L. Zhang, S.-K. Liao, J. Yin, W.-Y. Liu, W.-Q. Cai, M. Yang, L. Li, K.-X. Yang, X. Han, Y.-Q. Yao, J. Li, H.-Y. Wu, S. Wan, L. Liu, D.-Q. Liu, Y.-W. Kuang, Z.-P. He, P. Shang, C. Guo, R.-H. Zheng, K. Tian, Z.-C. Zhu, N.-L. Liu, C.-Y. Lu, R. Shu, Y.-A. Chen, C.-Z. Peng, J.-Y. Wang, and J.-W. Pan, "Ground-to-satellite quantum teleportation," *Nature*, vol. 549, no. 7670, pp. 70–73, aug 2017. [Online]. Available: https://doi.org/10.1038/nature23675

[63] A. Angelow and M. C. Batoni, "About Heisenberg Uncertainty Relation (by E.Schrodinger)," *Proceedings of The Prussian Academy of Sciences*, vol. XIX, pp. 296–303, 1930. [Online]. Available: http://arxiv.org/abs/quant-ph/9903100

[64] V. Giovannetti, S. Lloyd, and L. Maccone, "Quantum-enhanced measurements: beating the standard quantum limit." *Science*, vol. 306, no. 5700, pp. 1330–1336, 2004.

[65] ——, "Advances in quantum metrology," *Nature Photonics*, vol. 5, no. 4, pp. 222–229, 2011. [Online]. Available: http://dx.doi.org/10.1038/nphoton.2011.35

[66] M. J. Padgett and R. W. Boyd, "An introduction to ghost imaging: quantum and classical," *Philosophical Transactions of the Royal Society A: Mathematical, Physical and Engineering Sciences*, vol. 375, no. 2099, p. 20160233, 2017. [Online]. Available: https://doi.org/10.1098/rsta.2016.0233

[67] N. Piro, F. Rohde, C. Schuck, M. Almendros, J. Huwer, J. Ghosh, A. Haase, M. Hennrich, F. Dubin, and J. Eschner, "Heralded single-photon absorption by a single atom," *Nature Physics*, vol. 7, no. 1, pp. 17–20, 2011. [Online]. Available: http://dx.doi.org/10.1038/nphys1805

[68] J. A. Rushton, M. Aldous, and M. D. Himsworth, "Contributed Review: The feasibility of a fully miniaturized magneto-optical trap for portable ultracold quantum technology," *Review of Scientific Instruments*, vol. 85, no. 12, p. 121501, 2014. [Online]. Available: http://dx.doi.org/10.1063/1.4904066

[69] S. Buckley, K. Rivoire, and J. Vučković, "Engineered quantum dot single-photon sources." *Reports on Progress in Physics*, vol. 75, p. 126503, 2012. [Online]. Available: http://dx.doi.org/10.1088/0034-4885/75/12/126503

[70] H. Ritsch, P. Domokos, F. Brennecke, and T. Esslinger, "Cold atoms in cavity-generated dynamical optical potentials," *Reviews of Modern Physics*, vol. 85, no. 2, pp. 553–601, 2013. [Online]. Available: http://dx.doi.org/10.1103/RevModPhys.85.553

[71] T. Basché, W. E. Moerner, M. Orrit, and H. Talon, "Photon antibunching in the fluorescence of a single dye molecule trapped in a solid," *Physical Review Letters*, vol. 69, no. 10, pp. 1516–1519, sep 1992. [Online]. Available: http://dx.doi.org/10.1103/PhysRevLett.69.1516

[72] J. Friedrich and D. Haarer, "Photochemical Hole Burning: A Spectroscopic Study of Relaxation Processes in Polymers and Glasses," *Angewandte Chemie International Edition in English*, vol. 23, no. 2, pp. 113–140, 1984. [Online]. Available: http://dx.doi.org/10.1002/anie.198401131

[73] B. Lounis and M. Orrit, "Single-photon sources," pp. 1129–1179, may 2005. [Online]. Available: http://dx.doi.org/10.1088/0034-4885/68/5/R04

[74] F. Jelezko and J. Wrachtrup, "Single defect centres in diamond: A review," *Physica Status Solidi A: Applications and Materials Science*, vol. 203, no. 13, pp. 3207–3225, 2006. [Online]. Available: http://dx.doi.org/10.1002/pssa.200671403

[75] M. W. Doherty, N. B. Manson, P. Delaney, F. Jelezko, J. Wrachtrup, and L. C. Hollenberg, "The nitrogen-vacancy colour centre in diamond," *Physics Reports*, vol. 528, no. 1, pp. 1–45, jul 2013. [Online]. Available: http://dx.doi.org/10.1016/j.physrep.2013.02.001

[76] C. Santori, D. Fattal, and Y. Yamamoto, *Single-photon Devices and Applications*, ser. Physics Textbook Series. John Wiley & Sons, 2010.

[77] I. Aharonovich, A. D. Greentree, and S. Prawer, "Diamond photonics," *Nature Photonics*, vol. 5, no. 7, pp. 397–405, 2011. [Online]. Available: http://dx.doi.org/10.1038/nphoton.2011.54

[78] A. A. Martin, S. Randolph, A. Botman, M. Toth, and I. Aharonovich, "Maskless milling of diamond by a focused oxygen ion beam," *Scientific Reports*, vol. 5, p. 8958, 2015. [Online]. Available: http://dx.doi.org/10.1038/srep08958

[79] M. J. Burek, N. P. De Leon, B. J. Shields, B. J. Hausmann, Y. Chu, Q. Quan, A. S. Zibrov, H. Park, M. D. Lukin, and M. Lončar, "Free-standing mechanical and photonic nanostructures in single-crystal diamond," *Nano Letters*, vol. 12, no. 12, pp. 6084–6089, 2012. [Online]. Available: http://dx.doi.org/10.1021/nl302541e

[80] I. Aharonovich, J. C. Lee, A. P. Magyar, D. O. Bracher, and E. L. Hu, "Bottom-up engineering of diamond micro- and nano-structures," *Laser and Photonics Reviews*, vol. 7, no. 5, pp. 61–65, 2013. [Online]. Available: https://doi.org/10.1002/lpor.201300065

[81] Z. Su, W. Zhou, and Y. Zhang, "New insight into the soot nanoparticles in a candle flame," *Chemical Communications*, vol. 47, no. 16, pp. 4700–4702, 2011. [Online]. Available: http://dx.doi.org/10.1039/c0cc05785a

[82] A. W. Schell, G. Kewes, T. Hanke, A. Leitenstorfer, R. Bratschitsch, O. Benson, and T. Aichele, "Single defect centers in diamond nanocrystals as quantum probes for plasmonic nanostructures," *Optics Express*, vol. 19, no. 8, p. 7914, 2011. [Online]. Available: http://dx.doi.org/10.1364/OE.19.007914

[83] A. Högele, C. Galland, M. Winger, and A. Imamolu, "Photon antibunching in the photoluminescence spectra of a single carbon nanotube," *Physical Review Letters*, vol. 100, no. 21, pp. 5–8, 2008. [Online]. Available: http://dx.doi.org/10.1103/PhysRevLett.100.217401

[84] X. Ma, N. F. Hartmann, J. K. S. Baldwin, S. K. Doorn, and H. Htoon, "Room-temperature single-photon generation from solitary dopants of carbon nanotubes," *Nature Nanotechnology*, vol. 10, no. 8, pp. 671–675, 2015. [Online]. Available: http://dx.doi.org/10.1038/nnano.2015.136

[85] M. Kumar and Y. Ando, "Chemical Vapor Deposition of Carbon Nanotubes: A Review on Growth Mechanism and Mass Production," *Journal of Nanoscience and Nanotechnology*, vol. 10, no. 6, pp. 3739–3758, 2010. [Online]. Available: http://dx.doi.org/10.1166/jnn.2010.2939

[86] X. Ma, L. Adamska, H. Yamaguchi, S. E. Yalcin, S. Tretiak, S. K. Doorn, and H. Htoon, "Electronic structure and chemical nature of oxygen dopant states in carbon nanotubes," *ACS Nano*, vol. 8, no. 10, pp. 10 782–10 789, 2014. [Online]. Available: https://doi.org/10.1021/nn504553y

[87] K. S. Novoselov, A. K. Geim, S. V. Morozov, D. Jiang, Y. Zhang, S. V. Dubonos, I. V. Grigorieva, and A. A. Firsov, "Electric Field Effect in Atomically Thin Carbon Films," *Science*, vol. 306, no. 5696, pp. 666–669, 2004. [Online]. Available: http://dx.doi.org/10.1126/science.1102896

[88] F. Xia, H. Wang, D. Xiao, M. Dubey, and A. Ramasubramaniam, "Two-dimensional material nanophotonics," *Nature Photonics*, vol. 8,

no. 12, pp. 899–907, 2014. [Online]. Available: http://dx.doi.org/10.1038/nphoton.2014.271

[89] A. Srivastava, M. Sidler, A. V. Allain, D. S. Lembke, A. Kis, and A. Imamoglu, "Optically active quantum dots in monolayer WSe2," *Nature Nanotechnology*, vol. 10, no. 6, pp. 491–496, 2015. [Online]. Available: http://dx.doi.org/10.1038/nnano.2015.60

[90] Y. Huang, E. Sutter, N. N. Shi, J. Zheng, T. Yang, D. Englund, H. J. Gao, and P. Sutter, "Reliable Exfoliation of Large-Area High-Quality Flakes of Graphene and Other Two-Dimensional Materials," *ACS Nano*, vol. 9, no. 11, pp. 10 612–10 620, 2015. [Online]. Available: http://dx.doi.org/10.1021/acsnano.5b04258

[91] S. Tongay, W. Fan, J. Kang, J. Park, U. Koldemir, J. Suh, D. S. Narang, K. Liu, J. Ji, J. Li, R. Sinclair, and J. Wu, "Tuning interlayer coupling in large-area heterostructures with CVD-grown MoS2and WS2monolayers," *Nano Letters*, vol. 14, no. 6, pp. 3185–3190, 2014. [Online]. Available: https://doi.org/10.1021/nl500515q

[92] K. Garay-Palmett, D. Cruz-Delgado, F. Dominguez-Serna, E. Ortiz-Ricardo, J. Monroy-Ruz, H. Cruz-Ramirez, R. Ramirez-Alarcon, and A. B. U'Ren, "Photon-pair generation by intermodal spontaneous four-wave mixing in birefringent, weakly guiding optical fibers," *Physical Review A*, vol. 93, no. 3, 2016. [Online]. Available: http://dx.doi.org/10.1103/PhysRevA.93.033810

[93] S. F. Preble, M. L. Fanto, J. A. Steidle, C. C. Tison, G. A. Howland, Z. Wang, and P. M. Alsing, "On-chip quantum interference from a single silicon ring-resonator source," *Physical Review Applied*, vol. 4, no. 2, pp. 1–5, 2015. [Online]. Available: http://dx.doi.org/10.1103/PhysRevApplied.4.021001

[94] J. B. Spring, P. L. Mennea, B. J. Metcalf, P. C. Humphreys, J. C. Gates, H. L. Rogers, C. Söller, B. J. Smith, W. S. Kolthammer, P. G. R. Smith, and I. A. Walmsley, "Chip-based array of near-identical, pure, heralded single-photon sources," *Optica*, vol. 4, no. 1, pp. 90–96, 2017. [Online]. Available: http://dx.doi.org/10.1364/OPTICA.4.000090

[95] K. Heshami, D. G. England, P. C. Humphreys, P. J. Bustard, V. M. Acosta, J. Nunn, and B. J. Sussman, "Quantum memories: emerging applications and recent advances," *Journal of Modern Optics*, vol. 63, no. 20, pp. 2005–2028, 2016. [Online]. Available: https://dx.doi.org/10.1080/09500340.2016.1148212

[96] M. Davanço, C. S. Hellberg, S. Ates, A. Badolato, and K. Srinivasan, "Multiple time scale blinking in InAs quantum dot single-photon sources," *Physical Review B*, vol. 89, no. 16, pp. 1–8, 2014. [Online]. Available: http://dx.doi.org/10.1103/PhysRevB.89.161303

[97] T. Li, Q. Wang, X. Guo, Z. Jia, P. Wang, X. Ren, Y. Huang, and S. Cai, "The saturation density property of (B)InAs/GaAs quantum dots

grown by metal-organic chemical vapor deposition," *Physica E: Low-Dimensional Systems and Nanostructures*, vol. 44, no. 7-8, pp. 1146–1151, 2012. [Online]. Available: http://dx.doi.org/10.1016/j.physe.2012.01.002

[98] H. S. Lee, J. Y. Lee, T. W. Kim, and M. D. Kim, "Strain effects in and crystal structures of self-assembled InAs/GaAs quantum dots," *Applied Physics Letters*, vol. 83, no. 11, pp. 2256–2258, 2003. [Online]. Available: http://dx.doi.org/10.1063/1.1612894

[99] J. M. Moison, F. Houzay, F. Barthe, L. Leprince, E. André, and O. Vatel, "Self-organized growth of regular nanometer-scale InAs dots on GaAs," *Applied Physics Letters*, vol. 64, no. 2, pp. 196–198, 1994. [Online]. Available: http://dx.doi.org/10.1063/1.111502

[100] R. Ohtsubo and K. Yamaguchi, "High quality InAs quantum dots covered by InGaAs/GaAs hetero-capping layer," *Physica Status Solidi C: Conferences*, vol. 943, no. 3, pp. 939–943, 2003. [Online]. Available: http://dx.doi.org/10.1002/pssc.200306247

[101] R. Nötzel, "Self-organized growth of quantum-dot structures," *Semiconductor Science and Technology*, vol. 11, no. 10, pp. 1365–1379, 1996. [Online]. Available: http://dx.doi.org/10.1088/0268-1242/11/10/004

[102] L. Jacak, "Semiconductor quantum dots - towards a new generation of semiconductor devices," *European Journal of Physics*, vol. 21, no. 6, pp. 487–497, nov 2000. [Online]. Available: http://dx.doi.org/10.1088/0143-0807/21/6/301

[103] C. J. Mayer, M. F. Helfrich, and D. M. Schaadt, "Influence of hole shape/size on the growth of site-selective quantum dots," *Nanoscale Research Letters*, vol. 8, no. 1, pp. 1–7, 2013. [Online]. Available: https://doi.org/10.1186/1556-276X-8-504

[104] J. Skiba-Szymanska, A. Jamil, I. Farrer, M. B. Ward, C. A. Nicoll, D. J. P. Ellis, J. P. Griffiths, D. Anderson, G. A. C. Jones, D. A. Ritchie, and A. J. Shields, "Narrow emission linewidths of positioned InAs quantum dots grown on pre-patterned GaAs(100) substrates." *Nanotechnology*, vol. 22, no. 6, p. 065302, 2011. [Online]. Available: http://dx.doi.org/10.1088/0957-4484/22/6/065302

[105] S. Reitzenstein, C. Hofmann, A. Gorbunov, M. Strauß, S. H. Kwon, C. Schneider, A. Löffler, S. Höfling, M. Kamp, and A. Forchel, "AIAs/GaAs micropillar cavities with quality factors exceeding 150.000," *Applied Physics Letters*, vol. 90, no. 25, pp. 5–7, 2007. [Online]. Available: https://doi.org/10.1063/1.2749862

[106] K. D. Jöns, P. Atkinson, M. Müller, M. Heldmaier, S. M. Ulrich, O. G. Schmidt, and P. Michler, "Triggered indistinguishable single photons with narrow line widths from site-controlled quantum dots," *Nano Letters*, vol. 13, no. 1, pp. 126–130, 2013. [Online]. Available: http://dx.doi.org/10.1021/nl303668z

[107] J. Zhang, S. Lu, S. Chattaraj, and A. Madhukar, "Triggered single photon emission up to 77K from ordered array of surface curvature-directed mesa-top GaAs/InGaAs single quantum dots," *Optics Express*, vol. 24, no. 26, p. 29955, dec 2016. [Online]. Available: http://dx.doi.org/10.1364/OE.24.029955

[108] J. M. Pietryga, Y. S. Park, J. Lim, A. F. Fidler, W. K. Bae, S. Brovelli, and V. I. Klimov, "Spectroscopic and device aspects of nanocrystal quantum dots," *Chemical Reviews*, vol. 116, no. 18, pp. 10 513–10 622, 2016. [Online]. Available: https://dx.doi.org/10.1021/acs.chemrev.6b00169

[109] B. Lounis, H. Bechtel, D. Gerion, P. Alivisatos, and W. Moerner, "Photon antibunching in single CdSe/ZnS quantum dot fluorescence," *Chemical Physics Letters*, vol. 329, no. 5-6, pp. 399–404, 2000. [Online]. Available: http://dx.doi.org/10.1016/S0009-2614(00)01042-3

[110] B. O. Dabbousi, J. Rodriguez-Viejo, F. V. Mikulec, J. R. Heine, H. Mattoussi, R. Ober, K. F. Jensen, and M. G. Bawendi, "(CdSe)ZnS CoreShell Quantum Dots: Synthesis and Characterization of a Size Series of Highly Luminescent Nanocrystallites," *The Journal of Physical Chemistry B*, vol. 101, no. 46, pp. 9463–9475, 1997. [Online]. Available: http://dx.doi.org/10.1021/jp971091y

[111] I. L. Medintz, H. T. Uyeda, E. R. Goldman, and H. Mattoussi, "Quantum dot bioconjugates for imaging, labelling and sensing." *Nature Materials*, vol. 4, no. 6, pp. 435–446, 2005. [Online]. Available: http://dx.doi.org/10.1038/nmat1390

[112] M. Pelton, "Modified spontaneous emission in nanophotonic structures," *Nature Photonics*, vol. 9, no. 7, pp. 427–435, 2015. [Online]. Available: http://dx.doi.org/10.1038/nphoton.2015.103

[113] E. M. Purcell, "Spontaneous Emission Probabliities at Radio Frquencies," *Physical Review*, vol. 69, p. 681, 1946. [Online]. Available: http://dx.doi.org/10.1103/PhysRev.69.674.2

[114] K. J. Vahala, "Optical Microcavities," *Nature*, vol. 424, no. August, pp. 839–846, 2005. [Online]. Available: https://doi.org/10.1038/nature01939

[115] S. Reitzenstein and A. Forchel, "Quantum dot micropillars," *Journal of Physics D: Applied Physics*, vol. 43, no. 3, p. 033001, 2010. [Online]. Available: https://doi.org/10.1088/0022-3727/43/3/033001

[116] P. Michler, A. Kiraz, C. Becher, W. V. Schoenfeld, P. M. Petroff, L. Zhang, E. Hu, and A. Imamolu, "A quantum dot single-photon turnstile device." *Science*, vol. 290, no. 5500, pp. 2282–2285, 2000. [Online]. Available: http://dx.doi.org/10.1126/science.290.5500.2282

[117] Y. Akahane, T. Asano, B.-s. Song, and S. Noda, "High- Q photonic nanocavity in a two-dimensional photonic crystal," *Nature*, vol. 425, no. October, pp. 944–947, 2003. [Online]. Available: http://dx.doi.org/10.1038/nature02063

[118] J. Joannopoulos, S. G. Johson, R. Meade, and J. Winn, *Photonic Crystals: Molding the Flow of Light (Second Edition)*. Princeton University Press, 2008.

[119] Rayleigh, "On the remarkable phenomenon of crystalline reflexion described by Prof. Stokes," *The London, Edinburgh, and Dublin Philosophical Magazine and Journal of Science*, vol. 26, no. 160, pp. 256–265, sep 1888. [Online]. Available: https://doi.org/10.1080/14786448808628259

[120] E. Yablonovitch, T. J. Gmitter, and K. M. Leung, "Photonic band structure: The face-centered-cubic case employing nonspherical atoms," *Physical Review Letters*, vol. 67, no. 17, pp. 2295–2298, 1991. [Online]. Available: https://doi.org/10.1103/PhysRevLett.67.2295

[121] T. F. Krauss, R. M. D. L. Rue, and S. Brand, "Two-dimensional photonic-bandgap structures operating at near-infrared wavelengths," *Nature*, vol. 383, no. 6602, pp. 699–702, oct 1996. [Online]. Available: https://doi.org/10.1038/383699a0

[122] S. Fan, P. R. Villeneuve, R. D. Meade, and J. D. Joannopoulos, "Design of threedimensional photonic crystals at submicron lengthscales," *Applied Physics Letters*, vol. 65, no. 11, pp. 1466–1468, sep 1994. [Online]. Available: http://dx.doi.org/10.1063/1.112017

[123] R. Kubrin, R. M. Pasquarelli, M. Waleczek, H. S. Lee, R. Zierold, J. J. Do Rosário, P. N. Dyachenko, J. M. Montero Moreno, A. Y. Petrov, R. Janssen, M. Eich, K. Nielsch, and G. A. Schneider, "Bottom-up Fabrication of Multilayer Stacks of 3D Photonic Crystals from Titanium Dioxide," *ACS Applied Materials and Interfaces*, vol. 8, no. 16, pp. 10 466–10 476, 2016. [Online]. Available: http://dx.doi.org/10.1021/acsami.6b00827

[124] K. Kitano, K. Suzuki, K. Ishizaki, and S. Noda, "Three-dimensional photonic crystals fabricated by simultaneous multidirectional etching," *Physical Review B - Condensed Matter and Materials Physics*, vol. 91, no. 15, pp. 1–10, 2015. [Online]. Available: http://dx.doi.org/10.1103/PhysRevB.91.155308

[125] T. Crane, O. J. Trojak, J. P. Vasco, S. Hughes, and L. Sapienza, "Anderson Localization of Visible Light on a Nanophotonic Chip," *ACS Photonics*, vol. 4, no. 9, pp. 2274–2280, sep 2017. [Online]. Available: https://doi.org/10.1021/acsphotonics.7b00517

[126] M. Kitamura, S. Iwamoto, and Y. Arakawa, "Enhanced light emission from an organic photonic crystal with a nanocavity," *Applied Physics Letters*, vol. 87, no. 15, pp. 1–3, 2005. [Online]. Available: http://dx.doi.org/10.1063/1.2103404

[127] N. Jiang, X. Zhuo, and J. Wang, "Active Plasmonics: Principles, Structures, and Applications," *Chemical Reviews*, p. acs.chemrev.7b00252, 2017. [Online]. Available: http://dx.doi.org/10.1021/acs.chemrev.7b00252

[128] A. Kinkhabwala, Z. Yu, S. Fan, Y. Avlasevich, K. Müllen, and W. E. Moerner, "Large single-molecule fluorescence enhancements produced by a bowtie nanoantenna," *Nature Photonics*, vol. 3, no. 11, pp. 654–657, 2009. [Online]. Available: https://doi.org/10.1038/nphoton.2009.187

[129] R. Adato, S. Aksu, and H. Altug, "Engineering mid-infrared nanoantennas for surface enhanced infrared absorption spectroscopy," *Materials Today*, vol. 18, no. 8, pp. 436–446, 2015. [Online]. Available: http://dx.doi.org/10.1016/j.mattod.2015.03.001

[130] E. B. Ureña, M. P. Kreuzer, S. Itzhakov, H. Rigneault, R. Quidant, D. Oron, and J. Wenger, "Excitation enhancement of a quantum dot coupled to a plasmonic antenna," *Advanced Materials*, vol. 24, no. 44, pp. 314–320, 2012. [Online]. Available: https://doi.org/10.1002/adma.201202783

[131] F. Monticone and A. Alu, "Metamaterial, plasmonic and nanophotonic devices," *Reports on Progress in Physics*, vol. 80, no. 3, 2017. [Online]. Available: http://dx.doi.org/10.1088/1361-6633/aa518f

[132] C. F. Wang, A. Badolato, I. Wilson-Rae, P. M. Petroff, E. Hu, J. Urayama, and A. Imamolu, "Optical properties of single InAs quantum dots in close proximity to surfaces," *Applied Physics Letters*, vol. 85, no. 16, pp. 3423–3425, 2004. [Online]. Available: https://dx.doi.org/10.1063/1.1806251

[133] B. Ai, Y. Yu, H. Möhwald, G. Zhang, and B. Yang, "Plasmonic films based on colloidal lithography," *Advances in Colloid and Interface Science*, vol. 206, pp. 5–16, 2014. [Online]. Available: http://dx.doi.org/10.1016/j.cis.2013.11.010

[134] T. Li and F.-G. Deng, "Heralded high-efficiency quantum repeater with atomic ensembles assisted by faithful single-photon transmission," *Scientific Reports*, vol. 5, no. October, p. 15610, 2015. [Online]. Available: https://doi.org/10.1038/srep15610

[135] L. Bocquet and E. Charlaix, "Nanofluidics, from bulk to interfaces," *Chem. Soc. Rev.*, vol. 39, no. 3, pp. 1073–1095, 2010. [Online]. Available: http://dx.doi.org/10.1039/B909366B

[136] T. Yoshie, A. Scherer, J. Hendrickson, G. Khitrova, H. M. Gibbs, G. Rupper, C. Ell, O. B. Shchekin, and D. G. Deppe, "Vacuum Rabi splitting with a single quantum dot in a photonic crystal nanocavity," *Nature*, vol. 432, no. 7014, pp. 200–203, 2004. [Online]. Available: https://doi.org/10.1038/nature03119

[137] K. Hennessy, A. Badolato, M. Winger, D. Gerace, M. Atat Uuml Re, S. Gulde, S. F Auml Lt, E. L. Hu, and A. Imamo Gbreve Lu, "Quantum nature of a strongly coupled single quantum dot-cavity system," *Nature*, vol. 445, no. 7130, p. 896, 2007. [Online]. Available: http://dx.doi.org/10.1038/nature05586

[138] S. M. Thon, M. T. Rakher, H. Kim, J. Gudat, W. T. M. Irvine, P. M. Petroff, and D. Bouwmeester, "Strong coupling through optical positioning of a quantum dot in a photonic crystal cavity," *Applied Physics Letters*, vol. 94, no. 11, pp. 2–4, 2009. [Online]. Available: https://doi.org/10.1063/1.3103885

[139] A. Dousse, L. Lanco, J. Suffczynski, E. Semenova, A. Miard, A. Lemaître, I. Sagnes, C. Roblin, J. Bloch, and P. Senellart, "Controlled light-matter coupling for a single quantum dot embedded in a pillar microcavity using far-field optical lithography," *Physical Review Letters*, vol. 101, no. 26, pp. 30–33, 2008. [Online]. Available: https://doi.org/10.1103/PhysRevLett.101.267404

[140] T. Kojima, K. Kojima, T. Asano, and S. Noda, "Accurate alignment of a photonic crystal nanocavity with an embedded quantum dot based on optical microscopic photoluminescence imaging," *Applied Physics Letters*, vol. 102, no. 1, p. 011110, jan 2013. [Online]. Available: https://doi.org/10.1063/1.4773882

[141] M. Gschrey, F. Gericke, A. Schüßler, R. Schmidt, J. H. Schulze, T. Heindel, S. Rodt, A. Strittmatter, and S. Reitzenstein, "In situ electron-beam lithography of deterministic single-quantum-dot mesa-structures using low-temperature cathodoluminescence spectroscopy," *Applied Physics Letters*, vol. 102, no. 25, pp. 1–4, 2013. [Online]. Available: https://doi.org/10.1063/1.4812343

[142] J. Liu, M. Davanço, L. Sapienza, K. Konthasinghe, J. V. D. M. Cardoso, J. D. Song, A. Badolato, and K. Srinivasan, "Cryogenic photoluminescence imaging system for nanoscale positioning of single quantum emitters," *Review of Scientific Instruments*, vol. 88, p. 023116, dec 2017. [Online]. Available: http://dx.doi.org/10.1063/1.4976578

[143] N. Somaschi, V. Giesz, L. De Santis, J. C. Loredo, M. P. Almeida, G. Hornecker, S. L. Portalupi, T. Grange, C. Anton, J. Demory, C. Gomez, I. Sagnes, N. D. L. Kimura, A. Lemaître, A. Auffeves, A. G. White, L. Lanco, and P. Senellart, "Near optimal single photon sources in the solid state," *Nature Photonics*, vol. 10, no. 2, pp. 1–6, 2016. [Online]. Available: https://doi.org/10.1038/nphoton.2016.23

[144] Y.-M. He, Y. He, Y.-J. Wei, D. Wu, M. Atatüre, C. Schneider, S. Höfling, M. Kamp, C.-Y. Lu, and J.-W. Pan, "On-demand semiconductor single-photon source with near-unity indistinguishability," *Nature Nanotechnology*, vol. 8, no. 3, pp. 213–217, 2013. [Online]. Available: https://doi.org/10.1038/nnano.2012.262

[145] O. Gazzano, S. Michaelis de Vasconcellos, C. Arnold, A. Nowak, E. Galopin, I. Sagnes, L. Lanco, A. Lemaître, and P. Senellart, "Bright solid-state sources of indistinguishable single photons." *Nature Communications*, vol. 4, no. Feb, p. 1425, 2013. [Online]. Available: https://doi.org/10.1038/ncomms2434

[146] M. E. Reimer, G. Bulgarini, N. Akopian, M. Hocevar, M. B. Bavinck, M. A. Verheijen, E. P. A. M. Bakkers, L. P. Kouwenhoven,

and V. Zwiller, "Bright single-photon sources in bottom-up tailored nanowires." *Nature Communications*, vol. 3, p. 737, 2012. [Online]. Available: https://doi.org/10.1038/ncomms1746

[147] M. Davanço, M. T. Rakher, D. Schuh, A. Badolato, and K. Srinivasan, "A circular dielectric grating for vertical extraction of single quantum dot emission," *Applied Physics Letters*, vol. 99, no. 4, p. 041102, 2011. [Online]. Available: https://doi.org/10.1063/1.3615051

[148] O. J. Trojak, S. I. Park, J. D. Song, and L. Sapienza, "Metallic nanorings for broadband, enhanced extraction of light from solid-state emitters," *Applied Physics Letters*, vol. 111, no. 2, p. 021109, 2017. [Online]. Available: https://doi.org/10.1063/1.4993774

[149] O. J. Trojak, C. Woodhead, S.-I. Park, J. D. Song, R. J. Young, and L. Sapienza, "Combined metallic nano-rings and solid-immersion lenses for bright emission from single InAs/GaAs quantum dots," *Applied Physics Letters*, vol. 112, no. 22, p. 221102, 2018. [Online]. Available: https://doi.org/10.1063/1.5023207

[150] C. F. Madigan, M.-H. Lu, and J. C. Sturm, "Improvement of output coupling efficiency of organic light-emitting diodes by backside substrate modification," *Applied Physics Letters*, vol. 76, no. 13, pp. 1650–1652, mar 2000. [Online]. Available: https://doi.org/10.1063/1.126124

[151] M. C. Huang, Y. Zhou, and C. J. Chang-Hasnain, "A surface-emitting laser incorporating a high-index-contrast subwavelength grating," *Nature Photonics*, vol. 1, no. 5, pp. 297–297, 2007. [Online]. Available: http://dx.doi.org/10.1038/nphoton.2007.73

[152] O. Gazzano and G. S. Solomon, "Toward optical quantum information processing with quantum dots coupled to microstructures," *Journal of the Optical Society of America B*, vol. 33, no. 7, pp. C160–C175, 2016. [Online]. Available: http://dx.doi.org/10.1364/JOSAB.33.00C160

[153] I. Aharonovich, D. Englund, and M. Toth, "Solid-state single-photon emitters," *Nature Photonics*, vol. 10, no. 10, pp. 631–641, 2016. [Online]. Available: http://dx.doi.org/10.1038/nphoton.2016.186

[154] J. L. O'Brien, A. Furusawa, and J. Vučković, "Photonic quantum technologies," *Nature Photonics*, vol. 3, no. 12, pp. 687–695, 2009. [Online]. Available: https://doi.org/10.1038/nphoton.2009.229

[155] A. V. Kuhlmann, J. H. Prechtel, J. Houel, A. Ludwig, D. Reuter, A. D. Wieck, and R. J. Warburton, "Transform-limited single photons from a single quantum dot," *Nature Communications*, vol. 6, p. 8204, 2015. [Online]. Available: http://dx.doi.org/10.1038/ncomms9204

[156] C. Schneider, P. Gold, S. Reitzenstein, S. Höfling, and M. Kamp, "Quantum dot micropillar cavities with quality factors exceeding 250,000," *Applied Physics B: Lasers and Optics*, vol. 122, no. 1, pp. 1–6, 2016. [Online]. Available: http://dx.doi.org/10.1007/s00340-015-6283-x

[157] P. Senellart, G. Solomon, and A. White, "High-performance semiconductor quantum-dot single-photon sources," *Nature Nanotechnology*, vol. 12, no. 11, pp. 1026–1039, 2017. [Online]. Available: http://dx.doi.org/10.1038/nnano.2017.218

[158] J. Liu, K. Konthasinghe, M. Davanco, J. Lawall, V. Anant, V. Verma, R. Mirin, S. W. Nam, J. D. Song, B. Ma, Z. S. Chen, H. Q. Ni, Z. C. Niu, and K. Srinivasan, "Direct observation of nanofabrication influence on the optical properties of single self-assembled InAs/GaAs quantum dots," pp. 1–11, 2017. [Online]. Available: http://arxiv.org/abs/1710.09667

[159] J. Claudon, J. Bleuse, N. S. Malik, M. Bazin, P. Jaffrennou, N. Gregersen, C. Sauvan, P. Lalanne, and J.-M. Gérard, "A highly efficient single-photon source based on a quantum dot in a photonic nanowire," *Nature Photonics*, vol. 4, no. March, pp. 174–177, 2010. [Online]. Available: http://dx.doi.org/10.1038/nphoton.2009.287

[160] M. Munsch, N. S. Malik, E. Dupuy, A. Delga, J. Bleuse, J.-M. Gérard, J. Claudon, N. Gregersen, and J. Mørk, "Dielectric GaAs antenna ensuring an efficient broadband coupling between an inas quantum dot and a gaussian optical beam," *Physical Review Letters*, vol. 110, no. 17, pp. 1–5, 2013. [Online]. Available: http://dx.doi.org/10.1103/PhysRevLett.110.177402

[161] S. Ates, L. Sapienza, M. Davanco, A. Badolato, and K. Srinivasan, "Bright Single-Photon Emission From a Quantum Dot in a Circular Bragg Grating Microcavity," *IEEE Journal of Selected Topics in Quantum Electronics*, vol. 18, no. 6, pp. 1711–1721, nov 2012. [Online]. Available: http://dx.doi.org/10.1109/JSTQE.2012.2193877

[162] "Lumerical FDTD, Lumeriucal Solutions Inc." http://www.lumerical.com/tcad-products/fdtd/.

[163] J. Vancea, G. Reiss, F. Schneider, K. Bauer, and H. Hoffmann, "Substrate effects on the surface topography of evaporated gold filmsA scanning tunnelling microscopy investigation," *Surface Science*, vol. 218, no. 1, pp. 108–126, aug 1989. [Online]. Available: http://dx.doi.org/10.1016/0039-6028(89)90622-5

[164] J. Kennedy and R. Eberhart, "Particle swarm optimization," *Neural Networks, 1995. Proceedings., IEEE International Conference on*, vol. 4, pp. 1942–1948 vol.4, 1995.

[165] "NANO PMMA and Copolymer," MicroChem Corp., Tech. Rep., 2001. [Online]. Available: http://microchem.com/Prod-PMMA

[166] D. Lide, *CRC Handbook of Chemistry and Physics 86th Edition.* Boca Raton: CRC Press, 2005.

[167] J.-H. Kim, T. Cai, C. J. K. Richardson, R. P. Leavitt, and E. Waks, "Two-photon interference from a bright single-photon source at telecom wavelengths," *Optica*, vol. 3, no. 6, p. 577, 2016. [Online]. Available: http://dx.doi.org/10.1364/OPTICA.3.000577

[168] M. Sartison, S. L. Portalupi, T. Gissibl, M. Jetter, H. Giessen, and P. Michler, "Combining in-situ lithography with 3D printed solid immersion lenses for single quantum dot spectroscopy," *Scientific Reports*, vol. 7, no. August 2016, p. 39916, 2017. [Online]. Available: http://dx.doi.org/10.1038/srep39916

[169] A. Hartmann, Y. Ducommun, E. Kapon, U. Hohenester, and E. Molinari, "Few-Particle Effects in Semiconductor Quantum Dots: Observation of Multicharged Excitons," *Physical Review Letters*, vol. 84, no. 24, pp. 5648–5651, jun 2000. [Online]. Available: http://dx.doi.org/10.1103/PhysRevLett.84.5648

[170] M. Li, J. Wang, L. Zhuang, and S. Y. Chou, "Fabrication of circular optical structures with a 20 nm minimum feature size using nanoimprint lithography," *Applied Physics Letters*, vol. 76, no. 6, p. 673, 2000. [Online]. Available: http://dx.doi.org/10.1063/1.125896

[171] R. J. Warburton, C. Schulhauser, D. Haft, C. Schäflein, K. Karrai, J. M. Garcia, W. Schoenfeld, and P. M. Petroff, "Giant permanent dipole moments of excitons in semiconductor nanostructures," *Physical Review B*, vol. 65, no. 11, p. 113303, feb 2002. [Online]. Available: http://dx.doi.org/10.1103/PhysRevB.65.113303

[172] M. J. Conterio, N. Sköld, D. J. Ellis, I. Farrer, D. A. Ritchie, and A. J. Shields, "A quantum dot single photon source driven by resonant electrical injection," *Applied Physics Letters*, vol. 103, no. 16, pp. 1–4, 2013. [Online]. Available: http://dx.doi.org/10.1063/1.4825208

[173] K. A. Serrels, E. Ramsay, P. A. Dalgarno, B. D. Gerardot, J. A. O'Connor, R. H. Hadfield, R. J. Warburton, and D. T. Reid, "Solid immersion lens applications for nanophotonic devices," *Journal of Nanophotonics*, vol. 2, no. 1, p. 021854, 2008. [Online]. Available: http://dx.doi.org/10.1117/1.3068652

[174] M. Gschrey, A. Thoma, P. Schnauber, M. Seifried, R. Schmidt, B. Wohlfeil, L. Krüger, J.-H. Schulze, T. Heindel, S. Burger, F. Schmidt, A. Strittmatter, S. Rodt, and S. Reitzenstein, "Highly indistinguishable photons from deterministic quantum-dot microlenses utilizing three-dimensional in situ electron-beam lithography." *Nature Communications*, vol. 6, no. May, p. 7662, 2015. [Online]. Available: http://dx.doi.org/10.1038/ncomms8662

[175] F. Mugele and J. C. Baret, "Electrowetting: From basics to applications," *Journal of Physics Condensed Matter*, vol. 17, no. 28, 2005. [Online]. Available: http://dx.doi.org/10.1088/0953-8984/17/28/R01

[176] B. Born, E. L. Landry, and J. F. Holzman, "Electrodispensing of Microspheroids for Lateral Refractive and Reflective Photonic Elements," *IEEE Photonics Journal*, vol. 2, no. 6, pp. 873–883, 2010. [Online]. Available: http://dx.doi.org/10.1109/JPHOT.2010.2076800

[177] C. C. Lee, S. Y. Hsiao, and W. Fang, "Microlens formation technology utilizing multi-phase liquid ambiance," *TRANSDUCERS*

2009 - 15th International Conference on Solid-State Sensors, Actuators and Microsystems, pp. 2086–2089, 2009. [Online]. Available: http://dx.doi.org/10.1109/SENSOR.2009.5285646

[178] C. S. Woodhead, J. Roberts, Y. J. Noori, Y. Cao, R. Bernardo-Gavito, P. Tovee, A. Kozikov, K. Novoselov, and R. J. Young, "Increasing the light extraction and longevity of TMDC monolayers using liquid formed micro-lenses," *2D Materials*, vol. 4, no. 1, p. 015032, 2016. [Online]. Available: https://doi.org/10.1088/2053-1583/4/1/015032

[179] O. L. Muskens, V. Giannini, J. A. Sánchez-Gil, and J. Gómez Rivas, "Strong enhancement of the radiative decay rate of emitters by single plasmonic nanoantennas," *Nano Letters*, vol. 7, no. 9, pp. 2871–2875, 2007. [Online]. Available: https://doi.org/10.1021/nl0715847

[180] C. Santori, D. Fattal, J. Vucković, G. S. Solomon, and Y. Yamamoto, "Indistinguishable photons from a single-photon device." *Nature*, vol. 419, no. 6907, pp. 594–597, 2002. [Online]. Available: https://doi.org/10.1109/QELS.2003.1276041

[181] M. Pfeiffer, K. Lindfors, C. Wolpert, P. Atkinson, M. Benyoucef, A. Rastelli, O. G. Schmidt, H. Giessen, and M. Lippitz, "Enhancing the optical excitation efficiency of a single self-assembled quantum dot with a plasmonic nanoantenna," *Nano Letters*, vol. 10, no. 11, pp. 4555–4558, 2010. [Online]. Available: https://doi.org/10.1021/nl102548t

[182] S. I. Park, O. J. Trojak, E. Lee, J. D. Song, J. Kyhm, I. Han, J. Kim, G.-C. Yi, and L. Sapienza, "GaAs droplet quantum dots with nanometer-thin capping layer for plasmonic applications," *Nanotechnology*, vol. 29, no. 20, p. 205602, 2018. [Online]. Available: https://doi.org/10.1088/1361-6528/aab2e1

[183] T. H. Taminiau, F. D. Stefani, F. B. Segerink, and N. F. Van Hulst, "Optical antennas direct single-molecule emission," *Nature Photonics*, vol. 2, no. 4, pp. 234–237, 2008. [Online]. Available: https://dx.doi.org/10.1038/nphoton.2008.32

[184] R. Zia, J. A. Schuller, A. Chandran, and M. L. Brongersma, "Plasmonics: the next chip-scale technology," *Materials Today*, vol. 9, no. 7-8, pp. 20–27, 2006. [Online]. Available: https://doi.org/10.1016/S1369-7021(06)71572-3

[185] J. A. Schuller, E. S. Barnard, W. Cai, Y. C. Jun, J. S. White, and M. L. Brongersma, "Plasmonics for extreme light concentration and manipulation," *Nature Materials*, vol. 9, no. 3, pp. 193–204, 2010. [Online]. Available: http://dx.doi.org/10.1038/nmat2630

[186] D. P. Fromm, A. Sundaramurthy, P. James Schuck, G. Kino, and W. E. Moerner, "Gap-dependent optical coupling of single "bowtie" nanoantennas resonant in the visible," *Nano Letters*, vol. 4, no. 5, pp. 957–961, 2004. [Online]. Available: https://doi.org/10.1021/nl049951r

[187] A. A. Lyamkina, K. Schraml, A. Regler, M. Schalk, A. K. Bakarov, A. I. Toropov, S. P. Moshchenko, and M. Kaniber, "Monolithically integrated single quantum dots coupled to bowtie nanoantennas," *Optics Express*, vol. 24, no. 25, p. 28936, dec 2016. [Online]. Available: http://dx.doi.org/10.1364/OE.24.028936

[188] T. B. Hoang, G. M. Akselrod, and M. H. Mikkelsen, "Ultrafast Room-Temperature Single Photon Emission from Quantum Dots Coupled to Plasmonic Nanocavities," *Nano Letters*, vol. 16, no. 1, pp. 270–275, 2016. [Online]. Available: http://dx.doi.org/10.1021/acs.nanolett.5b03724

[189] G. M. Akselrod, C. Argyropoulos, T. B. Hoang, C. Ciracì, C. Fang, J. Huang, D. R. Smith, and M. H. Mikkelsen, "Probing the mechanisms of large Purcell enhancement in plasmonic nanoantennas," *Nature Photonics*, vol. 8, no. 11, pp. 835–840, 2014. [Online]. Available: http://dx.doi.org/10.1038/nphoton.2014.228

[190] Z. M. Wang, B. L. Liang, K. A. Sablon, and G. J. Salamo, "Nanoholes fabricated by self-assembled gallium nanodrill on GaAs(100)," *Applied Physics Letters*, vol. 90, no. 11, pp. 2006–2008, 2007. [Online]. Available: https://doi.org/10.1063/1.2713745

[191] C. Heyn, M. Zocher, L. Pudewill, H. Runge, A. Küster, and W. Hansen, "Droplet etched GaAs quantum dots close to surfaces and metallic interfaces," *Journal of Applied Physics*, vol. 121, no. 4, pp. 1–6, 2017. [Online]. Available: https://doi.org/10.1063/1.4974965

[192] H. Zhang, Y. Huo, K. Lindfors, Y. Chen, O. G. Schmidt, A. Rastelli, and M. Lippitz, "Narrow-line self-assembled GaAs quantum dots for plasmonics," *Applied Physics Letters*, vol. 106, no. 10, pp. 1–4, 2015. [Online]. Available: http://dx.doi.org/10.1063/1.4914387

[193] P. Atkinson, E. Zallo, and O. G. Schmidt, "Independent wavelength and density control of uniform GaAs/AlGaAs quantum dots grown by infilling self-assembled nanoholes," *Journal of Applied Physics*, vol. 112, no. 5, p. 054303, sep 2012. [Online]. Available: https://doi.org/10.1063/1.4748183

[194] N. Koguchi and K. Ishige, "Growth of gaas epitaxial microcrystals on an s-terminated gaas substrate by successive irradiation of ga and as molecular beams," *Japanese Journal of Applied Physics*, vol. 32, no. 5 R, pp. 2052–2058, 1993. [Online]. Available: https://doi.org/10.1143/JJAP.32.2052

[195] M. Jo, T. Mano, Y. Sakuma, and K. Sakoda, "Extremely high-density GaAs quantum dots grown by droplet epitaxy," *Applied Physics Letters*, vol. 100, no. 21, p. 212113, may 2012. [Online]. Available: https://doi.org/10.1063/1.4721663

[196] T. Mano, M. Abbarchi, T. Kuroda, C. A. Mastrandrea, A. Vinattieri, S. Sanguinetti, K. Sakoda, and M. Gurioli, "Ultra-narrow emission from single GaAs self-assembled quantum dots grown by droplet epitaxy," *Nanotechnology*, vol. 20, no. 39, 2009. [Online]. Available: https://doi.org/10.1088/0957-4484/20/39/395601

[197] T. Mano, T. Kuroda, K. Kuroda, and K. Sakoda, "Self-assembly of quantum dots and rings by droplet epitaxy and their optical properties," *Journal of Nanophotonics*, vol. 3, no. 1, p. 031605, 2009. [Online]. Available: https://doi.org/10.1117/1.3085991

[198] W. Jevasuwan, S. Ratanathammapan, and S. Panyakeow, "InP Ring-Shaped Quantum Dot Molecules by Droplet Epitaxy," in *Quantum Dot Molecules. Lecture Notes in Nanoscale Science and Technology*, J. Wu and Z. M. Wang, Eds. New York: Springer, 2014, vol. 14, ch. 2, pp. 29–49. [Online]. Available: https://doi.org/10.1007/978-1-4614-8130-0{_}2

[199] T. Mano, T. Kuroda, S. Sanguinetti, T. Ochiai, T. Tateno, J. Kim, T. Noda, M. Kawabe, K. Sakoda, G. Kido, and N. Koguchi, "Self-assembly of concentric quantum double rings," *Nano Letters*, vol. 5, no. 3, pp. 425–428, 2005. [Online]. Available: https://dx.doi.org/10.1021/nl048192

[200] M. Jo, T. Mano, and K. Sakoda, "Morphological control of GaAs quantum dots grown by droplet epitaxy using a thin AlGaAs capping layer," *Journal of Applied Physics*, vol. 108, no. 8, p. 083505, oct 2010. [Online]. Available: http://dx.doi.org/10.1063/1.3493262

[201] I. Favero, G. Cassabois, R. Ferreira, D. Darson, C. Voisin, J. Tignon, C. Delalande, G. Bastard, P. Roussignol, and J. M. Gérard, "Acoustic phonon sidebands in the emission line of single InAs/GaAs quantum dots," *Physical Review B - Condensed Matter and Materials Physics*, vol. 68, no. 23, pp. 68–71, 2003. [Online]. Available: https://dx.doi.org/10.1103/PhysRevB.68.233301

[202] M. Barth, J. Kouba, J. Stingl, B. Löchel, and O. Benson, "Modification of visible spontaneous emission with silicon nitride photonic crystal nanocavities," *Optics Express*, vol. 15, no. 25, p. 17231, 2007. [Online]. Available: http://dx.doi.org/10.1364/OE.15.017231

[203] Y. Lai, S. Pirotta, G. Urbinati, D. Gerace, M. Minkov, V. Savona, A. Badolato, and M. Galli, "Genetically designed L3 photonic crystal nanocavities with measured quality factor exceeding one million," *Applied Physics Letters*, vol. 104, no. 24, p. 241101, jun 2014. [Online]. Available: http://dx.doi.org/10.1063/1.4882860

[204] H. Sekoguchi, Y. Takahashi, T. Asano, and S. Noda, "Photonic crystal nanocavity with a Q-factor of 9 million," *Optics Express*, vol. 22, no. 1, pp. 916–924, 2014. [Online]. Available: http://dx.doi.org/10.1364/OE.22.000916

[205] M. M. Murshidy, A. M. Adawi, P. W. Fry, D. M. Whittaker, and D. G. Lidzey, "The optical properties of hybrid organic-inorganic L3 nanocavities," *Journal of the Optical Society of America B*, vol. 27, no. 2, pp. 215–221, 2010. [Online]. Available: http://dx.doi.org/10.1364/JOSAB.27.000215

[206] "Quality factor calculations," https://kb.lumerical.com/en/index.html?diffractive_optics_cavity_q_calculation.html, accessed: 2018-01-26.

[207] J. Kistner, X. Chen, Y. Weng, H. P. Strunk, M. B. Schubert, and J. H. Werner, "Photoluminescence from silicon nitride-no quantum effect," *Journal of Applied Physics*, vol. 110, no. 2, pp. 1–5, 2011. [Online]. Available: https://doi.org/10.1063/1.3607975

[208] I. Parkhomenko, L. Vlasukova, F. Komarov, O. Milchanin, M. Makhavikou, A. Mudryi, V. Zhivulko, J. Żuk, P. Kopyciński, and D. Murzalinov, "Origin of visible photoluminescence from Si-rich and N-rich silicon nitride films," *Thin Solid Films*, vol. 626, pp. 70–75, 2017. [Online]. Available: https://doi.org/10.1016/j.tsf.2017.02.027

[209] F. Ay and A. Aydinli, "Comparative investigation of hydrogen bonding in silicon based PECVD grown dielectrics for optical waveguides," *Optical Materials*, vol. 26, no. 1, pp. 33–46, 2004. [Online]. Available: http://dx.doi.org/10.1016/j.optmat.2003.12.004

[210] L. Ren, "Proximity effect in electron beam lithography," *Proceedings. 7th International Conference on Solid-State and Integrated Circuits Technology, 2004.*, vol. 1, pp. 579–582, 2004. [Online]. Available: http://dx.doi.org/10.1109/ICSICT.2004.1435073

[211] "Positive E-Beam Resists AR-P 6200 (CSAR 62)," Allresist GmbH, Tech. Rep., 2014. [Online]. Available: http://www.allresist.com/csar-62-ar-p-6200/

[212] H. R. Philipp, "Optical Properties of Silicon Nitride," *Journal of The Electrochemical Society*, vol. 120, no. 2, p. 295, 1973. [Online]. Available: https://doi.org/10.1149/1.2403440

[213] B. J. Hausmann, B. J. Shields, Q. Quan, Y. Chu, N. P. De Leon, R. Evans, M. J. Burek, A. S. Zibrov, M. Markham, D. J. Twitchen, H. Park, M. D. Lukin, and M. Loncr, "Coupling of NV centers to photonic crystal nanobeams in diamond," *Nano Letters*, vol. 13, no. 12, pp. 5791–5796, 2013. [Online]. Available: https://doi.org/10.1021/nl402174g

[214] M. Khan, T. Babinec, M. W. McCutcheon, P. Deotare, and M. Lončar, "Fabrication and characterization of high-quality-factor silicon nitride nanobeam cavities," *Optics Letters*, vol. 36, no. 3, p. 421, 2011. [Online]. Available: https://doi.org/10.1364/OL.36.000421

[215] Y. Gong and J. Vučković, "Photonic crystal cavities in silicon dioxide," *Applied Physics Letters*, vol. 96, no. 3, pp. 2009–2011, 2010. [Online]. Available: https://doi.org/10.1063/1.3297877

[216] C. Wang, M. J. Burek, Z. Lin, H. A. Atikian, V. Venkataraman, I.-C. Huang, P. Stark, and M. Lončar, "Integrated high quality factor lithium niobate microdisk resonators," *Optics Express*, vol. 22, no. 25, p. 30924, 2014. [Online]. Available: https://doi.org/10.1364/OE.22.030924

[217] E. S. Hosseini, S. Yegnanarayanan, A. H. Atabaki, M. Soltani, and A. Adibi, "High quality planar silicon nitride microdisk resonators for integrated photonics in the visible wavelength range." *Optics express*, vol. 17, no. 17, pp. 14 543–14 551, 2009. [Online]. Available: https://doi.org/10.1364/OE.17.014543

[218] H. Nelson, "An Investigation into Anderson Localized Modes in Silicon Nitride Photonic Crystal Waveguides," Masters Thesis, University of Southampton, 2015.

[219] T. Crane, "Anderson Localisation of Visible Light on a Chip," Masters Thesis, University of Southampton, 2016.

[220] S. Hughes, L. Ramunno, J. F. Young, and J. E. Sipe, "Extrinsic optical scattering loss in photonic crystal waveguides: Role of fabrication disorder and photon group velocity," *Physical Review Letters*, vol. 94, no. 3, pp. 1–4, 2005. [Online]. Available: https://dx.doi.org/10.1103/PhysRevLett.94.033903

[221] L. Sapienza, H. Thyrrestrup, S. Stobbe, P. D. Garcia, S. Smolka, and P. Lodahl, "Cavity quantum electrodynamics with Anderson-localized modes." *Science*, vol. 327, no. 5971, pp. 1352–1355, 2010. [Online]. Available: http://dx.doi.org/10.1126/science.1185080

[222] S. Smolka, H. Thyrrestrup, L. Sapienza, T. B. Lehmann, K. R. Rix, L. S. Froufe-Pérez, P. D. García, and P. Lodahl, "Probing the statistical properties of Anderson localization with quantum emitters," *New Journal of Physics*, vol. 13, no. 6, p. 063044, jun 2011. [Online]. Available: http://dx.doi.org/10.1088/1367-2630/13/6/063044

[223] J. Topolancik, F. Vollmer, and B. Ilic, "Random high- Q cavities in disordered photonic crystal waveguides," *Applied Physics Letters*, vol. 91, no. 20, pp. 1–4, 2007. [Online]. Available: http://dx.doi.org/10.1063/1.2809614

[224] M. Barth, N. Nusse, J. Stingl, B. Lochel, and O. Benson, "Emission properties of high-Q silicon nitride photonic crystal heterostructure cavities," *Applied Physics Letters*, vol. 93, no. 2, p. 021112, 2008. [Online]. Available: http://dx.doi.org/10.1063/1.2958346

[225] J. Topolancik, B. Ilic, and F. Vollmer, "Experimental observation of strong photon localization in disordered photonic crystal waveguides," *Physical Review Letters*, vol. 99, no. 25, p. 253901, 2007. [Online]. Available: http://dx.doi.org/10.1103/PhysRevLett.99.253901

[226] P. W. Anderson, "Absence of diffusion in certain random lattices," *Physical Review*, vol. 109, no. 5, pp. 1492–1505, 1958. [Online]. Available: http://dx.doi.org/10.1103/PhysRev.109.1492

[227] A. D. Lagendijk, B. V. Tiggelen, and D. S. Wiersma, "Fifty years of Anderson localization," *Physics Today*, vol. 62, no. August, pp. 24–29, 2009. [Online]. Available: http://dx.doi.org/10.1063/1.3206091

[228] S. John, "Electromagnetic absorption in a disordered medium near a photon mobility edge," *Physical Review Letters*, vol. 53, no. 22, pp. 2169–2172, 1984. [Online]. Available: http://dx.doi.org/10.1103/PhysRevLett.53.2169

[229] M. Patterson, S. Hughes, S. Combrié, N. V. Tran, A. De Rossi, R. Gabet, and Y. Jaouën, "Disorder-induced coherent scattering in slow-light photonic crystal waveguides," *Physical Review Letters*, vol. 102, no. 25, pp. 1–4, 2009. [Online]. Available: https://dx.doi.org/10.1103/PhysRevLett.102.253903

[230] M. Wilson, "A photonic crystal localizes light in two dimensions," *Physics Today*, vol. 60, no. 5 May, pp. 22–23, 2007. [Online]. Available: http://dx.doi.org/10.1063/1.2743114

[231] P. Sheng, *Introduction to Wave Scattering, Localization, and Mesoscopic Phenomena*. Elsevier Science, 1995.

[232] M. Cutler and N. F. Mott, "Observation of anderson localization in an electron gas," *Physical Review*, vol. 181, no. 3, pp. 1336–1340, 1969. [Online]. Available: http://dx.doi.org/10.1103/PhysRev.181.1336

[233] H. Hu, A. Strybulevych, J. H. Page, S. E. Skipetrov, and B. A. Van Tiggelen, "Localization of ultrasound in a three-dimensional elastic network," *Nature Physics*, vol. 4, no. 12, pp. 945–948, 2008. [Online]. Available: http://dx.doi.org/10.1038/nphys1101

[234] G. Roati, C. D'Errico, L. Fallani, M. Fattori, C. Fort, M. Zaccanti, G. Modugno, M. Modugno, and M. Inguscio, "Anderson localization of a non-interacting Bose-Einstein condensate," *Nature*, vol. 453, no. 7197, pp. 895–898, 2008. [Online]. Available: http://dx.doi.org/10.1038/nature07071

[235] A. A. Chabanov, M. Stoytchev, and A. Z. Genack, "Statistical signatures of photon localization," *Nature*, vol. 404, no. 6780, pp. 850–853, 2000. [Online]. Available: http://dx.doi.org/10.1038/35009055

[236] D. S. Wiersma, P. Bartolini, A. Lagendijk, and R. Righini, "Localization of light in a disordered medium," *Nature*, vol. 390, no. 6661, pp. 671–673, 1997. [Online]. Available: http://dx.doi.org/10.1038/37757

[237] J. P. Vasco and S. Hughes, "Statistics of Anderson-localized modes in disordered photonic crystal slab waveguides," *Physical Review B*, vol. 95, no. 22, p. 224202, jun 2017. [Online]. Available: https://dx.doi.org/10.1103/PhysRevB.95.224202

[238] K. Luke, Y. Okawachi, M. R. E. Lamont, A. L. Gaeta, and M. Lipson, "Broadband mid-infrared frequency comb generation in a Si_3N_4 microresonator," *Optics Letters*, vol. 40, no. 21, p. 4823, 2015. [Online]. Available: http://dx.doi.org/10.1364/OL.40.004823

[239] R. Coccioli, M. Boroditsky, K. Kim, Y. Rahmat-Samii, and E. Yablonovitch, "Smallest possible electromagnetic mode volume in a dielectric cavity," *IEE Proceedings - Optoelectronics*, vol. 145, no. 6, pp. 391–397, 1998. [Online]. Available: https://doi.org/10.1049/ip-opt:19982468

[240] Y. Zhang and M. Lončar, "Submicrometer diameter micropillar cavities with high quality factor and ultrasmall mode volume," *Optics Letters*, vol. 34, no. 7, p. 902, 2009. [Online]. Available: https://doi.org/10.1364/OL.34.000902

[241] D. S. Wiersma, "The physics and applications of random lasers," *Nature Physics*, vol. 4, no. 5, pp. 359–367, 2008. [Online]. Available: http://dx.doi.org/10.1038/nphys971

[242] H. S. Knowles, D. M. Kara, and M. Atatüre, "Observing bulk diamond spin coherence in high-purity nanodiamonds," *Nature Materials*, vol. 13, no. 1, pp. 21–25, 2014. [Online]. Available: http://dx.doi.org/10.1038/nmat3805

[243] J. Bertolotti, S. Gottardo, D. S. Wiersma, M. Ghulinyan, and L. Pavesi, "Optical necklace states in anderson localized 1D systems," *Physical Review Letters*, vol. 94, no. 11, p. 113903, 2005. [Online]. Available: https://dx.doi.org/10.1103/PhysRevLett.94.113903

[244] O. J. Trojak, T. Crane, and L. Sapienza, "Optical sensing with Anderson-localised light," *Applied Physics Letters*, vol. 111, no. 14, p. 141103, oct 2017. [Online]. Available: https://doi.org/10.1063/1.4999936

[245] J. Hodgkinson and R. P. Tatam, "Optical gas sensing: a review," *Measurement Science and Technology*, vol. 24, p. 012004, 2013. [Online]. Available: http://dx.doi.org/10.1088/0957-0233/24/1/012004

[246] M. Li, S. K. Cushing, and N. Wu, "Plasmon-enhanced optical sensors: a review," *The Analyst*, vol. 140, no. 2, pp. 386–406, 2015. [Online]. Available: http://dx.doi.org/10.1039/C4AN01079E

[247] W. Zhu, T. Xu, A. Agrawal, and H. J. Lezec, "High-Quality-Factor Cup Resonator for Plasmonic Sensor and Plasmon Laser," in *Conference on Lasers and Electro-Optics*. San Jose: Optical Society of America, 2016, p. FTh1B.5. [Online]. Available: https://doi.org/10.1364/CLEO{_}QELS.2016.FTh1B.5

[248] P. Jahangiri, F. B. Zarrabi, M. Naser- Moghadasi, A. Saee Arezoomand, and S. Heydari, "Hollow plasmonic high Q-factor absorber for bio-sensing in mid-infrared application," *Optics Communications*, vol. 394, no. August 2016, pp. 80–85, 2017. [Online]. Available: http://dx.doi.org/10.1016/j.optcom.2017.03.016

[249] S. Hamed Mirsadeghi, E. Schelew, and J. F. Young, "Photonic crystal slot-microcavity circuit implemented in silicon-on-insulator: High Q operation in solvent without undercutting," *Applied Physics Letters*, vol. 102, no. 13, pp. 3–6, 2013. [Online]. Available: http://dx.doi.org/10.1063/1.4799963

[250] A. Di Falco, L. O'Faolain, and T. F. Krauss, "Chemical sensing in slotted photonic crystal heterostructure cavities," *Applied Physics Letters*, vol. 94, no. 6, pp. 9–11, 2009. [Online]. Available: http://dx.doi.org/10.1063/1.3079671

[251] Y.-N. Zhang, Y. Zhao, and R.-Q. Lv, "A review for optical sensors based on photonic crystal cavities," *Sensors and Actuators A: Physical*, vol. 233, pp. 374–389, 2015. [Online]. Available: http://dx.doi.org/10.1016/j.sna.2015.07.025

[252] E. Chow, A. Grot, L. W. Mirkarimi, M. Sigalas, and G. Girolami, "Ultracompact biochemical sensor built with two-dimensional photonic crystal microcavity." *Optics letters*, vol. 29, no. 10, pp. 1093–1095, 2004. [Online]. Available: http://dx.doi.org/10.1364/OL.29.001093

[253] D. F. Dorfner, T. Hürlimann, T. Zabel, L. H. Frandsen, G. Abstreiter, and J. J. Finley, "Silicon photonic crystal nanostructures for refractive index sensing," *Applied Physics Letters*, vol. 93, no. 18, pp. 2–4, 2008. [Online]. Available: http://dx.doi.org/10.1063/1.3009203

[254] W. Liu, J. Yan, and Y. Shi, "High sensitivity visible light refractive index sensor based on high order mode Si_3N_4 photonic crystal nanobeam cavity," *Optics Express*, vol. 25, no. 25, p. 31739, dec 2017. [Online]. Available: http://dx.doi.org/10.1364/OE.25.031739

[255] Y. Gong, M. Makarova, S. Yerci, R. Li, M. J. Stevens, B. Baek, S. W. Nam, R. H. Hadfield, S. N. Dorenbos, V. Zwiller, J. Vuckovic, and L. Dal Negro, "Linewidth narrowing and Purcell enhancement in photonic crystal cavities on an Er-doped silicon nitride platform," *Optics Express*, vol. 18, no. 3, p. 2601, 2010. [Online]. Available: http://dx.doi.org/10.1364/OE.18.002601

[256] Y. Ooka, T. Tetsumoto, A. Fushimi, W. Yoshiki, and T. Tanabe, "CMOS compatible high-Q photonic crystal nanocavity fabricated with photolithography on silicon photonic platform," *Scientific Reports*, vol. 5, no. February, pp. 1–9, 2015. [Online]. Available: http://dx.doi.org/10.1038/srep11312

[257] O. J. Trojak, C. Murray, R. Wang, H. Alizadeh, F. Pinheiro, L. Dal Negro, and L. Sapienza, "Experimental investigation of light confinement in golden-angle, sipral photonic crystals," *In Preperation*, 2018.

[258] L. Negro, *Optics of Aperiodic Structures: Fundamentals and Device Applications*. Pan Stanford Publishing, 2013.

[259] R. Penrose, "Pentaplexity A Class of Non-Periodic Tilings of the Plane," *The Mathematical Intelligencer*, vol. 2, no. 1, pp. 32–37, mar 1979. [Online]. Available: https://doi.org/10.1007/BF03024384

[260] V. Passias, N. V. Valappil, Z. Shi, L. Deych, A. A. Lisyansky, and V. M. Menon, "Luminescence properties of a Fibonacci photonic quasicrystal," *Optics Express*, vol. 17, no. 8, p. 6636, 2009. [Online]. Available: https://doi.org/10.1364/OE.17.006636

[261] M. E. Zoorob, M. D. Charlton, G. J. Parker, J. J. Baumberg, and M. C. Netti, "Complete photonic bandgaps in 12-fold symmetric quasicrystals," *Nature*, vol. 404, no. 6779, pp. 740–743, 2000. [Online]. Available: https://doi.org/10.1038/35008023

[262] J. K. Yang, S. V. Boriskina, H. Noh, M. J. Rooks, G. S. Solomon, L. Dal Negro, and H. Cao, "Demonstration of laser action in a pseudorandom medium," *Applied Physics Letters*, vol. 97, no. 22, pp. 2–5, 2010. [Online]. Available: https://doi.org/10.1063/1.3519844

[263] A. N. Poddubny and E. L. Ivchenko, "Photonic quasicrystalline and aperiodic structures," *Physica E: Low-Dimensional Systems and Nanostructures*, vol. 42, no. 7, pp. 1871–1895, 2010. [Online]. Available: http://dx.doi.org/10.1016/j.physe.2010.02.020

[264] M. H. Kok, W. Lu, W. Y. Tam, and G. K. L. Wong, "Lasing from dye-doped icosahedral quasicrystals in dichromate gelatin emulsions," *Optics Express*, vol. 17, no. 9, p. 7275, 2009. [Online]. Available: https://doi.org/10.1364/OE.17.007275

[265] H. Vogel, "A better way to construct the sunflower head," *Mathematical Biosciences*, vol. 44, no. 3-4, pp. 179–189, jun 1979. [Online]. Available: https://doi.org/10.1016/0025-5564(79)90080-4

[266] D. Thompson, *On Growth and Form*, ser. Dover Books on Biology Series. Dover Publications, 1942.

[267] J. Trevino, S. F. Liew, H. Noh, H. Cao, and L. Dal Negro, "Geometrical structure, multifractal spectra and localized optical modes of aperiodic Vogel spirals," *Optics Express*, vol. 20, no. 3, pp. 3015–3033, 2012. [Online]. Available: https://doi.org/10.1364/OE.20.003015

[268] N. Lawrence, J. Trevino, and L. Dal Negro, "Aperiodic arrays of active nanopillars for radiation engineering," *Journal of Applied Physics*, vol. 111, no. 11, pp. 1–9, 2012. [Online]. Available: https://doi.org/10.1063/1.4723564

[269] M. E. Pollard and G. J. Parker, "Low-contrast bandgaps of a planar parabolic spiral lattice." *Optics letters*, vol. 34, no. 18, pp. 2805–7, 2009. [Online]. Available: https://doi.org/10.1364/OL.34.002805

[270] J. Trevino, H. Cao, and L. Dal Negro, "Circularly symmetric light scattering from nanoplasmonic spirals," *Nano Letters*, vol. 11, no. 5, pp. 2008–2016, 2011. [Online]. Available: https://doi.org/10.1021/nl2003736

[271] S. F. Liew, H. Noh, J. Trevino, L. Dal Negro, and H. Cao, "Localized photonic band edge modes and orbital angular momenta of light in a golden-angle spiral," *Optics Express*, vol. 19, no. 24, p. 23631, 2011. [Online]. Available: https://doi.org/10.1364/OE.19.023631

[272] K. Guo, M. Du, C. I. Osorio, and A. F. Koenderink, "Broadband light scattering and photoluminescence enhancement from plasmonic Vogel's golden spirals," *Laser and Photonics Reviews*, vol. 11, no. 3, pp. 1–10, 2017. [Online]. Available: https://doi.org/10.1002/lpor.201600235

[273] F. Intonti, N. Caselli, N. Lawrence, J. Trevino, D. S. Wiersma, and L. Dal Negro, "Near-field distribution and propagation of scattering resonances in Vogel spiral arrays of dielectric nanopillars," *New Journal of Physics*, vol. 15, pp. 1–12, 2013. [Online]. Available: https://doi.org/10.1088/1367-2630/15/8/085023

[274] O. J. Trojak, "On-chip Single-photon Sources for Quantum Information Technology," 16 Month Upgrade Report, University of Southampton, 2016.

Note that in IEEE style, — denotes the same authors as the previous reference.

Acronyms

1D	1-dimensional.
2D	2-dimensional.
3D	3-dimensional.
AFM	atomic force microscope.
BEC	Bose-Einstein condensate.
BME	Bloch mode expansion.
CCD	charge coupled device.
CMOS	complementary metal oxide semiconductor.
CNOT	controlled NOT gate.
CNT	carbon nanotube.
CVD	chemical vapour deposition.
CW	continuous wave.
DBR	distributed Bragg reflector.
DI	deionized.
EBL	electron beam lithography.
EMCCD	electron-multiplying CCD.
EPR	Einstein-Podolsky-Rosen.
FDTD	finite-difference time-domain.
FIB	focussed ion beam.
FM	flip-mirror.
FPGA	field-programmable gate array.
FWHM	full-width half-maximum.
GAVS	golden angle Vogel spiral.
HBT	Hanbury-Brown and Twiss.
HOM	Hong-Ou-Mandel.
HP	hot-plate.

ICP	inductively-coupled plasma.
IPA	isopropyl alcohol.
ITH	internal thermal heating.
ITO	indium tin oxide.
KOH	potassium hydroxide.
LDOS	local density of states.
LED	light emitting diode.
LHe	liquid helium.
LPCVD	low pressure chemical vapour deposition.
LPF	longpass filter.
MBE	molecular beam epitaxy.
MIBK	methyl isobutyl ketone.
ML	monolayer.
MMA	methyl methacrylate (co-polymer).
Mo	molybdenum.
NDF	neutral density filter.
NIR	near infrared.
NMR	nuclear magnetic resonance.
NV	nitrogen-vacancy.
PECVD	plasma-enhanced chemical vapour deposition.
PhC	photonic crystal.
PL	photoluminescence.
PMMA	poly(methyl methacrylate).
ps-pulsed	picosecond-pulsed.
QD	quantum dot.
QED	quantum electrodynamics.
Q-factor	quality-factor.
QKD	quantum key distribution.
R.T.	room temperature.
RTA	rapid thermal annealing.
SEM	scanning electron microscope.
SFWM	spontaneous four-wave mixing.
Si_3N_4	silicon nitride.
SIL	solid immersion lens.
SK	Stranski-Krastanov.

SPAD	single photon avalanche photo-diode.
SSQD	solid state quantum dot.
TE	transverse electric.
TM	transverse magnetic.
UV	ultra violet.
XOR	exclusive OR.
ZPL	zero phonon line.

Index